Development of Al- and Mg-based Nanocomposites via Solid-State Synthesis

by

Naser Al-Aqeeli

Department of Mining, Metals and Materials Engineering
McGill University
Montreal, Canada

A thesis submitted to the
Faculty of Graduate Studies and Research
In partial fulfillment of the requirements for the degree of
Doctor of Philosophy

Your file Votre référence
ISBN: 978-0-494-32129-4
Our file Notre référence
ISBN: 978-0-494-32129-4

Abstract

Mechanical milling (alloying) is one of the non-equilibrium techniques used to prepare alloys with exceptional properties. This technique was employed in this research to develop a new class of Al- and Mg-based nanocomposite alloys using SPEX high energy milling. These nanocomposites are characterized by the dispersion of nanocrystals in an amorphous matrix. Zirconium was added to the Al-Mg alloys for the purpose of promoting glass formability. As-milled samples were annealed at 400°C for 1 hour to investigate the thermal stability of the nanostructure. The phase evolution of the resulting alloys was studied using XRD and TEM/EDS, which showed a strong dependence of the resulting metastable phases on the starting alloys compositions.

The nanocomposite structure was developed at Zr concentrations of 20 and 35 at.% regardless of the Al/Mg ratio and with some traces of oxidation. However, the amount of amorphous phase was varied in each case depending on the Al concentration into the alloy, since in low Al-containing alloys the amount of amorphous phase was less pronounced. It was found that higher Zr concentrations will lead to greater refinement of the nanostructure. These nanocomposites showed improved mechanical properties, in terms of higher hardness values, in addition to improved thermal stability. The improvement in thermal stability was attributed to the presence of Al_3Zr which proved to contribute significantly to retarding grain growth via grain boundary pinning.

Additionally, the employment of mechanical alloying was beneficial in producing Al_3Zr in the cubic $L1_2$ ordered structure which improves the ductility of the alloy. Moreover, the homogeneity ranges of γ-$Al_{12}Mg_{17}$ and Al_3Zr were extended significantly due to the nature of the non-equilibrium processing. In this research, the alloy with the maximum hardness was $Al_{40}Mg_{25}Zr_{35}$, which has an average hardness value close to 780 HV and average crystallite size of about 10 nm. A common observation in the alloys that showed a higher hardness values combined with improved thermal stability, is that they contain higher Al and Zr concentrations.

Résumé

Le broyage mécanique est une technique hors équilibre qui permet la fabrication de nouveaux alliages avec des propriétés exceptionnelles. Lors de cette recherche, un broyeur SPEX 8000 a été utilisé pour développer une nouvelle classe de nanocomposites à base d'aluminium et de magnésium. Ces nanocomposites tirent leur spécificité de leur dispersion de nanocrystaux dans une matrice amorphe. Du zirconium a été ajouté aux alliages d'aluminium et de magnésium pour promouvoir l'amorphisation. Les échantillons de poudres broyées ont été recuits à 400°C pour 1 heure pour évaluer la stabilité thermique des différentes phases. Leur évolution a été caractérisée par diffraction par rayon-X et par MEB/EDS. Il fut démontré que les phases métastables obtenues dépendent fortement de la composition des alliages de départ.

La structure nanocomposite a été formée avec des concentrations en zirconium de 20 et 35at.%, peu importe le ratio Al/Mg. Par contre, la quantité de phase amorphe formée varie selon la quantité d'Al dans l'alliage, la phase amorphe étant plus importante avec une plus grande concentration d'Al. Dans tous les cas, une certaine contamination d'oxygène était présente. Il a aussi été démontré qu'une concentration plus élevée de Zr mène à un plus grand raffinement de la nanostructure et à des valeurs de dureté plus élevées. Ces composites contenant plus de Zr ont de meilleures propriétés mécaniques, en terme de dureté, en plus d'une stabilité thermique accrue. Cette dernière est attribuée à la formation de Al_3Zr, qui contribue significativement à retarder le grossissement de grain par l'ancrage des joints de grain.

En plus, l'utilisation de l'alliage mécanique a permis la formation de Al_3Zr cubique $L1_2$, ce qui améliore la ductilité de l'alliage. Aussi, les plages d'homogénéité des phases γ-$Al_{12}Mg_{17}$ et Al_3Zr ont été fortement étendues par la nature hors équilibre du procédé. Dans cette étude, l'alliage avec la dureté la plus élevée est le $Al_{40}Mg_{25}Zr_{35}$, avec une dureté moyenne proche de 780 HV et une taille de cristallites d'environ 10 nm. Il fut observé que tous les alliages démontrant une dureté élevée ainsi qu'une stabilité thermique accrue contenaient des concentrations d'Al et de Zr élevées.

ACKNOWLEDGMENTS

I acknowledge, with gratitude and appreciation the guidance provided to me by my thesis supervisor Professor Robin A. L. Drew. I thank him for giving me enough room for personal scientific development and providing me with confidence to implement my ideas and to see myself in this research. He continuously enriched my skills and experiences by providing me with opportunities and necessary challenges, in spite of his busy schedule. I would like also to express special thanks and appreciations to Dr. Guillermo Mendoza-Suarez for his valuable help and guidance throughout all phases of this project. I appreciate all the comments and fruitful discussions we had.

Acknowledgments are due to all the organizations that sponsored the project and/or granted my scholarship. Special thanks are for Natural Science and Engineering Research Council of Canada (NSERC) for financial support of the project and to King Fahd University of Petroleum & Minerals (KFUPM) for sponsoring my PhD residency.

Sincere thanks to all personnel of the department for their friendship and their continuous support throughout my PhD stay in the Metals and Materials Engineering Department. Lots of thanks to the technical personnel of the department for the support and assistance provided to me one-way or another.

It is also important to thank all my friends and colleagues for providing me with an intellectually stimulating and most friendly environment in addition to their fun and support. I should remember: Farzad, Ozgur, Ramona, Fabian, Xin, Lydia, Laura, Abdel, Paula, Yaneth, Dominique, Abdulaziz, Felix, Umugaba, Camille, Andreas (surprisingly, I dropped you man on the first draft) ... I hope I did not drop anyone else and if I did I thank you all.

Last but not least, I express my heartfelt gratitude to my loving parents, brothers and sisters for their love and encouragement, constant prayers, continuing support, understanding and for enduring the geographical distance from me during my PhD.

Finally, I should mention that I will never be able to forget what my loving wife (Maee) has provided me with during every single moment. Maee: many thanks for your encouragement and enormous patience ... I thank you for all the sacrifices you made ... without your support, your presence, your love, I will never be able to accomplish this.

Table of Contents

List of Figures

List of Tables

Chapter 1

Introduction and Objectives

1.1 INTRODUCTION

Aluminium-magnesium-based alloys represent the alloys of choice in many automotive, aerospace and structural applications. They offer combined benefits of high strength and light weight (high specific strength) in addition to maintaining good corrosion resistance by adding a suitable amount of Al that promotes protective oxidation. The development of new Al-Mg-based alloys with improved properties is essential to meet the challenges and demands for higher performance alloys. This can be achieved by choosing the right constituents combined with a suitable processing techniques. The mechanical and physical properties can be improved significantly by employing non-equilibrium processing techniques which promote the formation of non-equilibrium phases, such as intermetallics and solid solutions. One of the simplest and most versatile techniques is Mechanical Alloying (MA).

Mechanical alloying is a novel and simple powder metallurgy processing technique that facilitates the development of non-equilibrium materials with remarkable properties. In general, alloying is achieved by repeated cold welding and fracturing of powders, when placed in a mill. It can be used to produce metastable phases and to extend solid solubility limits yielding materials with nanometer-grain sizes and, hence, improved properties. This technique has been employed successfully in the fabrication of Al-Mg alloys and has led to the production of new alloys with exceptional properties. It can also be used to develop new classes of nanocomposite materials which were introduced in the 1990's.

These nanocomposites were initially synthesized by Rapid Solidification (RS), another non-equilibrium processing technique. The term nanocomposite refers to their structural characteristics, which are similar to the well-known composite materials but with dispersed particles at the nanometer scale embedded into an amorphous matrix. They offer remarkable properties over conventional materials, in particular, at elevated temperatures. Nevertheless, no Al-Mg-based nanocomposite has been developed using MA starting from metallic powders.

To yield Al-Mg nanocomposites of similar characteristics, the addition of a ternary transition metal seems to be necessary to promote the formation of an amorphous phase. In this research, Zr represents the element of choice since it enhances glass formability, improves fatigue corrosion cracking resistance and retards natural aging.

The addition of a glass former, like Zr, can be of great benefit in developing Al-Mg-based nanocomposites and providing some additional properties. In fact, only very little work has been reported on the effect of Zr addition to mechanically alloyed Al-Mg alloys and no work was published on the possible formation of Al-Mg-based nanocomposite materials. Most of the work published on Zr addition was directed to liquid processing routes and little or no information is available on the processing of Zr-containing alloys via solid-state synthesis.

1.2 AIM OF THIS WORK

The main objective of this project is to develop Al-Mg-Zr nanocomposite materials via solid-state synthesis (mechanical alloying). These nanocomposite materials have structural characteristics similar to the well-known composite materials but with nanocrystalline grains embedded in an amorphous matrix. The study of phase evolution of these nanocomposites and the effect of variable Zr concentrations on the final microstructure will be carried out using a variety of characterization techniques; namely, XRD and EDS/TEM. The thermal stability of the developed nanocomposites will be evaluated via isothermal annealing.

Additionally, the effect of alloys' compositions and the formation of a nanocomposite structure on mechanical properties will be evaluated via hardness measurements. Alloys powders will be compacted in order to facilitate mechanical testing. Moreover, the extension of homogeneity ranges of some metastable phases

will be studied as the application of non-equilibrium processing yields alloys and intermetallics beyond their equilibrium homogeneity ranges. Finally, the composition of the alloy combining the highest hardness value in addition to improved thermal stability will be presented at the end of this research.

Chapter 2

Literature Review

2.1 MECHANICAL ALLOYING (MA)

2.1.1 Non-equilibrium Processing Techniques

Mechanical Alloying (MA) or milling is one of the non-equilibrium processing techniques that can facilitate the formation of metastable phases, i.e. phases that are stable under certain conditions. To explain the process from an energy perspective the following schematic (Figure 2.1) is provided. As observed, the free energy of the system "G" varies at each stage of the process. The energy is brought initially from the stable level G_o to a higher (and unstable) level G_2 and then quenched rapidly to a lower level G_1 to maintain the metastable phases that lead to the advantageous and novel properties. [1]

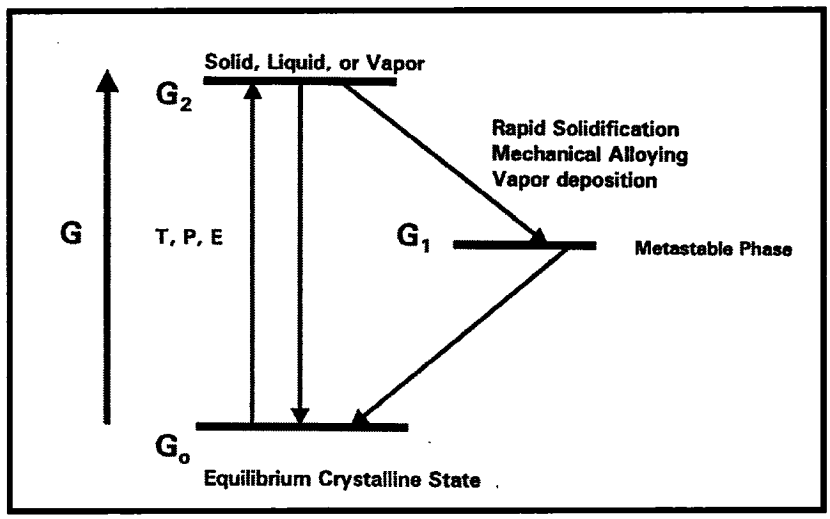

Figure 2.1: The variation of free energy "G" in non-equilibrium techniques [1].

Non-equilibrium is referred to as a systematic departure of the material from the equilibrium state, which can be attained in many processing techniques, and has been reviewed elsewhere [2] with particular emphasis on MA, plasma processing, and physical vapour deposition (PVD). In general, processing materials under non-equilibrium facilitates:

1. Producing fine dispersed second phases
2. Extending solid solubility
3. Refining the microstructure to nanometer scale
4. Synthesizing novel crystalline phases
5. Developing amorphous phases

6. Alloying elements that have large differences in melting points or involve complex solidification paths.
7. Allowing chemical reactions at low temperatures
8. Producing large quantities

It should be kept in mind, however, that in non-equilibrium techniques involving higher temperatures, partial return to equilibrium condition can occur if cooling rates are relatively slow. Moreover, if a material under non-equilibrium conditions is exposed to high temperatures, the metastable phases might transform into stable phases that can degrade the properties of the material while in service. As compared to Rapid Solidification (RS), mechanical alloying leads to higher solid solubility values than RS. For instance, some solid solubility was achieved by MA for Ti-Mg system, where there was no detectable solubility by RS [2]. However, this mainly depends on the system under study since it is not possible to generalize such an observation to all systems.

2.1.2 Development and History of MA

Mechanical Alloying (MA) is defined in literature as a dry powder metallurgy processing technique that involves cold welding, fracturing and rewelding of powder particles in a high-energy ball mill. However, this definition is not accurate since low-energy milling may produce good-quality alloying. The technique is used to synthesize a variety of alloy phases, including: 1) equilibrium 2) supersaturated solid

solutions (SSSS) 3) crystalline or quasicrystalline intermediate phases 4) amorphous or glassy alloys and 5) nanocrystalline materials. [3]

From a historical point of view, this technique was used earlier to reduce the particle size of powders and in some mining applications. However, it was introduced at INCO's Paul D. Merica's Research laboratory in 1966 for new applications of developing alloys combining Oxide Dispersions (ODS) with γ' precipitation hardening in a nickel-based superalloy intended for gas turbine applications. The idea was to combine the high temperature strength of the dispersed oxides with the intermediate temperature strength of the γ' precipitates, while taking into account the required corrosion and oxidation resistance [4].

The process was called mechanical alloying at first by the patent attorney of INCO to describe the process although it was not considered as a "real" alloying process rather milling/mixing [5]. It is essential to distinguish at this stage between milling and alloying, as in milling there is no formation of intermetallics or compounds (pre-alloyed intermetallics are used with the powder) rather there is only a change in structure and/or microstructure [6].

In mechanical alloying, the alloying action occurs by the repeated welding and fracturing of the powders in a highly activated ball charge. The alloying proceeds via solid-state reactions which are triggered by the impact forces between milling balls and powder particles. It was widely accepted when the technique was introduced that

for the alloying process to take place it is necessary to have at least one ductile metal to promote bonding. However, some reports showed the possibility of alloying brittle-brittle materials, in which the less brittle materials will act as binder in the alloying process [7].

From an industrial perspective, the first alloy prepared for commercial purposes was Ni-20Cr ODS (oxide dispersion strengthening) for the B-1 bomber engine in the first stage vanes and bands. As a first commercial product, INCONEL MA6000 alloy was used as a turbine blade material. The story that led to the use of MA process in the production of precipitation hardening alloys and the first applications are discussed in details in the review provided by Benjamin. [5]

Since the development of MA, there has been little research aiming to exploit the possible capabilities of this processing technique. However, the research and interest in MA grew significantly after the development of the first amorphous material in 1983 using this technique [8]. Only then, researchers realized that MA holds a potential for the development of advanced and non-equilibrium alloys. Moreover, only at that time it was accepted to refer to this process as a "true" alloying. A summary of the important events and dates in the use of MA was provided by Suryanarayana in his comprehensive review on this process [1]. Table 2.1 summarizes those turning points:

Table 2.1: Important events in the development of MA processing [1]

Year	Event
1966	Development of ODS nickel-base alloys
1981	Amorphization of intermetallics
1982	Disordering of ordered components
1983	Amorphization of blended elemental powder mixtures
1987/88	Synthesis of nanocrystalline phases
1989	Occurrence of displacement reactions
1989	Synthesis of quasicrystalline phases

As mentioned earlier that there has been a growing interest in MA process and many research papers are published every year covering a wide range of applications and topics. Publications in the past 20 years could be in the order of 1000-2000 in journals and conference proceedings in English language [9]. Quantitatively, Figure 2.2 shows the number of publications in the field of MA in English language only up to the year 1994. Nevertheless, most of the published papers in the field of MA seem to be somewhat repetitions of each other, only in changing the types of alloys in the milling process, hence represent only little scientific contribution. Moreover, the scientific impact is very little since only few papers dealt with the science underlying MA.

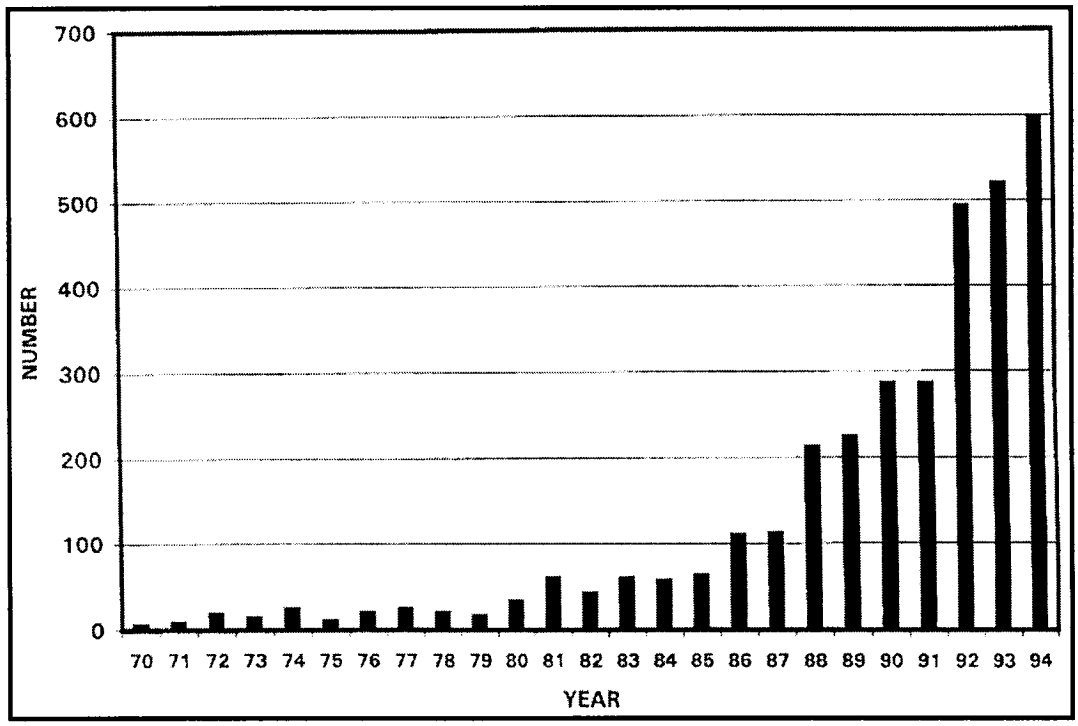

Figure 2.2: Number of publications in MA until 1994 [3].

Figure 2.2 shows the dramatic increase in the number of publications after the introduction of the first amorphous phase using MA in 1981 and the emergence of mechanochemistry in 1989. Mechanochemistry is the given name to the alloying process which involves chemical reactions (displacement reactions). Mechanochemistry and the accompanying displacement reactions will be discussed in greater details later in this chapter.

Mechanical alloying has many advantages as a processing technique which includes being simple, versatile, economically viable and enables the synthesis of novel alloys, i.e. alloying of otherwise immiscible elements. In addition to that, it

produces materials with improved properties compared with conventional methods. It should be kept in mind that mechanical alloying is a solid-state processing technique and therefore the limitations imposed by phase diagrams do not apply here. It also enables large scale production of up to 3000 lb (1250 kg). [1]

The steps involved into the MA process can be summarized as:

1. Loading powders into a sealed stainless steel vial under a protective argon atmosphere in a glove box. Loading the powder into an inert environment is essential since oxygen and nitrogen impurities might lead to the formation of undesirable oxides and nitrides.
2. Adding a controlled amount of process control agent (PCA) about 1-2 % to prevent excessive cold welding, especially if powders of ductile materials are used. More information will be provided later on the importance and the use of PCA.
3. Adding the powder material in measured percentages along with the grinding medium "milling balls".
4. Adjusting the ball:powder ratio (BPR), which is one of the main parameters in reaching high intensity milling.

As a result of milling/collisions, the powder interfaces which are impacted during the milling process become integral part of the particle (perfection of welding). Figure 2.3 shows the layered structure resulting from milling two elemental powders [10].

This structure is typical in most milling conditions and is analogous to layered composite materials.

Figure 2.3: Resulting layered structure from milling [10].

With respect to the types of mills used in laboratory and industrial practice, there exist many types of mills differing in their intensity, design, and powder discharge. The first type is a SPEX shaker mill, which is employed in this research, where a charge of 10-20 grams of powder can be processed at a time and it is commonly used in laboratories. Then comes the planetary ball mill (like the Pulverisette mill manufactured by Fritsch) where powders can be processed in more than one container. The planetary mill owes its names from the vial movement, analogous to planet-like motion. The recent mills from Fritsch are equipped with gas pressure and temperature measuring system (GTM) for in-situ data acquisition during milling. Another type is the Attritor mill in which powder up to 100 lb can be processed and is less energetic than the first two. It is also known as stirred ball mill and manufactured by Union

Process. However, the time periods required for milling are shorter for the SPEX and Planetary mills and longer for the attritors. [3, 11]

All the aforementioned mills are considered as dry milling equipments. In practice, milling can also be carried out at cryogenic (very low) temperatures in the presence of liquid medium "wet milling". The cryogenic medium is usually liquid nitrogen and the whole process is commonly referred to as cryomilling. However, the subject of cryomilling is not of our concern in this research and for more information, some very recent reviews [12] can be referred to.

2.1.3 Role of Diffusion in MA

Since mechanical alloying is performed at room temperature, it is essential to study the role of diffusion on the alloying process. In general, it is easier to nucleate metastable phases compared to equilibrium phases due to the relative simplicity of their crystal structures. In mechanical alloying, compounds can be formed by the enhanced diffusion due to the milling action and can grow at the low temperatures experienced by the powder. Structural defects such as grain boundaries and interfaces are believed to be responsible for the enhanced diffusivity of the powder. It is not confirmed yet if the mechanical stress plays any significant role in enhancing the diffusivity [9].

In MA the continuous refinement of composite structures can be related to the decrease in reaction temperature. In other words, with further milling the interface layer decreases in thickness leading to faster reactions. When a compound has formed the additional milling action will contribute in refining the structure further. As an example, SiC has been produced by MA by simply milling Si and C, since new interfaces are introduced continuously, as the milling progresses, which enhances the rate of diffusion. On the contrary, this is not possible by heating Si and C, since no new interfaces are created upon heating and only limited amount of SiC is produced. More specifically, the bulk diffusivity is low for Si and C and MA greatly enhances diffusion by introducing new interfaces. [9]

Many studies have suggested that the progress of alloying in MA is attributed to the accelerated diffusion between metal powders. Factors affecting diffusion in such cases can be summarized as: the super-equilibrium vacancies as a result of the severe plastic deformation, flow of matter over grain boundaries because of high shear levels, and the adiabatic heating in slip bands. [13]

2.1.4 Advantages of MA

2.1.4.1 Extending Solid Solubility and Formation of Intermetallics

In general, alloys that form metastable structures are desirable since they can be tailored to fulfill certain application requirements. For instance, supersaturated alloys

can exhibit good corrosion resistance and high ductility [14]. The ease of the development of metastable materials through the simple solid-state reaction encouraged many materials' scientists to explore the MA technique [9]. As for MA technique, solid solubility extension is one of the main advantages. As stated earlier, in non-equilibrium processing techniques the rules of phase diagrams do not apply and phases could be formed at values that are not achievable under equilibrium conditions. Moreover, even in systems where no detectable solubility is observed, MA proves to be capable of forming some metastable phases.

For instance, it was observed experimentally [14] that the solid solubility of Mg into Al can be extended to 18 at% for $Al_{70}Mg_{30}$ and to 45 at% in $Al_{50}Mg_{50}$ alloys by employing MA, which are well beyond the equilibrium values. The obtained supersaturated alloys exhibit high ductility, good corrosion resistance and broad single-phase homogeneity range. Even if the thermodynamic conditions are satisfied for the formation of a solid solution, as indicated by the negative heat of mixing, only based on the kinetic conditions the formation of the SS can be assured [9].

In some reports, the extension in solid solubility was attributed to the temperature increase inside the vial that is thought to be as high as 400°C. However, researchers have reported different values for vial temperature rise and all values were determined based on differential scanning calorimetry (DSC) observations. No direct measurement of the internal vial temperature has been reported and this is due to the difficulties encountered in inserting and maintaining a thermocouple during the high

intensity milling process. Moreover, it is difficult to determine the collision temperature of the trapped powder due to the random nature of powder-ball and powder-wall collisions.

Suryanarayana et al. [3] stated that the increase in solid solubility during MA may be explained by incorporating Hume-Ruthery rules. In fact, there exist many explanations (hypotheses) to the increase in solid solubility limits, but the widely accepted hypothesis is the one that relates to the formation of nanostructures during milling, since there is a large volume fraction of atoms residing in grain boundaries which enhances the diffusion and increases the solid solubility [15]. However, all of the existing theories can not explain the observations in all systems.

As for the formation of intermetallic phases, MA can promote as well the nucleation and growth of intermetallic compounds at low temperatures due to the enhanced diffusivity, which is reached by the introduction of structural defects [9]. The interest in intermetallics is due to the fact that they are promising materials for the use in high-temperature structural applications. However, the only draw back in forming intermetallics is their noticeable brittleness [16]. In general, the formation of either an intermetallic or a solid solution phase during MA depends mainly on the free energy of the competing phases [3].

2.1.4.2 Grain Refinement

Milling can facilitate the formation of materials with very fine grains (of nanometric size) up to certain limit. With further milling of a single phase elemental powder or an intermetallic compound the particle size will reach a minimum of 3-25 nm or will undergo amorphization beyond this point, thus sets the limitations to the possible refinement in grains. The refinement of grain size can not continue and it is absolutely limited by the consequence cold welding. The reduction of grain size is also limited by the minimum grain size where no nucleation or propagation of cracks is allowed within grains.

To explain the nanocrystalline formation, a mechanism similar to dynamic recrystallization occurs during grain reduction. This is due to the fact that during hot working, grains are formed by the annihilation of dislocations and the transformation of subgrains into grain by grain rotation and subgrain boundary sliding. These grains maintain their nanometric size since the milling temperature is relatively low for grain growth to take place. The final grain size can be reached once equilibrium between dislocation accumulation and dynamic recovery is established. In other approaches, some experiments suggested that the minimum grain size is inversely proportional to melting temperature. However, this appears valid for some FCC crystals with $T_m >$ 1800 K but cannot be generalized. Some studies suggested that the nanograins nucleate and grow in a relatively slow rate due to the low temperature encountered during milling. [9]

The development of nanostructures by MA was explained by Koch [17] via several steps that can be summarized as:

1. Localized deformation and increase in dislocation density.
2. Movement of dislocations, annihilation/rearrangement to form a cell with nanometer scales.
3. Random orientation of grains.

2.1.4.3 Nanostructures Formation

To start from the basics, it should be stated that materials are considered as nanostructured if the crystal size is in the order of few nanometers (typically 1-100 nm) in at least one dimension. They can be classified into:

1. equiaxed: called crystallites (3D)
2. filamentary (2D), or
3. lamellar: and referred to as layered nanostructure (1D)

The reduction in grain size to the nanometric scale offers many advantages, including: high strength, improved soft magnetic properties and greater processing versatility [18]. Nanostructured materials feature enhanced properties like: increased strength/hardness, enhanced diffusivity, improved ductility/toughness, reduced density, reduced elastic modulus, higher electrical resistivity, increased specific heat, higher thermal expansion coefficient and lower thermal conductivity [19].

Along with MA, nanostructured materials can be synthesized using a variety of techniques such as: 1) inert gas condensation, 2) electrodeposition, 3) sputtering, 4) crystallization of amorphous phases, 5) rapid solidification, and 6) chemical processing. However, it is important to mention that it has been reported [9] that the formation of nanograins in MA is a result of the numerous nucleation events of the limited growing phase and not a result of the fracturing and cold welding actions.

Among the many aforementioned processing techniques, mechanical alloying is preferred for the formation of nanograin materials for many reasons which include: its simplicity, relatively low cost, applicability to any class of materials, and the ability to scale up to tonnage quantities [3]. Some problems may arise while using MA which include possible contamination from the milling media or atmosphere, and the need of compacting powders without grain coarsening.

Based on some TEM observations, Koch [17] confirmed that the crystallite size decreases continuously with milling time. As of milling energy, previous results have indicated that the final crystallite size does not depend on energy, since comparable grain sizes have been obtained from both a shaker mill and conventional low energy ball mill. However, milling energy affects the kinetics of the process with processing time being several orders of magnitude higher in low energy milling. Crystallite size can be assessed using either direct TEM observation or X-ray broadening measurements. The latter can be performed using the Williamson-Hall method [20] or

root-mean-square (rms) strain from X-ray broadening using the Scherrer formula. However, direct observation using TEM gives more precise and reliable values.

It was stated that nanograins could be stable which might be due to the uniformity of grain size (narrow grain size distribution), inclusions and pinning by solutes. In the previous paper by Koch [17], the formation of nanocrystalline materials from the amorphous state was discussed. It is useful to keep in mind that in nanocrystalline materials a substantial fraction of atoms resides in the interfaces (it could reach 50% for 5 nm grains), hence, properties are greatly affected by the interfacial structure. In general, nanostructured materials are considered as in metastable state since the grain boundaries are relatively unrelaxed.

2.1.4.4 Amorphization by MA

One of the main discoveries that resulted in an increased interest in MA was the development of amorphous phases from crystalline elemental powders. As stated earlier, the first amorphous material obtained by MA from blended powders was the $Ni_{60}Nb_{40}$ compound by Koch et al. in 1983 [8]. It has been reported elsewhere that amorphization represents one of the mostly reported events in MA research [3], since it seems to be possible to fabricate amorphous alloys by MA when appropriate milling conditions are met. Amorphous alloys can also be produced by rapid solidification and rapid condensation of mixed metal gases. However, for MA, it is interesting how easy it is to produce metastable phases by just milling powders in the solid state.

To start from basics, three possible products can form when milling two elemental powders A & B:

1. Amorphous phase
2. A(B) or B(A) SS, and/or
3. A_xB_y intermetallic compounds

The amorphous phase can nucleate if its kinetic conditions are more favourable over the formation of other metastable phases. There are no bases that would guarantee the formation of an amorphous phase but if the milled alloy is an easy glass former through RS then the formation of an amorphous phase by MA can be predicted. In the process of producing an amorphous phase, it is necessary to satisfy the kinetic as well as the thermodynamic conditions. In terms of thermodynamics, the Gibbs free energy of the starting powder should be greater than that of the amorphous phase. For the kinetic conditions, they mainly depend on the difficulty of forming intermetallic compounds and how restrictive the environment is. [9]

At the onset of the milling process, the powder will turn into a layered structure and extending the milling operation will lead to amorphization by solid-state (interdiffusion) reaction under thermodynamic equilibrium. As MA progresses, there is a continuous reduction in grain size along with subsequent increase in grain boundary area and possible expansion in lattice parameter; the accumulation of structural defects tend to destabilize the crystalline structure which then raises the free energy of the system [3].

In general, the three main features of amorphous metals are:

1. The amorphous atomic structure.
2. The absence of crystal defects (grain boundaries and dislocations).
3. The possible existence of wide compositional range for a single phase amorphous metal, like in the Ni-Zr system. This implies that the physical properties of a material can be modified by altering the composition over a wide range which is not possible for crystalline alloys, since most single-phase metals can only be formed within the narrow stability ranges of intermetallic phase. This feature of the amorphous phase can be very beneficial in magneto-optic thin films.

As mentioned earlier, in addition to MA two methods have been mainly adopted for the production of amorphous materials; melt spinning in the form of ribbons (50 μm in thickness) or vapour condensation to produce thin amorphous films. In the vapour quenching technique, the amorphous phase is obtained over a wider composition range because of the higher quenching rate, whereas for melt spinning, it can be obtained primarily in a composition close to deep eutectics. For MA, experiments have shown that it is possible to obtain the amorphous phase around the equiatomic composition (like 50Al-50at%Mg), i.e. at the composition of the high-melting intermetallic phase [3]. Moreover, amorphous phases that can be formed by MA might not be obtained by melt-spinning [21].

On the other hand, the fraction of amorphous phase formed can be determined only qualitatively by XRD. Quantitative measurements can be obtained from DSC through crystallization enthalpy measurements. Measuring some of the intrinsic properties can give a good indication of the terminal composition (such as crystallization or transition temperatures) of the amorphous phase. The measured properties would be constant at the boundary regions of the amorphous phase. If the value of the free enthalpy of mixing is more negative for a system it then shows easy amorphization.

Crystallization of amorphous materials into nanoscale sizes is possible and it is attributed to either impurity pick-up which alters T_x (crystallization temperature) of the mixture or the higher levels of temperatures reached in the milling vial. It is known that the amorphous phase contains a large excess energy over its equilibrium crystalline counterpart, which is released during heating [18]. Recrystallization of amorphous powders could also be a result of compaction through conventional routes like hot isostatic pressing (HIP) or dynamic routes like explosive compaction. [17]

In MA the amorphization phenomenon has been explained in literature [22] by different mechanisms that can be summarized as follows:

1. It is the result of rapid quenching of local melts produced by the mechanical impact.
2. In the milling of intermetallic compounds, it is suggested that the amorphization is due to the accumulation of deformation-generated defects,

which raise the free energy of the compound above that of the amorphous phase.

3. It has been proposed and widely accepted that the amorphous phase nucleates at the interfaces and grows by interdiffusion reaction under interfacial metastable equilibrium, analogous to that in thin-film diffusion couples and in co-deformed metal foils.

Solid-state amorphization can be reached for phase mixtures with negative enthalpies of mixing and large difference in atomic sizes between solute and solvent atoms. This metastable amorphous state becomes favourable when the diffusion and partitioning of long-range solutes are suppressed [23]. To investigate amorphization further, the progress of amorphization during MA of Fe-Zr was investigated by Hellstern et al. [24]. Amorphous alloys were obtained after milling layered composite material from 2 to 16 hours whereas prolonged milling led to homogenization of particles. It was observed that the level of internal stress was extremely high before the amorphization process takes place. They concluded that the main driving force for amorphization to proceed is the difference in free enthalpy between the amorphous phase and the crystalline composite.

2.1.5 Compaction and Heat Treatment

One of the main steps for evaluating mechanical properties and thermal stability of mechanically alloyed powders is the production of compacted samples. Mechanically

alloyed powders can be sintered in the same way as any other powder produced by other means like chemical vapour condensation. However, the irregularity in shape, due to collision stresses and the fact that they are heavily work hardened might impose some differences in sintering and compaction. No recent studies have been carried out to investigate the sintering action of MAed powders to compare with powders produced by other techniques. In general, consolidation conditions should be dealt with in great attention to avoid grain coarsening and subsequence loss of the nanostructure. Diffusion is needed for consolidation at the atomic scale but it may cause grain growth. It is difficult to achieve full consolidation at the atomic level and some experiments showed that fracture occurs along the original inter-particle boundaries. [9]

For some alloy systems, consolidation should be carried out at low temperatures to avoid grain coarsening or possible crystallization of some amorphous alloys. It was stated earlier that from an energy point of view, amorphous materials have higher energies compared to their equilibrium crystalline counterparts. Upon heating they release this energy to form other stable or metastable phases such as supersaturated solid solution or intermetallics [18]. Despite the fact that nanocrystalline materials are in metastable state, they could be resistant to grain growth, partly, because of a narrow grain size distribution and grain boundary pinning due to solute, inclusions/pores, and triple junctions. [18]

2.1.6 Process Control Agents (PCA)

During mechanical milling of ductile elements the powder might become agglomerated and hence reduces the efficiency of the alloying process. It is essential for effective alloying processes to take place to balance cold welding and fracturing. To achieve this, two approaches were adopted. The first is to modify the deformation mode of the powder particles in order to facilitate fracture before particles get deformed to large strains that are necessary for flattening and cold welding. The second approach, which is more common, is to add process control agents (PCA) to prevent agglomeration of the resulting powder and to enable extended alloying at the atomic scale [10]. Different PCAs and different quantities have been used in MA to alter the surface condition of the deformed powders by impeding clean metal to metal contact sufficiently for cold welding [25].

There exist many types of PCA differing in their properties and effect. Some examples include: stearic acid, heptane, ethylacetate, ethylenebidi-steramide, dodecane, methyl alcohol and polyethylene glycol. One of the key factors in selecting the suitable PCA is to account for its melting point. Most of the aforementioned additives have melting temperatures lower than 0°C, which makes it difficult to utilize them with powders. On the contrary, ethylenebidi-steramide has a melting point of 141°C and this temperature might not be always possible to reach inside the vial during MA. For this particular reason stearic acid and polyethylene glycol which have

melting points as 68 and 59°C, respectively, represent the PCA of choice for most of milling operations. [10]

2.1.7 Mechanochemistry

In the late 1980s, Schaffer and McCormick [26] explored mechanochemistry by milling Ca and CuO powders. They noticed that a displacement reaction occurring during milling, resulting in pure Cu while starting from CuO. It was quite surprising to realize that the milling energy was high enough to initiate chemical reactions without the addition of heat. Mechanochemistry was further explored by Shen et al. [27] in the Fe-CuO system. Shen et al. referred to the previous work by Schaffer and McCormick in which they added only Fe instead of Ca, and noticed the continuation of the displacement reaction on their system.

Three years after the discovery of mechanochemistry, Schaffer and McCormick [28] investigated the possible kinetics of solid-state displacement reactions during MA. In particular, the effects of charge ratio and ball size on the propagation of the reactions, using CuO and Fe. The evaluation was based on the measurable values of ignition temperature, combustion time and crystalline size. They found that reaction kinetics increase with increasing charge ratio. This is mainly because of the increase in collision events within the powder. Ball size has also an effect through particle collision frequency and collision energy. Solid-state displacement reactions are obtained via MA due to the nature of the process where new interfaces are

continuously created promoting rapid diffusion. This implies that, it is necessary for MA to be performed in an inert environment since new (clean) surfaces are always created. When two new surfaces impact each other then welding occurs and reaction takes place between these internal surfaces. The reduction of metal oxides by solid reducing agents is preceded by a collision action that causes an unstable reaction. This reaction proceeds by the propagation of a combustion wave through the partially reacted powder. If the ball mass is increased it helps in reducing the crystalline size and the ignition temperature due to the increased plastic work and strain for a given number of collisions. Also, increasing ball size can cause the local temperature of particles to increase. [28]

When milling ductile-brittle systems it is first observed that the hard phase disperses into the matrix of the ductile phase, before the reactions start. Also, highly negative free energy values would indicate the tendency of the reaction to proceed. The three factors that affect reaction rate are: reactants' area of contact, rate of nucleation of the product and rate of diffusion of atoms of the product phase. The heat generated from the exothermic reaction will propagate the solid-state reaction since the diffusion distances and interlayer thickness between reactants is low, which will promote reaction in short times. Hence, the displacement reaction occurs faster in a self-sustaining way.

2.1.8 Applications of MA

MA can be used to produce alloys that can be used in many applications including: aerospace, hydrogen storage, heaters, fertilizers and many others [3]. Alloys produced by mechanical alloying found potential applications in industry right from the beginning. As mentioned earlier, this process was first developed in industry to solve some of the problems encountered in the fabrication of high temperature superalloys. Apart from the first alloy developed by mechanical alloying, other alloys like Fe-based MA956, Al-based MA952, and Ni-based Inconel MA754 have gone into commercial scale production for the use in high temperature applications. One of the largest produced alloys for aerospace applications is Incoloy MA956 which was used in the precombustion chamber in a new generation of diesel engines developed in 1989. This alloy has superior corrosion resistance in addition to its high melting point compared with conventional Ni-based alloys. [10]

To elaborate more on the applications of MAed materials, Weber and Chellman [29] compared a newly developed mechanically alloyed Al-Mg-Li alloy (AL-905XL) with other commercial Al-based alloys (AA7075-T73 and AA7050-T74). The results revealed some improvement in density and mechanical properties in AL-905XL, which makes it a potential candidate in replacing some existing Al-based alloys. Moreover, the newly developed alloy possesses improved corrosion and crack initiation resistances. On the other hand, MA can be used also to synthesize rare earth permanent magnets through mechanochemical reactions induced by milling [30].

2.1.9 Modeling of MA

As mentioned earlier, different types of materials can be produced using MA including: amorphous alloys, intermetallics, composites and nanocomposites and nanocrystalline powders. Despite all the advantages and versatility, not much attention has been given to the modeling of MA process in order to assist in quantifying the produced phases. More understanding is required to develop and advance this process to commercial scale or turn it into a practical metallurgical process such as casting, melting and heat treatment [9]. The quantification attempts are limited to a semi-quantitative level since MA involves dynamic forces that make the analysis very complicated.

As an attempt to model MA processes, Maurice and Courtney [31] classified milling processes into three categories:

1. Vertical ball mill: attritor with moderate volume and moderate milling times (agitation is attained by impellers radiating from a central rotating shaft)
2. Vibratory or shaker mill (like SPEX); milling takes shorter times but the powder produced is in smaller quantities. It involves complex motion in three orthogonal directions.
3. Horizontal ball mill: involves rotation about a horizontal axis. It rotates at a speed lower than the critical speed which causes pinning of the balls to the wall of the drum. However, large volumes of powders are produced but require longer processing times.

During MA powders can be fragmented and trapped between two balls, between ball and vial wall, and in the case of vertical mill powder, trapped between balls and rotating impellers. The number of collision events certainly depends on the type of mill modeled. It is assumed that the cold welding process occurs when the severely plastically deformed surfaces of the powders overlap and become in contact. The analysis is made by studying the possible collisions of balls without powder and then introducing the powder particles by approximating it as an upset forging process between two parallel plates. This way, Maurice and Courtney [31] were able to estimate collision times, strain, and powder strain rate. In addition to that, the temperature increase can be obtained as a function of the milling times.

Additionally, Joardar et al. [32] have developed a model to determine the temperature of the entrapped powder particles during collision since it is difficult to facilitate direct measurement. A ternary AlNiFe alloy was employed in this model and the obtained temperature was as high as 473 K after 4-6 hours of milling. Milling of this alloy led to the formation of an AlNi intermetallic phase.

2.1.10 Comparison with Rapid Solidification (RS)

Rapid Solidification represents one of the main non-equilibrium processing techniques. It was started as an academic curiosity in the 1960's and matured into an industrially accepted technology with its use for the production of amorphous

ferromagnetic sheets for transformer core applications by AlliedSignal (most voluminous). Although the science underlying this process was investigated from the beginning the applications of its products emerged relatively slowly. This was mainly because of the limitations in the product size imposed by the nature of the process (melt-spinning).

In this section, a comparison between MA and RS will be presented as an attempt to highlight the importance and popularity of MA over RS. This comparison is based on calculating the obtained departure from equilibrium and by comparing extensions in solid solubility limits of both methods, since as indicated earlier, MA has the advantage of increasing the solid solubility over the equilibrium values. Some solid solubility values for both MA and RS for different systems are presented in Tables 2.2 and 2.3. As can be seen, they show different values for different systems, but in almost all cases both methods provide solubility limits higher than those obtained under equilibrium conditions. For the interest of this study, solid solubility values of Mg into Al will be considered. From the second table it is clear that RS shows higher solid solubility than MA, i.e. 40 at% and 23 at %, respectively. However, these values depend mainly on the composition of the starting material as shown previously by Calka et al [14] where solid solubility was increased up to 45 at % in $Mg_{50}Al_{50}$ alloy.

In terms of research interest, it is clear from Figure 2.4 that RS gained attention right from the beginning since it started as an academic curiosity. This is shown by the increased number of publications since 1960. On the contrary, not much attention was

paid to MA after its development for two reasons. The first is because it was developed to solve an existing industrial problem and by doing so not much attention was given to explore the potential of the process. The second reason is that the process was holding no promise for production of new materials, and only with the development of amorphous alloys, researchers started to recognize this process, and began showing more interest.

Table 2.2: Comparison between MA and RS in terms of solid solubility extension [3].

Solvent	Solute	Equilibrium value		By MA	By RSP
		At RT	Maximum		
Ag	Cu	0.0	14.0	100	100
Al	Mn	0.4	0.62	18.5	9.0
	Nb	0.0	0.065	25	2.4
	Ni	0.0	0.11	10	7.7
	Ru	0.0	0.008	14	4.5
	Ti	0.0	0.75	36	2.0
Ni	Ta	3.0	17.2	30	16.6
Ti	Si	0.0	3.5	37.5	6.0

Table 2.3: Comparison between MA and RS in terms of solid solubility extension [2].

Solvent	Solute	Solid solubility, at.-% Equilibrium at room temperature	RS	MA
Al	Fe	0·025	4·3	4·5
Al	Mg	18·9	40	23
Al	Nb	0·065	2·4	25–30
Al	Zr	0·083	1·5	9·1
Ag	Ni	~0	...	3·8
Mg	Ti	~0	...	4·2
Nb	Al	<6	25	60
Ni	Ag	~0	...	9·0
Ti	Al	<11	...	>33
Ti	Mg	<0·2	...	3·6

This can be seen by the rapid increase in the number of publications after the development of amorphous phases in 1981. However, this graph does not show the number of publications in RS after the year 1980. To complement this graph, the number of publications in RS after 1980 should be included to establish a complete comparison between these two processes.

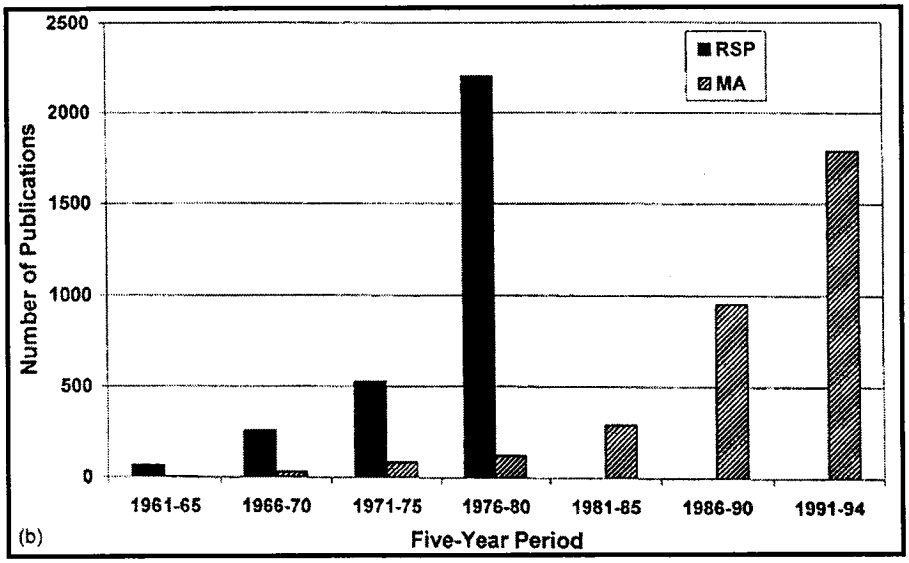

Figure 2.4: Comparison in the number of publication for MA and RS [3].

2.1.11 Contamination During MA

One of the main concerns with respect to MA process is the easy contamination of the powder particles due to the introduction of enormously fresh surfaces during the course of the process. The grinding media adds another source of contamination unless the grinding ball can be covered with the same milled materials. Iron-contamination of the powder is possible when steel balls and vials are used. Additionally, time and intensity of milling might also increase the contamination level, especially in high energy mills. [3]

In most cases, care should be taken while loading the powder into the vial since any trapped air will trigger oxidation reactions. It also depends on the milled powder

and its chemical affinity. Finally, the main concern is related to the formation of very fine grains since contamination might affect.

2.2 Mg-Al and Zr ALLOYS

2.2.1 Introduction

Aluminium is the second most important metal used in industry where it ranks second to Fe and Steel due to its special properties [10] and for some particular applications it is leading Fe. Aluminium is emerging in many applications, especially automotive and aerospace industries as the demand for lighter and higher performance materials is increasingly becoming an important issue. From the physical properties point of view, Al has an FCC structure and a density of 2.7 g/cm^3. Pure Al is fairly soft and ductile at room temperature and possesses relatively low yield strengths. Due to its low strengths, Al is alloyed with other metals in order to dramatically improve its mechanical properties. Common alloying elements include: magnesium, copper, zinc, manganese and nickel. Strengthening is achieved by solid-solution hardening and fine dispersions of precipitates. Among alloying elements, Mg-Al alloys proved to be potential candidates for structural, automotive and aerospace applications owing to their remarkable high specific strengths. They also offer good corrosion resistance, reasonable ductility and weldability in addition to high energy densities to be used in combustion and rocket propulsions.

Magnesium-aluminium alloys are processed by a variety of routes resulting in equilibrium and non-equilibrium phases. Non-equilibrium techniques are favoured as they yield improved properties with a metastable structure which showed to be beneficial in producing many desired mechanical and physical properties [14, 16].

As stated earlier, mechanical alloying is one of the non-equilibrium processing techniques that is capable of producing a variety of metastable phases [33, 34, 35], and can be used to fabricate these alloys. As for the Mg-Al system, studies have shown that the solid solubility limit of Mg in Al [33, 14, 36] and the homogeneity range of Mg-Al intermetallics [33] can be extended beyond the equilibrium values. Besides, the mechanical strength of Al-Mg alloys can be improved considerably by employing non-equilibrium processing techniques [37] through the formation of nanometric-size crystals. This is explained by the resistance of dislocation movement due to the increased volume fraction of grain boundaries. Other studies on MAed Al-5at%Mg [38] have shown that this particular alloy exhibits four times the strength of conventional 5083 alloy, in addition to maintaining good ductility (8.5% elongation). TEM studies showed a nanostructure consisting of equiaxed and randomly oriented grains with a mean size of 26 nm.

So, a considerable interest exists in mechanically alloyed Mg-Al alloys due to their promising properties. Generally, alloys are synthesized and then compacted to allow for mechanical property measurement. In the following section, some highlights of the

research activities that have recently been carried out in mechanically alloyed Mg-Al alloys are presented.

2.2.2 Research on Binary Al-Mg Alloys

To study the effect of varying Mg concentrations on the resulting microstructure and the formation of metastable phases, Schoenitz and Dreizin [35] milled Al-Mg binary alloys with Mg concentration varying between 5 and 50 at%. At a concentration of 40 at% Mg, a maximum supersaturation of 20.8 at% of Mg into the α-phase was reached. The γ-$Al_{12}Mg_{17}$ phase was present at Mg concentrations of 30 at% and above, however, no indication of the formation of the β-phase was observed in which they only nucleate after heat treatment. The results revealed that the re-crystallization of γ phase was observed near 170°C while precipitation of β occurred in the range 250-350°C. They concluded that the degree of supersaturation depends mainly on the energy of milling (higher ball:powder ratio) and higher levels of PCA. The average particle size ranged between 25 and 35 μm, and was independent on the alloy composition and ball:powder ratio.

In turn, Gao et al. [39] investigated the phase of mechanically alloyed Mg-5wt%Al mixtures and the resulting crystallite size. Magnesium crystallite sizes near 140 nm along with two types of second phase particles, namely, MgO and MgAl(O) were obtained after sintering and extrusion of the resulting powders. Milling for 10 hours resulted in the formation of the γ-phase which transformed into a solid solution of Al

into Mg upon further milling. As for mechanical properties, the yield strength of the extruded alloy was remarkably higher than the die-cast alloy of the same composition.

Other prolonged milling experiments [40] on the same alloy (Mg-5wt%Al) have shown that after 30 hours of milling, a solid solution of Al into Mg and γ-phase were formed. Spinel $MgAl_2O_4$ was observed after sintering of milled samples for 30h, which was evidence of oxidation. The crystallite size was dependent on milling time, being below 70 nm and 20 nm after 10 h and 30 h of milling, respectively. For samples milled for 5 h, grain growth was observed after sintering and extrusion, going from 69 nm to an average of about 200-300 nm. On the other hand, the average grain size after extrusion was of 60-120 nm for samples milled for 30 h. The presence of some dispersed particles at the grain boundaries after milling for 30 h was observed, which are believed to effectively pin grain boundaries during sintering and extrusion in alloys milled for longer periods.

On the other hand, Zhou et al. [41] investigated the recovery and recrystallization stages of mechanically milled Al-7.6 at% Mg with a resulting grain size of 25 nm using DSC. The results revealed that recovery occurs during annealing from 100 to 230°C while recrystallization occurs at a temperature of 370°C. Recovery was associated with an exothermic peak which is indicative of strain relaxation and grain coarsening.

To study the effect of milling temperature on this type of alloys, Hazelton [42] investigated the effect of the temperature on the formation of metastable phases in Al-Mg binary alloys. It was found that the milling temperature has practically no effect as it was varied over a range of 200°C, from -140 to 60°C. The formation of amorphous phases was possible by the addition of up to 6 at% of Zr, Ti, Y, Ca, V, Er or Pr to alloys near the $Mg_{40}Al_{60}$ composition. It is believed that this was the first time that a study claimed the formation of an amorphous phase in the Al-Mg system with the addition of a small amount of glass-forming element. However, the results are questionable since X-ray diffractograms do not show a strong indication of amorphous phase formation, instead they showed clear and distinct broadened and low intensity peaks. Additionally, no TEM work was provided to support the claim of amorphous phase formation. Compared to results published in relation to this work, 6 at.%Zr do not show to be enough in promoting the formation of an amorphous phase [43]. Other researchers have indicated that no amorphous phases are obtained in the Mg-Al system even with the addition of glass-forming additives [9, 34]. Moreover, no amorphous phase has been reported in the Al-Mg alloy system by RS.

2.2.3 Beta and Gamma Intermetallic Phases

From a thermodynamics point of view, the driving force for the formation of the γ and the β phases should be the same since they have similar values of heat of formation. However, from a kinetic perspective the formation of such phases is governed by other conditions. Beta has a complex cubic structure besides the large

unit cell (1168 atoms) whilst the γ-phase has a much simpler and smaller unit cell (58 atoms). Therefore, more interdiffusion between Al and Mg is needed for the formation of the β-phase. The γ-phase, on the other hand, will form first if the interface between Al/Mg allows the formation of metastable phases. Generally, at lower temperatures diffusion may be impaired and neither phases are thermodynamically stable. In this case, supersaturated FCC Al(Mg) and HCP Mg(Al) SS may form instead.

Zhang et al. [34] milled alloys of varying composition of Al-40, -60, -80at%Mg and showed experimentally that the reaction temperature for the formation of γ is independent of Mg content. They showed that, β-phase cannot be nucleated by milling since longer-range interdiffusion between Al and Mg is required to nucleate this phase with a complex structure and larger unit cell. Reactions are thought to occur while powders are trapped at collision points. Moreover, a procedure to predict the temperature inside the vial was carried out by attaching a thermocouple to its outer surface, indicating that the stabilized temperature was close to 50°C.

Singh et al. [33] proved that MA process is capable of extending the homogeneity range of Al-Mg intermetallic phases. In their study, they were able to alter the homogeneity ranges of the equilibrium phases present in the Al-Mg system, i.e. β (Al_3Mg_2) and γ ($Al_{12}Mg_{17}$). The Al content obtained for γ-phase was 30 at% after mechanical milling which is lower than the equilibrium value of 39.5 at.%Al. Moreover, it was found that the Al content for the formation of the β-phase could be

reduced from a value between 59.7 and 61.5 at% at equilibrium conditions to almost 50 at% post-milling.

To study the effect of temperature on the formation of Al-Mg intermetallics, Umbrajkar et al. [44] decreased the milling temperature from 70-80°C to 20-30°C and noticed that the amount of dissolved Mg into Al increased from 2-3 at% to ~25 at%. They also concluded that the formation of intermetallic phases is favoured at higher temperatures.

To further study the effect of milling times and ternary additions, on the evolution of phases and final crystallite size, Thein et al. [45] mechanically milled the composition Mg-5wt%Al for 5 and 20 h and added Ti to the alloy. The γ-phase with a grain size in the range 31 to 49 nm was detected after 5 h of milling. After 20 h of milling, the grain size decreased to 15-27 nm, with 10.3 %Ti alloy having the smallest grain size. Further milling did not reduce the crystallite size since an extremely high stress is needed to deform the nanometer-sized grains.

For the determination of metastable phases, X-ray diffraction is widely used in their characterization. When Mg diffuses into Al to form a solid solution (SS) the Al diffraction peaks will be shifted to lower angles due to the increase in lattice parameters and more diffusion of Mg into Al lattice is characterized by a larger shift. The lattice parameter "a" can be calculated from peak broadening and related to Mg content into the SS. In the previous case, if the amount of residual and undissolved Mg

is below the detection limit of XRD, which is between 2 and 5 %, depending on the instrument, then unalloyed Mg cannot be detected. [34]

2.2.4 Process Control Agent (PCA) in Mg-Al Alloys

The influence of PCA on mechanical alloying of Mg-Al binary alloys has been investigated by Lu and Zhang [25] by varying the type and amount of PCA. It was found that having a small amount of PCA accelerates interdiffusion reactions between Al and Mg. They stated that a greater addition of PCA is required when milling ductile materials. However, there is a lack of information regarding the effect of PCA when milling hard materials.

In an attempt to determine the adequate amount of PCA needed for proper milling of Al-Mg alloys, Zhang et al. [46] studied the optimum amount and type of PCA to produce fine particles. They found that the final particle size depends mainly on three factors; amount and type of PCA and duration of milling. Two types of PCA were used in their study, i.e. stearic acid and polyethylene glycol. Neural networks were trained in the research to predict the most suitable amount and type of PCA through the evaluation of the resulting mean crystallite size. It was found that at a certain level of PCA the average mean particles size is reduced. However, these results are limited to the type of materials milled into this study (Mg and Al) and the additives used. It was only an attempt to show the possible utilization of neural networks in the vicinity of experimental data to optimize the process parameters.

2.2.5 Addition of Zr

Zirconium can be added to Al-Mg alloys to improve fatigue corrosion cracking and natural aging resistance [47, 48], as well as to promote superplastic behavior [49, 50] through grain size refinement. Mechanical alloying has proved to promote the formation of intermetallics [51, 52] for the Al-Zr system, and metastable phases in both Mg-Zr [53, 54] and Mg-Al [34, 55, 35] systems.

However, it is essential to present some detailed studies dealing with the addition of Zr to Al and Mg in order to assess the individual effect of Zr addition before considering the addition of Zr to the binary Al-Mg alloy.

To study the metastable phases formed in the Zr-Al system, Fecht et al. [52] investigated the sequence of phase transformation in the mechanically alloyed Al-Zr system over alloy composition of Zr-10 up to 70 at%Al. The characterization of the MAed powders was carried out by TEM and XRD. The phase constitution was dependent mainly on the composition of the starting powders. For an Al concentration of less than 15 at%, a nanocrystalline supersaturated solid solution of α-Zr was present. When the Al concentration was increased to values between 15 and 40 at% the predominant phase was amorphous. At higher Al concentrations, a metastable FCC phase was present with a crystallite size of 4 nm.

Additionally, Sheng et al. [51] studied the effect of milling temperature on possible amorphization of $Zr_{100-X}Al_X$ (x= 0-40at%) alloys. They found that at low milling temperatures, an amorphous Zr-Al phase appeared under polymorphic constraint imposed by intensive external forces. At higher temperatures, an amorphous phase is obtained along with a solid solution forming a two-phase region. The results showed that the amount of Al needed for complete amorphization increases with the milling temperature. With respect to the Mg-Zr system, this mixture does not form either intermetallics or metastable phases. Zirconium seems to be present in the form of cores in Mg and can be revealed by SEM.

On the other hand, Desch et al. [16] studied the phase evolution of mechanically milled Al-Zr alloys. They confirmed the formation of the Al_3Zr intermetallic with a tetragonal crystallite DO_{23} structure under equilibrium conditions. However, the metastable cubic $L1_2$ structure can be produced using non-equilibrium processing techniques. This metastable structure forms at high temperatures and is considered beneficial for the mechanical properties since the problem with tri-aluminides such as Al_3Zr is their brittle nature. As stated previously, maintaining the metastable structure of Al_3Zr at room temperature is beneficial but quite challenging. Some studies [56] have suggested that the addition of ternary elements like Li stabilizes the $L1_2$ structure of Al_3Zr. However, such addition might not be feasible and other means of stabilizing this phase should be considered. One of the promising routes is the formation of nanograins that could act as a pinning mechanism and suppress the transformation of this phase into the equilibrium structure. In reality, mechanically milling Al-Zr can

produce a fairly stable Ll_2 structure since some studies [57] have shown that this crystal structure is stable up to approximately 600°C, after which the metastable phase transforms into the stable crystal structure DO_{23}. It seems that the closeness in lattice parameter and structure between Al and Al_3Zr facilitates the coherent precipitation of the metastable phase into the Al matrix.

For the role of Zr in promoting amorphization, El-Eskandarany et al. [58] mechanically milled Al-50at%Zr and observed that amorphization occurs in two distinct stages. First, milling will form layered-composite particles of larger sizes resulting from cold welding. In the second stage, the layered powder forms an amorphous phase after heating in the DTA to a temperature close to 400°C under Ar atmosphere. This transformation is attributed to thermally assisted solid-state amorphization, with the activation energy of amorphization Ea being independent of milling time.

For the possible improvement in mechanical properties due to the addition of Zr to Al, Rittner et al. [59] mechanically tested Al-Zr alloys produced by inert-gas condensation. They found that the modulus of elasticity of nanocrystalline alloys is similar to that of coarse-grained Al. Other properties such as hardness, strength and ductility seem to be affected by grain size which is reduced at higher Zr concentrations. Extremely high hardness values were obtained for these alloys; nevertheless, tensile properties were less impressive. For the smallest grain size, the material showed brittle-like fracture with no signs of plastic deformation. This can be

due to the apparently increased force needed to generate a dislocation to prevent crack propagation and generate yielding in the nanostructure regime. In their study they carried out compressive tests only, so the effect of flaws was not determined as they were not detrimental to the material's behaviour. It was noticed that extremely high stresses can be obtained under the indentor to produce plastic deformation.

With respect to the Mg-Zr system, very little work has been done to predict the possible phases resulting from MAing powder mixtures. Some studies [53] on Mg-0.56%Zr prepared by melting have confirmed only the presence of Zr-rich cores in either elliptical or nearly spherical forms. They also observed that these cores could be isolated or in clusters. These Zr-rich cores could be present at the Mg grain boundaries as well, which are characterized as pure Zr particles containing negligible amount of Fe as contamination. They concluded that in order to have excellent grain refinement it is desirable to supply a sufficient amount of Zr to form enough Zr particles in the melt prior to peritectic solidification. The majority of particles were in the range between 1 and 5 μm forming active nucleation sites for Mg grains. However, particles larger than 5 μm were inactive as nucleation sites. The best efficiency was achieved with particle sizes around 2 μm.

On the other hand, most of the work published in the Al-Mg-Zr system has focused on the liquid-processing route [50, 47, 60, 61, 62, 63], and little information is available on the processing of Al-Mg-Zr alloys by mechanical alloying. The very few published papers on mechanically milled Al-Mg-Zr alloys considered the addition of a

maximum amount of 0.6 wt.%Zr [48], and 6 at.%Zr [42], in addition to a published work in relation to this research where 5 at.%Zr was considered [64]. Therefore, a more thorough study is needed to evaluate phase evolution of the Al-Mg-Zr over a wider composition range.

For the available literature on the aforementioned mechanically milled Al-Mg-Zr alloys, Buso et al. [48] studied the microstructure of Al-2wt.%Mg-0.6%Zr using TEM. The alloys were prepared via MA, annealed at 623 K, then extruded and compacted. They confirmed that Zr contributes to improvement of the fatigue corrosion cracking and control natural aging; however, it causes loss of ductility. They mentioned that the solubility of Zr into Al-Mg alloys under normal conditions does not exceed 0.28 wt%, however, by the powder metallurgy techniques it can be increased by 2.5-5 times compared to normal conditions.

Hazelton et al. [42] added a fixed amount of 6 at.%Zr, and observed that some phases were suppressed by MA while others became more predominant than those in the equilibrium phase diagram. This study also considered the effect of milling temperature on the resulting structure and concluded that no effect was observed; neither on reaction rates nor on the final structure of the alloy.

2.3 Nanocomposites

At the beginning of this section it is appropriate to elaborate more on the features and advantages of having materials in the nanoscale range. In equiaxed nanocrystalline metals, two types of atoms can be distinguished, i.e. crystal atoms with nearest neighbour configurations belonging to a lattice and loosely packed grain boundary atoms with a variety of interatomic spacings. In such arrangement, a substantial fraction of atoms resides in the interfaces. This can be as much as 3% for 100 nm grains, 30% for 10 nm grains and increase to about 50% for 5 nm grains. In general, the grain boundaries in nanocrystalline materials are relatively unrelaxed (build-up of internal stresses), a state somewhat similar to rapidly quenched metallic glasses, in which the system of boundary atoms has a local but not global energy minimum; thus, the material is to be considered in a metastable condition. [18]

As mentioned earlier, the mechanical routes allow the development of nanostructured materials in large quantities. Typical refinement of metallic elements and intermetallics could reach 5-20 nm and atomic strains may vary between 0.7-2.5 % (for intermetallics). [23]

2.3.1 History and Development

The development of the nanocomposite materials (NCM) represents one of the deviation points in the field of structural materials. NCM materials possess tensile

stresses and hardness values higher than those exhibited by single phase amorphous materials of the same composition, in addition to retaining good bending ductility. The nanocomposites were first introduced by Kim et al. [65] and Chen et al. [66] in different alloy systems by melt-spinning (RS technique). The common feature of these nanocomposites is that the microstructure is comprised of nanograins embedded in an amorphous matrix, which proved to be responsible for the extraordinary improvement in properties.

In the work of Kim et al. [65], the nanocomposites were prepared directly by melt spinning alloys of compositions $Al_{88}Y_2Ni_9M_1$ (M = Mn or Fe). The resulting material consisted mainly of FCC-Al particles of about 3-4 nm in size dispersed in an amorphous matrix. The obtained tensile fracture strength (σ_f) and specific strength (σ_s) of AlYNiFe alloy were in the order of 1320 MPa and $40x10^3$ m, respectively, while the highest (σ_f) and (σ_s) for Al-based amorphous alloy of the same composition are of about 1140 MPa and $38x10^3$ m, respectively. This improvement in properties is presumably attributed to the presence of finely dispersed particles in the matrix which cause dramatic hardening of the FCC supersaturated solution. The improvement of strength was correlated to the percentage of dispersed particles and it was found that the highest fracture strength was obtained in the vicinity of 15 vol. % of the dispersion particles.

On the other hand, Chen et al. [66] were able to synthesize Al-based alloy with a composition of $Al_{90}Fe_5Gd_5$ through rapid solidification. The alloy consisted of an

amorphous matrix and was devitrified to obtain a nanocomposite structure. Partial crystallization was carried out by isothermal annealing for 20 minutes at a temperature below recrystallization, determined previously by differential scanning calorimetry (DSC). An improvement by 1/3 in fracture strength was found compared with the fully amorphous material with similar chemical composition. Grain sizes close to 8 nm were obtained; however, structure and compositions of nucleants were not reported.

Considering the aforementioned examples, these nanocomposite materials have also shown exceptional mechanical properties at high temperatures. At room temperature they exhibited a tensile strength of 1.6 GPa which is three times larger than the conventional alloys and 1.5 times higher than the corresponding fully amorphous alloy. At temperatures close to 300°C the tensile strength of these nanocomposites can reach 1 GPa, which is 20 times larger than the best conventional alloys at the same temperature. [67]

2.3.2 Amorphization

As indicated, nanocomposite materials can be formed either directly from the non-equilibrium process or by controlled heat treatment of the fully amorphous alloy (devitrification). In this section, some highlights on the amorphization process using mechanical alloying will be presented again as the amorphous phase represents a precursor for obtaining nanocomposites. In general, if any alloy system is an easy glass former through rapid solidification process or during solid state reaction in thin

films, then the formation of an amorphous phase through MA can be predicted. The ease of formation of the amorphous phases by rapid quenching is a reasonable indication of the level of difficulty of nucleating A_xB_y compounds that compete with the amorphous phase [9]. For Al-Mg alloy systems where it is difficult to nucleate the amorphous phase, the addition of ternary transition metal seems crucial to promote amorphization.

On the other hand, the nucleation of amorphous phases in mechanical alloying can take place directly from blended elemental powders or through the formation of an intermetallic phase. Two possible routes that can be followed in the formation of the amorphous phase:

$$mA + nB \rightarrow (A_m B_n)_{amorphous}$$

$$mA + nB \rightarrow (A_m B_n)_{crystalline} \rightarrow (A_m B_n)_{amorphous}$$

Where A and B are the elements being milled.

In addition to that, it is possible to have a solid solution forming prior to the formation of the amorphous phase. Having a former solid solution or an intermetallic phase depends on the relative free energies of the two competing phases. Moreover, the amorphous phase will form if the kinetic conditions of the formation of solid solutions are unstable or the intermetallic phase is difficult to nucleate. Nevertheless, the mechanism of amorphization is not clearly understood. It is believed that a

destabilization of the crystalline phase occurs as a result of the accumulation of structural defects, viz., vacancies, dislocations and grain boundaries [3]. In general, for the production of amorphous phases it should be kept in mind that rapid solidification process produces amorphous phases usually around deep eutectic compositions, but the composition range in MAed amorphous alloys is generally around equiatomic compositions [10].

2.3.3 Formation of Nanocomposites

2.3.3.1 Using Mechanical Alloying

Since the introduction of nanocomposite materials there has been a considerable amount of research aimed at synthesizing similar materials via different processing routes. In particular, the synthesis of nanocomposites through mechanical alloying has been the subject of research for many years. Some successful results were obtained by either milling elemental metallic powders of by adding oxides and/or carbides that can promote in-situ formation of the nanocomposites. In this section, some of the main achievements in synthesizing nanocomposites via mechanical alloying will be presented along with some elaboration on the milling conditions, characteristics of the resulting structure and the obtained improvement (if any) in properties.

On that basis, Murphy and Courtney [68] were able to successfully produce nanocomposite materials in 1994 using mechanical alloying. They started with

elemental powders of Cu and Nb in the presence of graphite or hexane to form a nanocomposite material. The obtained powders were consolidated using hot-press resulting in a compact with a relative density near 100%. Compaction of powders was carried out at a temperature of 0.3 T_m of NbC to maintain the nanostructure.

In another work by Krasnowski et al. [69] nanocomposite powders were obtained by milling Al_{50}-Fe_{25}-Ti_{25} (at%) with ethanol (C_2H_5OH) and ammonium carbonate ($(NH_4)_2CO_3$). They obtained a nanocomposite structure consisting mainly of an Fe(Al) matrix with some dispersed complex carbides of Al-Ti when milling with ethanol. Another type of nanocomposite was obtained when ammonium carbonate was added to the powder. The resulting powder consisted mainly of Fe(Al) matrix and dispersed TiN intermetallic grains. Particle sizes ranged from several nanometers to 20 nm when milling for 280 h.

In other study, Krasnowski and Kulik [70] were able to obtain a nanocomposite materials by mechanically milling elemental powders of Al, Fe and Ti, in nitrogen atmosphere. The resulting powder was then hot-pressed and consolidated under a pressure of 8 GPa to facilitate mechanical testing. Two consolidation temperatures were considered in their research, 750 and 950°C, which led to different hardness values, 1424 HV for 750 and 1461 HV for 950°C with a relative density of 97% in both cases. The nanocomposite consisted mainly of Fe(Al) solid solution and TiN of a few nanometers in size.

Zhang et al. [71] were able to obtain a nanocomposite material with WC particles embedded into a Co matrix. The size of the WC particles was reduced to 11 nm after 10 hours of milling. In their study, milling was also effective in changing the crystal structure of Co from FCC to HCP. Also, Li et al. [72] prepared a nanocomposite alloy by milling Al with NiO. Nickel oxide decomposed after 10 hours of milling without forming alumina, which was attributed to the diluent of alumina phase. Upon heat treating the alloy milled for 15 h at a temperature of 1400°C for 1 h, alumina was observed in addition to the nanosized Ni particles.

On the other hand, mechanical alloying shows to be advantageous in producing materials that are free of undesirable phases. For instance, in a study carried out by El-Eskandarany [73], mechanical alloying showed to be very successful in producing Al-SiC_p nanocomposites free of the undesirable Al_4C_3 and Si brittle phases. Consolidation of the milled powder into bulk compacts was attained using plasma activated sintering. In their study, SiC particles were homogeneously distributed into the Al matrix providing improved mechanical properties. The content of SiC was varied between 2 and 10 vol.% and an increase in density, hardness and elastic modulus was observed at higher SiC content.

Also, Woo and Zhang [74] were able to produce nanocomposite material by milling powders of composition Al-7Si-0.4Mg-34wt%SiC. The powders were then sintered at temperatures of 570 and 600°C to study the effect of SiC reinforcement on the hardness. They observed a considerable improvement in hardness values compared

with mixed and sintered composite powders (without milling). This confirms the role of milling in producing nanometric- and submicron-size composites with improved properties. Milling was also effective in increasing the sintering rate due to the enhanced diffusivity.

Starting from elemental powders, Hwang et al. [75] mechanically milled Mg-Ti-C to produce a nanocomposite structure of TiC nanoparticles (size 3-7 nm) embedded into nanocrystalline Mg matrix with crystals ranging in size between 25 and 60 nm. The obtained powders were subjected to compressive testing upon consolidation, showing an improvement in ductility while retaining their high compressive strengths.

Considering the previously mentioned examples, one might think that the addition of oxides, carbides or nitrides is necessary for the formation of a nanocomposite structure using mechanical alloying. In practice, the development of nanocomposite materials is also possible by directly milling elemental powders without the addition of carbides and/or oxides. In that respect, Sheng et al. [76] were able to obtain a nanocomposite material after milling Al and In powders for 300 hours. The final material was obtained with a composition of $Al_{95}In_5$, where the nanostructure contained mainly In particles embedded into an Al matrix. The grain sizes of both Al and In were 29 and 18 nm, respectively. However, they did not observe the expected layered structure in the resulting material, and this was attributed to the partial diffusion of In during milling. Additionally, they reported that there is no evidence of amorphization or extended solid solubility between Al and In. Since contamination is

expected for prolonged milling, Fe contents of 0.87 at% were observed dissolved in the Al matrix after 300 hours of milling.

2.3.3.2 Mechanochemical Synthesis

It is also possible to synthesize nanocomposite materials by employing self-sustained displacement reactions caused by milling (mechanochemistry). In this respect, Ying and Zhang [77] were able to produce Cu-Al_2O_3 nanocomposites through multiple-milling steps. They milled elemental powders of Al and Cu forming Cu(Al) solid solution and then milling the resultant solid solution (SS) with CuO to facilitate the displacement reaction between Al and O. The powders were then consolidated to form nanometric-size (< 200 nm) alumina particles with a 20 vol.% embedded into Cu matrix.

On the same basis, Wu and Li [78] were able to obtain a nanostructural composite material by milling Al and CuO powders for 56 hours. The formation of this nanocomposite was achieved by the progression of mechanochemical reaction between Al and CuO to form Al_4Cu_9 intermetallic, which then transformed upon annealing to $CuAl_2$. Additional oxides and carbides were present that offered substantial reinforcement to the Al matrix. Those precipitates differed in size as $CuAl_2$ was in the range of 100-500 nm and Al_2O_3 whereas the Al_4C_3 crystals showed sizes in the 10-50 nm range. Compression tests were carried out, showing that the nanocomposites exhibited excellent strengths both at room and high temperatures. The

improvement in strength was attributed to the fine dispersoids embedded in the Al matrix.

2.3.3.3 Other Methods

Apart from mechanical alloying and rapid solidification, it is possible to synthesize nanocomposite materials by other means which include: direct hot-pressing and spark plasma sintering. Selected publications related to these methods will be presented in this section which might indicate the possible formation of these advanced materials using rather simpler techniques.

Using hot-press, Yoshimura et al. [79] were able to obtain a nanocomposite alloy comprising of SiC particles embedded into Y_2O_3 matrix at the grain boundaries by directly hot-pressing the powders at temperatures ranging from 1300 to 1750°C. The SiC content varied between 2 and 15 vol.% and the measured particles sizes were below 100 nm. Mechanical properties of this alloy were improved especially at high temperatures after the addition of SiC particles. The highest fracture strength was obtained at 5 vol.% reaching 750 MPa at 1200°C in air. They attributed this improvement to the oxidation of SiC particles which are present at the grain boundaries.

Gao et al. [80] fabricated YAG-5 vol.% SiC "nano"-composite by spark plasma sintering. The addition of 5 vol.% SiC showed a considerable increase in bending

strength over monolithic YAG ceramics. Sintering was carried out at a temperature of 1500°C for 1 h. All particles obtained into this study were larger than 1 μm in size and thus the term nanocomposite should not be applied to the resulting alloys.

2.3.4 Heat Treatment

As stated previously, nanocomposites can be produced by controlled heat treatment from an amorphous precursor, which should be performed with great care since extended treatments might lead to the possible growth of the nanograins, hence with the loss of the nanostructure.

In this regard, Inoue et al. [81] investigated the crystallization of amorphous $Zr_{60}Al_{10}Cu_{30}$ alloy prepared by RS. The crystallization occurred by the simultaneous precipitation of Zr_2Al and Zr_2Cu. When Pd was added to the alloy, the nanostructure was preserved and the resulting particle size was ~ 200 nm. Some improvement in tensile strength (from 1.76 to 1.88 GPa) as well as Young's modulus (from 81.5 to 89.5 GPa) were observed due to the increased volume fraction of the Zr_2Cu intermetallic phase in the nanostructured alloy. These nanostructural compounds coexisted with a surrounding glassy phase that provided improved tensile strength and ductility, due to the fact that this glassy phase has a high free volume that remained after quenching.

As a comparison between different heat treatment routes, Gupta et al. [82] studied the early stages of crystallization of an $Fe_{72}Cu_1Nb_{4.5}Si_{13.5}B_9$ amorphous alloy and the formation of nanoscale particles. Specimens were devitrified by two means: furnace and electrical current. It was observed that there was no significant difference in the resulting nanostructures obtained by both routes of annealing. Iron-based amorphous alloys were prepared by RS and then annealed at 590°C for 10, 20, and 87 min (furnace annealing) and current annealed by passing a DC current of 7.8 A for 12 and 90 seconds. In this study, the formation of a nanostructured alloy was due to the presence of Cu and Nb in the alloy since the immiscibility of Cu in Fe helps in forming clusters which nucleate the nanostructured phase. They concluded that the addition of Nb was essential in stabilizing the residual amorphous phase and retarding grain growth.

Chapter 3

Experimental Techniques and Research Methodology

3.1 EXPERIMENTAL PROCEDURE

3.1.1 Starting Materials

In this research, mixtures of elemental Al, Mg and Zr (>99% purity and -325 mesh) powders provided by Alfa Aesar were used as starting materials. The composition of these powders with the level of impurity level is shown in Table 3.1. The size of the as-received powders is less than < 45 μm (99.9% of the powder). Moreover, the as-received materials were analyzed using X-ray diffraction in order to assess any possible presence of internal stresses and it showed no broadening into the XRD peaks indicative of stress-free powders.

Table 3.1: Compositions of as-received Al-Mg-Zr powders (all values are in wt.%).

	Si	Fe	Cu	Mn	H	Ni	Ca	Mg	Ga	Hf	other
Al	0.05	0.13	0.01	0.01	-	0.01	-	-	0.02	-	< 0.03
Mg	-	-	0.02	0.1	-	0.001	-	Bal.	-	-	< 0.06
Zr	0.3	0.08	-	-	0.25	-	0.15	0.15	-	0.2	< 0.09

3.1.2 Alloys Composition

The compositions of the prepared alloys were varied in order to assess the effect of different Al/Mg ratio and the effect of Zr on the formation of the nanocomposites and the subsequent effect on hardness. The different compositions of the alloys under study are all shown in Table 3.2. The prepared alloys were classified into four main categories. The first category is the *Low Mg Alloys*, in which the Mg concentration was fixed at 10 at% and Zr was varied from 0 to 35at%. The second category is considered as the *High Mg Alloys* where the content of Mg was raised to 40 at%. *Low Al Alloys* is the third category where the Al concentration was maintained at 10 at%. The final category with Al concentration of 40 at% was classified as *High Al Alloys* accordingly. Again, in all categories the Zr content was always varied between 0 and 35 at%. This variation in concentration resulted in 4 binary alloys and 12 ternary alloys.

Table 3.2: Break-down of compositions of alloys prepared in this research; (all values are in atomic percent).

Category of Alloys	*Composition*
Low Mg-containing Alloys $\mathbf{Mg_{10}Al_{90-x}Zr_x}$ **(x=0, 5, 20 and 35at.%)**	$10Mg-90Al$
	$10Mg-85Al-5Zr$
	$10Mg-70Al-20Zr$
	$10Mg-55Al-35Zr$
High Mg-containing Alloys $\mathbf{Mg_{40}Al_{60-x}Zr_x}$ **(x=0, 5, 20 and 35at.%)**	$40Mg-60Al$
	$40Mg-55Al-5Zr$
	$40Mg-40Al-20Zr$
	$40Mg-25Al-35Zr$
Low Al-containing Alloys $\mathbf{Al_{10}Mg_{90-x}Zr_x}$ **(x=0, 5, 20 and 35at.%)**	$10Al-90Mg$
	$10Al-85Mg-5Zr$
	$10Al-70Mg-20Zr$
	$10Al-55Mg-35Zr$
High Al-containing Alloys $\mathbf{Al_{40}Mg_{60-x}Zr_x}$ **(x=0, 5, 20 and 35at.%)**	$40Al-60Mg$
	$40Al-55Mg-5Zr$
	$40Al-40Mg-20Zr$
	$40Al-25Mg-35Zr$

3.1.3 Alloys Preparation

The alloys were prepared using a SPEX 8000 shaker mill and the milling time was fixed at 9 hours in all experiments. Previous experiments showed that 9 hours of milling is adequate for the production of metastable phases in Al-Mg alloys. Figure 3.1 shows a photograph of the mill used in this research. The powders were loaded in a hardened stainless steel vial under Ar atmosphere using a glove box to minimize reaction with air during milling. Stearic acid was added to the powder mixture as a process control agent (PCA) in a percentage between 2-3%.

Two balls of 12.7 mm and four of 6.35 mm in diameter were used to obtain a ball-to-powder (BPR) ratio of 10:1 in all stages of this investigation. Fixing the BPR and milling times throughout all experiments is beneficial in eliminating any effects of time and ratio on the phase evolution. The milling experiments were periodically halted every 1.5 hours for 3 hours to avoid temperature increase in the milling vial. Furthermore, to eliminate the buildup of unprocessed powders on the internal walls and dead spots the vial was opened after every 3 hours of milling under Ar and the deposited powders were scraped from the vial walls and incorporated back into the milling mixture.

Figure 3.1: SPEX 8000 mill used in preparation of alloys.

3.1.4 Annealing Experiments

The as-milled powders were annealed at 400°C for 1 hour to study phase stability and to examine possible transformations upon heating. This was performed in a tube furnace under Ar atmosphere to minimize oxidation. A schematic of the tube furnace set-up is shown in Figure 3.2.

For the annealing experiments, the alloys were placed into the tube furnace on a ceramic plate to avoid any reaction with the holder material and then inserted carefully into the hot zone and then secured at both ends of the tube. In addition to the as-milled alloys, pieces of Ti sponge were placed in the furnace in order to act as oxygen getter.

If the color of this Ti sponge turns black after the annealing process this indicates the presence of excess amount of oxygen during annealing, which is an indication of a leakage of air into the tube.

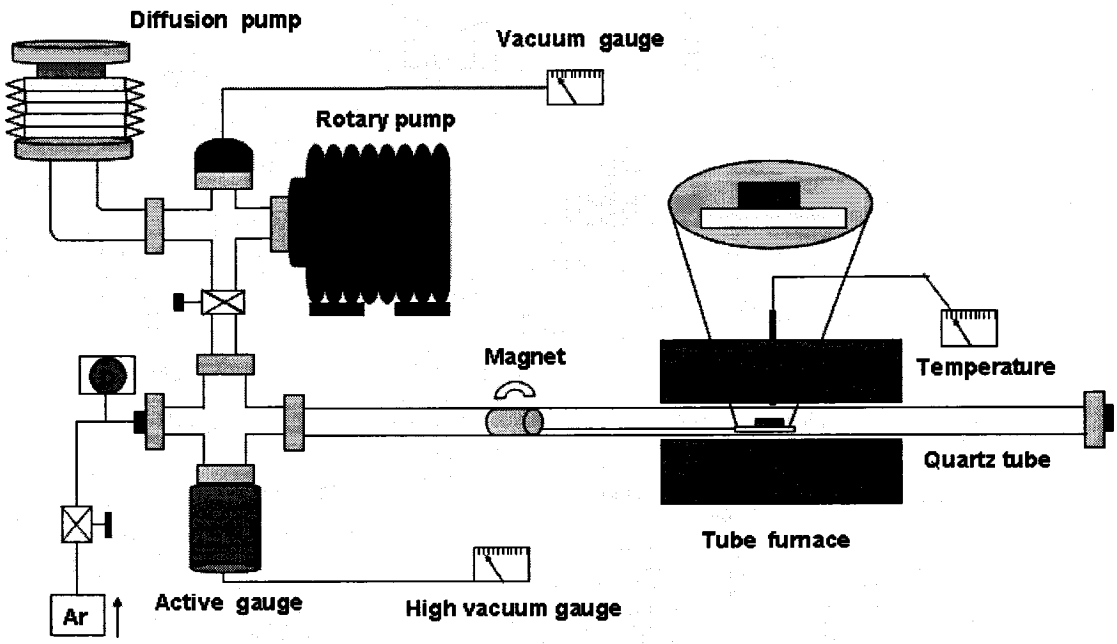

Figure 3.2: Schematic of the tube furnace used for annealing.

The furnace tube was evacuated with a rotary pump up to 100 mtorr and purged 4 times with Argon. Subsequently, the diffusion pump was started to achieve a vacuum of 1×10^{-7} torr. Once the system is at high vacuum, Ar gas was introduced to remove any remaining air that might promote the formation of undesirable oxides.

3.2 Characterization of the Prepared Alloys

3.2.1 X-Ray Diffraction (XRD)

Phase analysis was performed in both as-milled and annealed alloys in order to follow the phase evolution. The X-ray diffractometer consists mainly of three parts: a target material where the X-rays are generated, the specimen which is under study and the detector which collects the reflected X-rays and counts. The reflections coming from the specimen will be detected and the intensity of the counts will be collected for every specific position 2□. A Phillips APD-1700 X-ray diffractometer with Cu-Kα radiation was used with an accelerating voltage of 40 kV and a current of 20 mA, where scanning angles were ranging between 25° to 85°, with a step size of 0.01 and a scan rate of 1 step/second. For phase identification the purposes X'pert software (2004) "pattern treatments program" was used.

3.2.2 Scanning Electron Microscopy (SEM)

In some stages of the research, it was necessary to study the microstructure and surface morphology of the as-milled and annealed powders using JEOL JSM-840A SEM. Also, energy dispersive X-ray spectroscopy (EDS) was used along with the SEM in order to perform elemental analysis for the prepared alloys. The metallic alloys were produced in powder format, thus it was relatively easy to examine them for SEM since no gold coating was required to enhance conductivity of the materials under study. Powders were placed directly on a Cambridge stub and were inserted into

the beam column. To distinguish between elements in the SEM it was rather straight forward to differentiate between Al and Zr because of the pronounced difference in atomic number but in the case of Al and Mg it was difficult.

3.2.3 Transmission Electron Microscopy (TEM)

Transmission electron microscopy was used extensively in this research to characterize the nanostructures obtained in the resulting alloys in terms of particle size, crystallinity, internal structure and elemental distribution. In the TEM, when electrons are emitted into the electron gun it is accelerated toward the sample which has to be thin enough to allow passing of electrons and the generation of scatterings. Based on the intensity of penetrating and diffracting electrons a thickness contrast TEM image is formed. Additionally, bright- (BF) and dark-field (DF) images are used to measure crystallite size and to study structural defects[83]. Switching between BF and DF is accomplished by selecting specific electrons from the sample under study. If the transmitted electrons are collected only then the BF image is generated, while the DF image is generated if the scattered electrons are collected only.

In this research, TEM studies were carried out using a JEOL-2100HR instrument operating at an accelerating voltage of 200kV. The measurement of the interplanar spacing was performed using Fast Fourier Transform (FFT) procedure. The alloy powders were placed on a carbon grid coated with a 1-2 nm thickness polymeric membrane (commercial name is FORMVAR). This coating practice was performed to

modify the existing grid size in which the polymeric membrane will facilitate holding of the smaller powder particles.

3.2.4 Detection of Amorphous and Crystalline Phases Using XRD and TEM

Since XRD and TEM were used extensively in this research in characterizing the resulting alloys, the following figures show typical XRD patterns and TEM selected area diffraction patterns (SADP) for both completely crystalline and amorphous phases, in order to familiarize the reader with them.

Figure 3.3 shows a typical X-ray diffractogram for a crystalline material, showing sharp diffraction lines arising from the repeated reflection of crystalline planes satisfying the Bragg's law. In addition to that, SADP obtained for crystalline material by TEM is shown where it consists of diffraction rings. Starting from the center, where the electron beam is transmitted, every diffraction ring represents a reflection from distinct atomic planes, with the "hkl" Miller indexes growing outwards. Moreover, each diameter of the diffraction rings represents the interplanar spacing "d" which corresponds to a specific family of planes of a particular phase. The presence of specific crystalline materials can be detected from these d values by comparing these values to the data obtained from XRD cards.

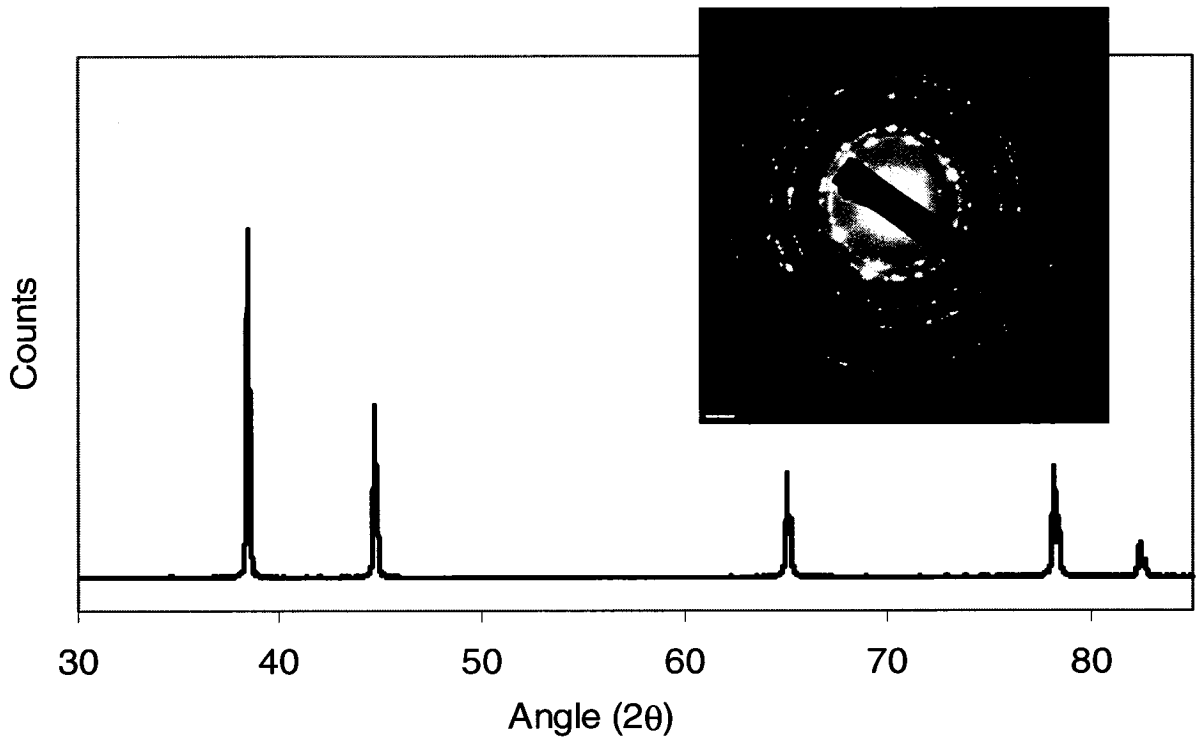

Figure 3.3: Typical XRD and TEM of fully crystalline material.

On the other hand, a typical XRD diffraction pattern for a fully amorphous material is presented in Figure 3.4, characterized by the lack of diffraction peaks. This absence of diffraction peaks is due to the presence of a distorted amorphous structure, which applies also to the SADPs obtained in the TEM shown in the same figure, manifested by the absence of crystalline long-rang order.

For the purpose of this study and due to the expected presence of both crystalline and amorphous phases, XRD analyses were complemented with high resolution TEM and SADPs, for a better qualitative characterization of nanocrystalline and amorphous

phases, since it is expected to see diffraction rings coexisting with the halo-diffraction patterns.

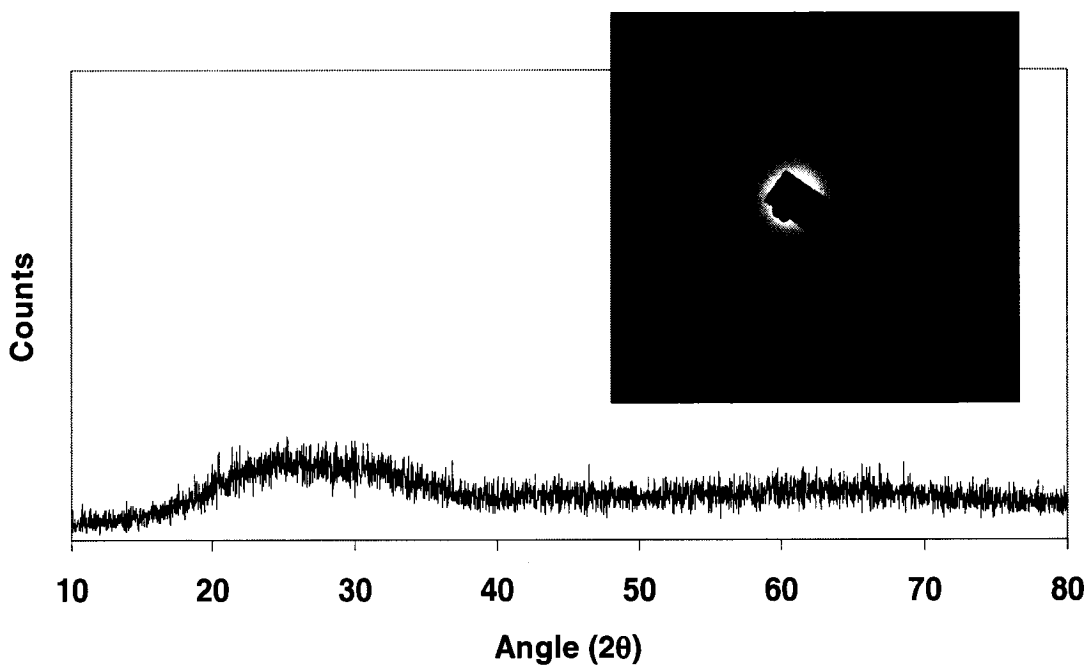

Figure 3.4: Typical XRD and TEM of fully amorphous alloy.

3.2.5 Particle Size Determination

In some cases, the average crystallite size was calculated using two methods. First, by fitting the non-overlapping diffraction peak profiles using the Scherrer procedure from XRD results. Additionally, direct TEM observation using bright- (BF) and dark-field (DF) images. These two procedures were used for comparison purposes in order to assess the indirect procedure of Scherrer with direct TEM observation. It is necessary to mention that in order to apply the Scherrer procedure to X-ray

diffractograms the peaks indicating the presence of solid solution should be clearly present. If these peaks cannot be seen on the XRD patterns, the procedure for crystallite size measurement cannot be performed and direct TEM observation is the only possible means of measuring the average crystallite size. However, direct TEM was used in most cases since it is more straight forward and more precise.

The procedure for calculating the average crystallite size using Scherrer equation has been detailed in Suryanarayana and Norton [84]. The reduction in crystallite size can be related directly to the broadening in the X-ray patterns in specific locations and thus allows for quantification. The broader the diffraction peak the smaller is the crystallite size of the material, which is mainly due to the fact that for smaller crystal structures there are less parallel planes available for sharp diffraction, hence broadening is observed. Nevertheless, the observed broadening into the peaks cannot be related directly to the broadening due to reduction in crystal structure. Other sources that cause broadening exist such as: the instrumental effect and lattice strain. Therefore, subtraction of these is essential in order to determine the crystallite size precisely. The following equations can be used for the calculation.

The broadening due to the instrumental error can be determined by running an annealed sample of the alloy under study and then subtracting the broadening of the obtained peaks "B_i". Hence,

$$B_r = B_o - B_i \quad (3.1)$$

Where B_o is the broadening from the material under study and B_r is the resulting broadening after subtracting the instrumental broadening. Thus, B_r is the broadening due to crystallite size and lattice strain. After that, the Scherrer equation can be used which is:

$$B_c = \frac{k\lambda}{L\cos\theta} \quad (3.2)$$

Where B_c is the broadening due to crystallite size reduction only, L is the crystallite size, k is a constant and λ is the wave length. Broadening due to lattice strain B_s can be represented by the relation:

$$B_s = \eta \tan\theta \quad (3.3)$$

Since $B_r = B_c + B_s$ (3.4)

And by substituting for the equations above and multiplying by $\cos\theta$:

$$B_r \cos\theta = \frac{k\lambda}{L} + \eta \sin\theta$$

Then by plotting the above equation in $B_r \cos\theta$ vs. $\sin\theta$

The intersection which is equal to $\frac{k\lambda}{L}$ can be depicted which facilitates the calculation of crystallite size *L*.

3.3 Compaction and Hardness Measurements

Hardness measurements of the resulting alloys have been undertaken in order to assess the mechanical properties as a function of the Zr concentration. Compaction of the as-milled powder was carried out by employing combined cold and hot compaction procedures. Figure 3.5 shows a photograph of a compacted powder sample of 20 mm in diameter along with the die used for this purpose.

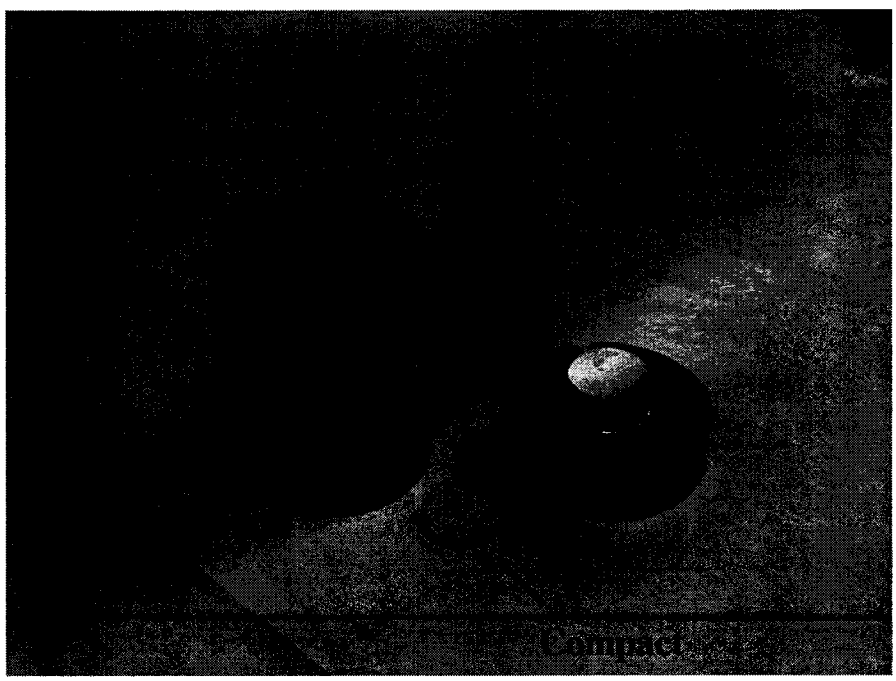

Figure 3.5: Compacted powders.

neglecting the presence of intermetallics since it is difficult to know the exact fraction. Vegard's rule can be written as:

$$v = \left(x\Omega^{o}_{Mg} + y\Omega^{o}_{Al} + z\Omega^{o}_{Zr}\right) \tag{3.5}$$

Where x, y and z are in atomic percentages.

As-milled powders were compacted using a cold-press at 1 GPa for 10 minutes. The sample and compaction die were placed in a hot-press and kept for 20 minutes at 400°C prior to compaction under 70 MPa for 10 minutes. This procedure is performed to obtain highly dense samples to facilitate hardness measurements using a Clark® LM-100AT microhardness tester with a load of 10 g.

It is important to mention here that the microhardness measurements were performed with great care taking into account the following concerns:

1. If there is particle collapse due to indentation, this reading is ignored. Nevertheless, we never had such incident which reassures the high density of the samples.
2. If there are large fluctuations in the hardness measurements, then this might indicate that the sample is not compacted enough, thus, taking hardness is not

suitable and compaction should be repeated. However, this case has not been encountered either.

3. The readings should be taken from locations far away in the material to avoid having local compacts and make sure that the material is showing no porosity.
4. Any distortion of the indentation (impressions) disqualifies the reading.

3.4 Research Methodology

The flow chart presented in Figure 3.6 shows the experimental procedure that can be followed. This procedure was used in all alloy systems using mechanical alloying to verify the possibility of forming nanocomposite material based on predetermined alloy constituents. Detailed description of this procedure will be given accompanied by all possible modification that can be made to develop a nanocomposite structure.

Once the alloy compositions and milling parameters are specified, the powders, and process control agent (PCA), were loaded in a sealed glove box under Ar atmosphere to prevent/minimize contamination by oxidation. Subsequently, the as-milled powders could be characterized by XRD, SEM, and/or TEM/EDS to verify the microstructure, i.e. completely amorphous, partly amorphous or completely crystalline phases. As-milled powders were subjected to annealing in order to study the stability of the obtained phases and the formation of equilibrium phases. In this research, particular emphasis was paid to obtain a nanocomposite structure comprising of

research, particular emphasis was paid to obtain a nanocomposite structure comprising of nanoparticles embedded in an amorphous matrix. This indicates that the formation of an amorphous phase is essential for this purpose.

From Figure 3.6, it can be seen that if a completely amorphous phase was obtained in as-milled samples, then these were subjected to controlled devitrification to nucleate nanometric crystals. Devitrification can be performed in the temperature range of 150-300°C for short periods of time depending on the system under study. On the other hand, if a partly amorphous phase or crystalline phases were obtained then further examination was needed to verify if they resembled a nanocomposite structure.

Adjusting the heat treatment procedure is very important to obtain the nanocomposite material and it can be altered until the desired microstructure is obtained. If a nanocomposite material is obtained, then it was possible to proceed to compaction and mechanical properties testing; otherwise either devitrification or adjustments of the milling parameters, such as milling time and ball-to-powder ratio is needed. Compaction should be performed also with great care to avoid coarsening of the nanometric grains. In general, compaction can be achieved by either hot- or cold-pressing. However, cold pressing was preferred to avoid excessive crystal growth.

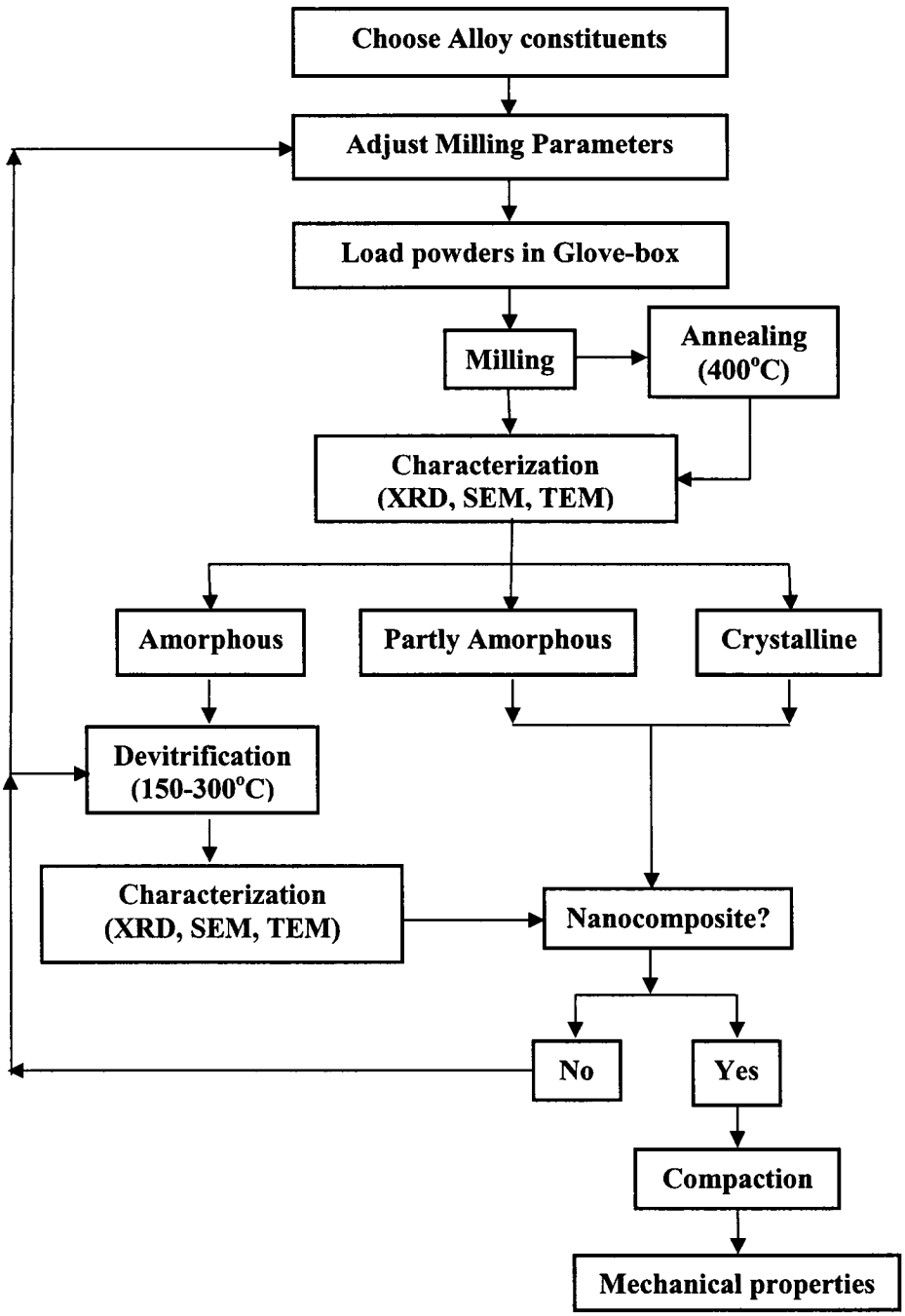

Figure 3.6: Flow chart showing the experimental procedure for the preparation of nanocomposites and possible characterization.

Chapter 4

Results and Discussion

4.1 Important Considerations in This Study

At the beginning of this section it is essential to address some key information that is useful for the discussion of this chapter. Since mechanical alloying is a non-equilibrium process, it is important to present some of the basic equilibrium phase diagrams in order to assess the departure from equilibrium obtained by employing mechanical alloying. Figure 4.1 shows the equilibrium Al-Mg phase diagram which clearly shows the presence of two main intermetallics, namely β-Al_3Mg_2 and γ-$Al_{12}Mg_{17}$. The β phase can be obtained for Mg concentrations between 38 and 41 at%, whilst the γ-phase can be produced at concentrations between 45 and 60.5 at%. As stated earlier, due to the nature of the alloying process, it is expected that these

intermetallic phases form at different Mg concentrations, which depends mainly on the milling conditions and phase stability.

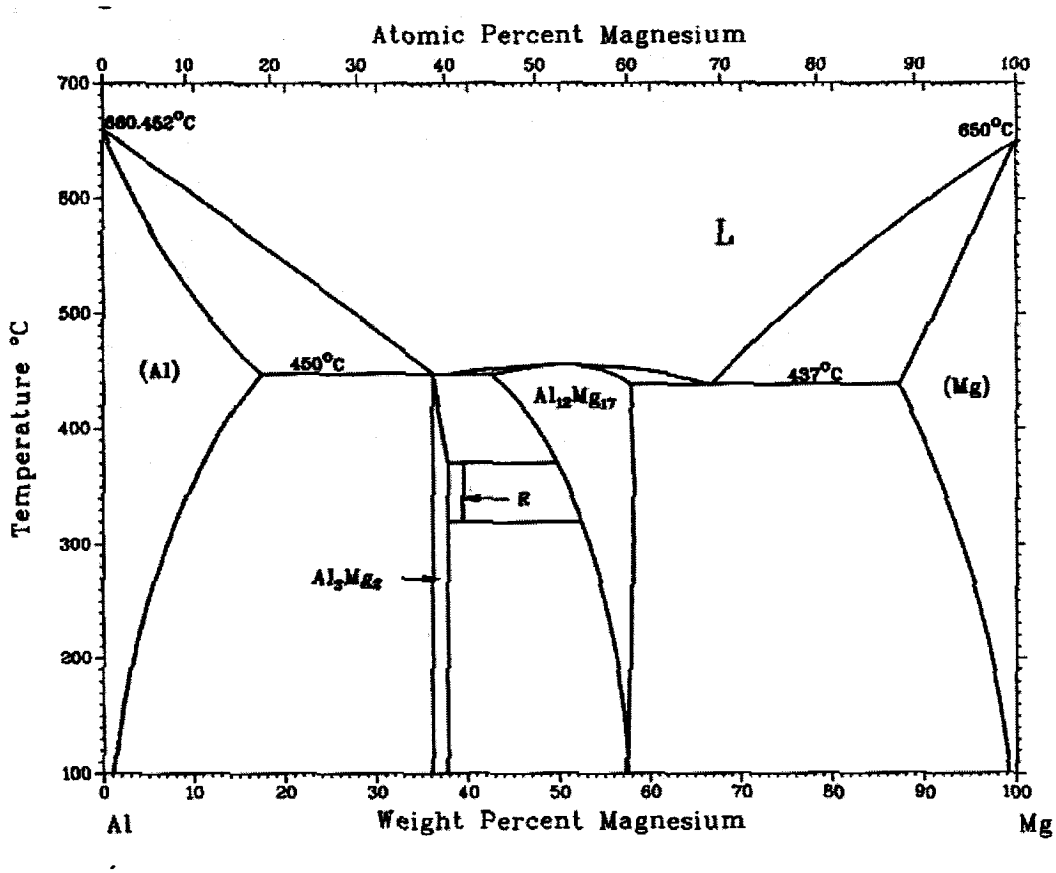

Figure 4.1: Al-Mg equilibrium phase diagram.

It is also useful to show the equilibrium Al-Zr diagram to show the equilibrium phases which is necessary to assess the departure from equilibrium by employing mechanical alloying. From Figure 4.2 it can be seen that the Al-Zr system is more complex compared to the Al-Mg. Since there exist many intermetallic phases exist in a narrow range of compositions, this makes the identification and characterization of these phases very challenging, and therefore information about their stability is

necessary. Some of these intermetallic phases nucleate only at higher temperatures in a metastable state and decompose upon slow cooling into higher stability intermetallics. Additionally, some of these intermetallics can be present in more than one crystal structure depending also on how the system is brought to room temperature. For instance, the tri-aluminide Al_3Zr can be present in either tetragonal DO_{23} or cubic Ll_2 crystal structures. The latter structure is considered as a higher temperature structure but can be preserved at room temperature through high quenching rates. This is beneficial for achieving improved mechanical properties at room temperature since the transformation to the equilibrium DO_{23} phase can cause embrittlement of the material.

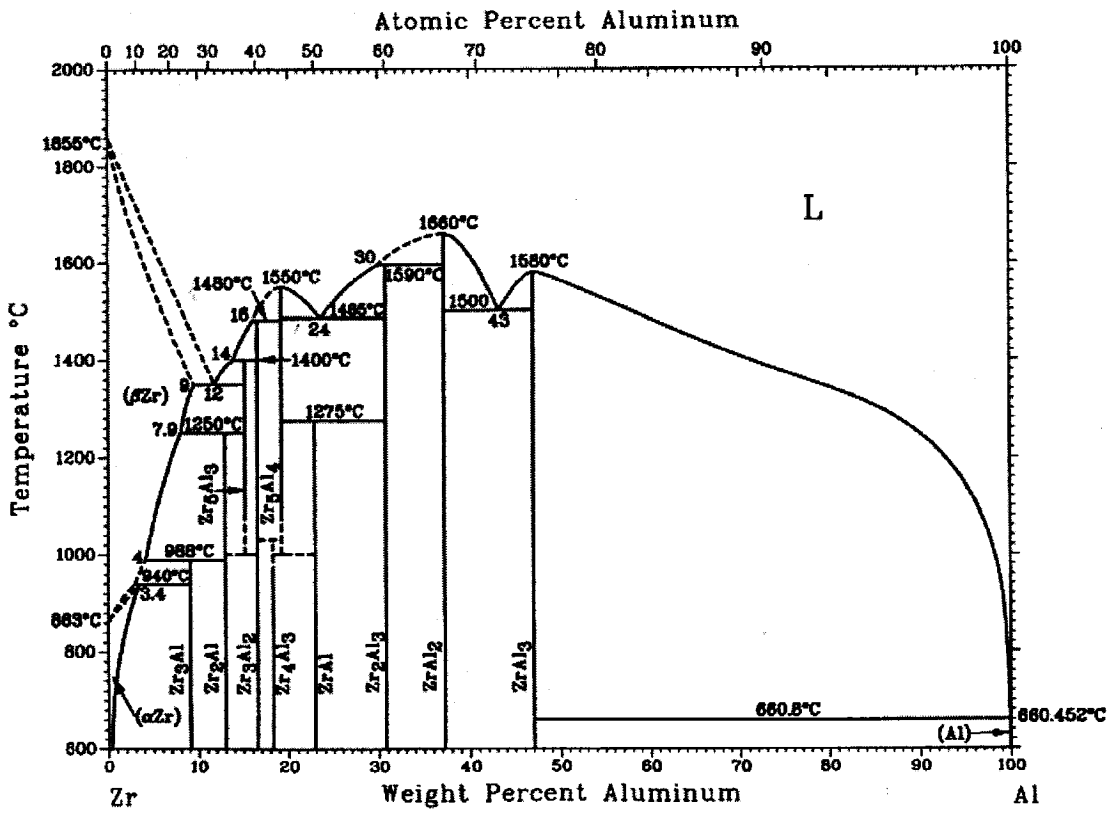

Figure 4.2: Al-Zr equilibrium phase diagram.

For the upcoming results and discussions, different categories of alloys will be presented separately. The sequence for results and discussion will be as follows:

1. X-ray diffractograms will be presented for both as-milled and annealed alloys followed by a discussion and comparison with the expected equilibrium phases. This step is essential in showing the resulting phases upon milling and to study the departure from equilibrium by employing mechanical alloying. In addition, the thermal stability of these phases was studied by comparing the metastable phases to those obtained after annealing.
2. The formation of the nanocomposite structure was examined using TEM, by investigating the presence of both amorphous and crystalline regions using SADPs and high resolution TEM. Moreover, the role of alloy composition on the formation of an amorphous phase will be assessed. Selected area diffraction patterns (SADPs) are presented from various locations of the material to locate the nanocomposite structure and assess the progress of amorphization.
3. Crystallite size measurements will be presented for both as-milled and annealed alloys. The crystallite size is another factor influenced by the Zr addition, and the role of Zr in retarding grain growth of the nanostructure will be highlighted.
4. Hardness values taken from different locations of the compacts to evaluate any improvement in mechanical properties will be presented as a function of Zr concentrations.

5. The aforementioned sequence of results and discussions will be presented for each category of alloys. However, it is important to mention that a detailed and thorough discussion will be given for the first category of alloys only. This is mainly to avoid repetitions since similar behaviour in terms of phase evolution might be observed from one group of alloys to another.
6. Finally, a general comprehensive discussion of all the results will be presented in order to evaluate the behaviour of all alloys prepared in this research and to draw overall conclusions. Additionally, the best alloy in terms of combining the most suitable structural stability along with mechanical properties will be highlighted.

4.2 Low Mg-Containing Alloys

This category of alloys was prepared in order to study the effect of adding a low content of Mg and varying the Al/Zr ratio, in nominal compositions according to $Mg_{10}Al_{90-x}Zr_x$ (where x: 0, 5, 20, and 35at%).

4.2.1 Phase Evolution Studies by XRD

X-ray diffraction patterns of the resulting as-milled and annealed alloys from this group are presented in Figures 4.3 and 4.4, respectively. As stated earlier, the Mg content was fixed at 10 at% for all the alloys, whereas the Zr concentration was varied to produce one binary and three ternary alloys. For the binary alloy, the presence of an Al(Mg) solid solution (SS), is shown by the clear shift of the α-Al peaks toward lower angles, caused by dissolution of the larger size Mg atoms into the Al matrix. The broadening of diffraction peaks is another feature that can be noticed, being indicative of the reduction in crystallite size and accumulation of strain in the material. However, neither the presence of Al-Mg intermetallics nor unalloyed Mg was revealed from the diffraction pattern which may suggest only complete solid solubility. Furthermore, upon annealing, the Al(Mg) SS was the only phase present; however, the diffraction peaks were slightly narrower due to stress relaxation and grain coarsening. These results agree well with previous findings [35] in which the α-Al solid solution was present in alloys containing up to 30 at.% Mg.

To study the phase evolution further and the possibility of forming nanocomposites as a result of adding a ternary glass-forming element, a series of alloys with different Zr concentrations was prepared. In the 5 at.% Zr alloy, some free Mg was present along with the Al(Mg)SS, suggesting that the solid solubility of Mg in Al decreases in the presence of Zr. This might be due to the substitution of some Zr for Mg and the formation of an Al(Mg,Zr) SS.

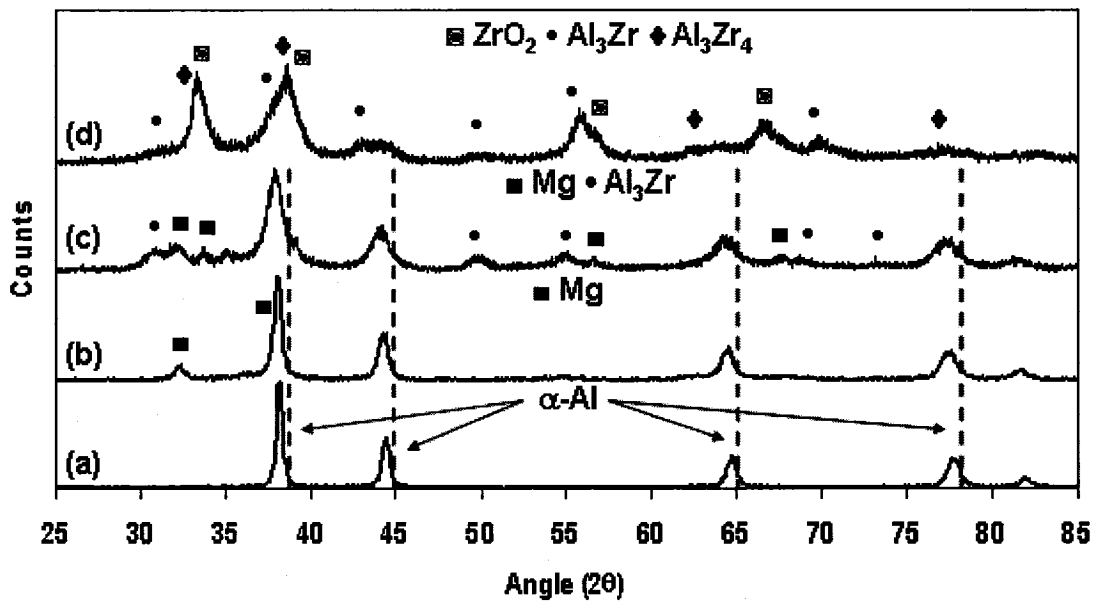

Figure 4.3: X-ray diffraction patterns of the low Mg concentration as-milled alloy powders: (a) 10Mg-90Al, (b) 10Mg-85Al-5Zr, (c) 10Mg-70Al-20Zr, (d) 10Mg-55Al-35Zr.

Upon annealing and due to the high affinity between Al and Zr, however, traces of the metastable Al_3Zr phase, having a cubic ordered structure Ll_2 were detected [85]. This phase can be synthesized directly by MA in alloys with higher Zr contents or by

annealing a solid solution with low Zr contents, as in this case. This highlights additional advantage of non-equilibrium processing in which it is possible to retain the Al_3Zr phase in the cubic ordered Ll_2 structure rather than the equilibrium tetragonal DO_{23} structure, which weakens the structure due to its embrittlement [16].

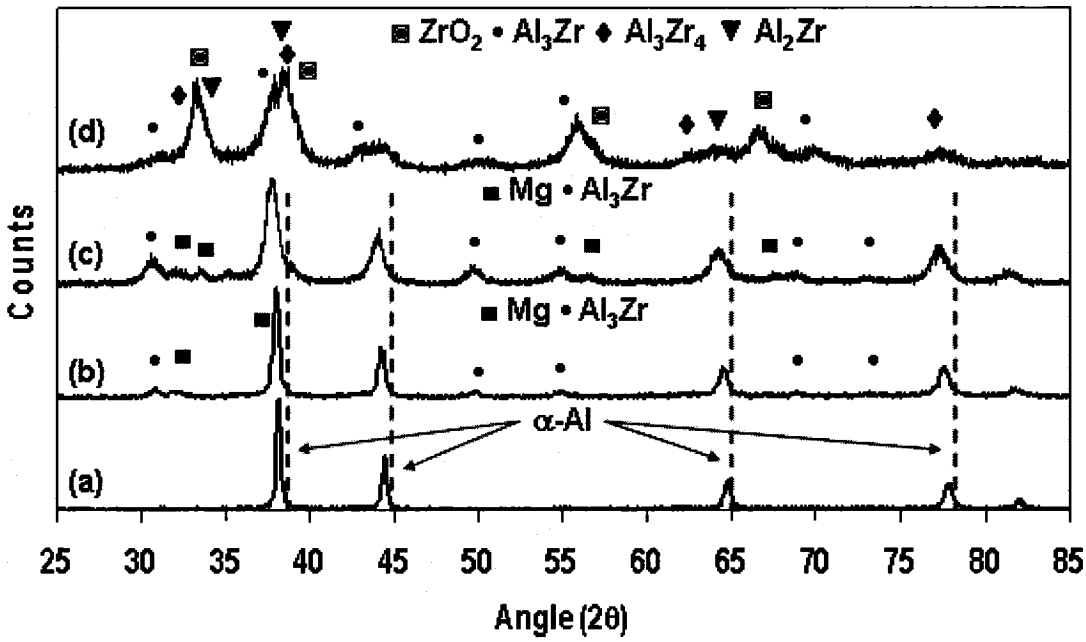

Figure 4.4: X-ray diffraction patterns of the resulting annealed alloy: (a) 10Mg-90Al, (b) 10Mg-85Al-5Zr, (c) 10Mg-70Al-20Zr, (d) 10Mg-55Al-35Zr.

Another feature observed in the XRD pattern is the apparent shift of peaks toward even lower angles and increased broadening as the Zr content increases. This indicates that the addition of Zr causes additional structural refinement and substantial structural disruption compared to the binary alloy. Furthermore, for 20 at.% Zr, the presence of unalloyed Mg and the formation of the Al_3Zr intermetallic in the as-milled powders

were clearly evident from X-ray diffractograms. The small difference in lattice parameter and the same crystal structure between the Al and Al_3Zr phases seem to facilitate the coherent precipitation of this metastable phase from the Al matrix. Nevertheless, no significant changes were observed in the annealed powders except for apparent peak narrowing.

In comparison with alloys with lower Zr content, the addition of 20 at.% caused further reduction in crystallite size and even larger structural disorder, as seen from the XRD peak width. This trend of continuous refinement in crystallite size and the increased shift towards lower angles as the Zr content increases was not observed in the case of 35 at% Zr. The higher Zr-containing alloys show clear evidence of oxidation, along with some Al-Zr intermetallics, i.e. Al_3Zr and Al_3Zr_4. These two phases showed good stability after annealing, together with the appearance of the Al_2Zr phase, which is a more stable intermetallic as observed from the equilibrium Al-Zr phase diagram.

Since crystallite size measurements by XRD can be influenced by the presence of lattice strain and other effects, direct TEM observations were carried out to determine structural refinement as a function of the Zr content. Further, due to the higher resolution of this technique, it was also possible to observe the nanocomposite formation and partial amorphization as a function of the Zr concentration.

4.2.2 TEM Studies

TEM was used to carry out more in-depth examination of the alloys with regard to their nanostructural nature and the presence of an amorphous phase. Figure 4.5 shows a TEM image of the binary alloy of nominal composition $Mg_{10}Al_{90}$. Additionally, the selected area diffraction pattern (SADP) taken from the center of this particle "circled region" is shown as an insert.

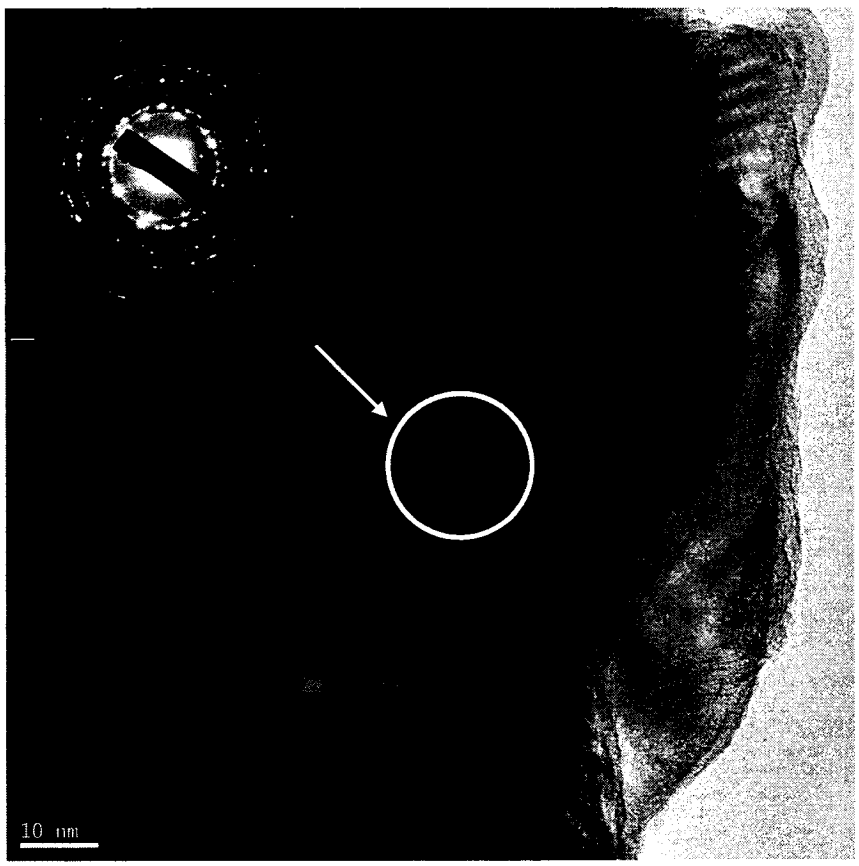

Figure 4.5: TEM image for the as-milled binary alloy 10Mg-90Al powders, showing complete crystallinity.

It can be clearly seen from the diffraction pattern that the binary alloy shows no presence of an amorphous phase which is manifested by the existence of clear reflections forming diffraction rings. These rings correspond to the Al(Mg) solid solution that was revealed previously by XRD of both as-milled and annealed alloys. This confirms the difficulty of forming an amorphous phase by milling binary Al-Mg alloys under the existing milling conditions.

Further investigation of the possible existence of small fractions of amorphous phases in this alloy was carried out using high resolution TEM (HR-TEM), shown in Figure 4.6. From the HR-TEM image the presence of ordered atomic planes can be seen, with an interplanar distance of 0.21 nm, corresponding to the (200) plane of the Al(Mg) SS. This confirms the diffusion of Mg into Al to form the solid solution since an enlargement of the interplanar spacing is obtained by comparison with the equilibrium value for Al, which is 0.2024 nm.

A bright field image of an alloy particle containing 5at.% Zr is shown in Figure 4.7 to study the effect of Zr addition on the formation of nanocomposite structure that might contain an amorphous phase. The EDS analysis of this particular alloy was taken from the center of several particles in order to assess any fluctuation in composition from the starting material. A typical EDS is presented in the same figure along with the corresponding selected area diffraction pattern (SADP) of the alloy containing 5 at.%Zr, taken from the center of a particle (circled area). It can be seen from the diffraction pattern (DP) that the continuous rings reveal the presence of a

highly crystalline material and the existence of an amorphous phase cannot be inferred from this DP. Therefore, the Al-Mg binary alloy and the one containing 5 at.%Zr did not apparently show the presence of amorphous phase.

Figure 4.6: High resolution TEM image of the binary alloy showing complete crystallinity and interplanar spacing d.

This agrees with previous studies performed in Al-Mg binary alloys [9] in which no amorphous phases were detected without the addition of a ternary glass-forming element. However, it should be stated that the amount of the glass former depends on the system under study. As will be shown later, ternary alloys containing higher Zr concentrations showed a nanocomposite structure with SADP images showing qualitatively a larger volume of the amorphous phase. It is important to mention also that EDS analyses of some selected regions of the ternary alloy showed no considerable compositional gradient, and the calculated average compositions are close to the nominal starting powder mixtures. However, the individual compositions of the crystalline and amorphous phases were not resolved.

A TEM image of a typical particle of 20 at.%Zr is shown in Figure 4.8. Additionally, the EDS analysis of the particle is shown, along with SADPs taken from the center (labelled "A") and corner (labelled "B") of the particle are shown in the same figure.

It can be seen that the diffraction pattern taken from location "A" reveals the presence of crystalline diffraction spots with no clear presence of an amorphous phase, which might be due to the higher thickness of the center of the sample. Furthermore, by obtaining the SADP of one edge of the sample (labelled "B") a typical halo-diffraction pattern is shown along with some crystalline spots indicating the presence of an amorphous phase coexisting with crystalline particles, i.e., a nanocomposite structure.

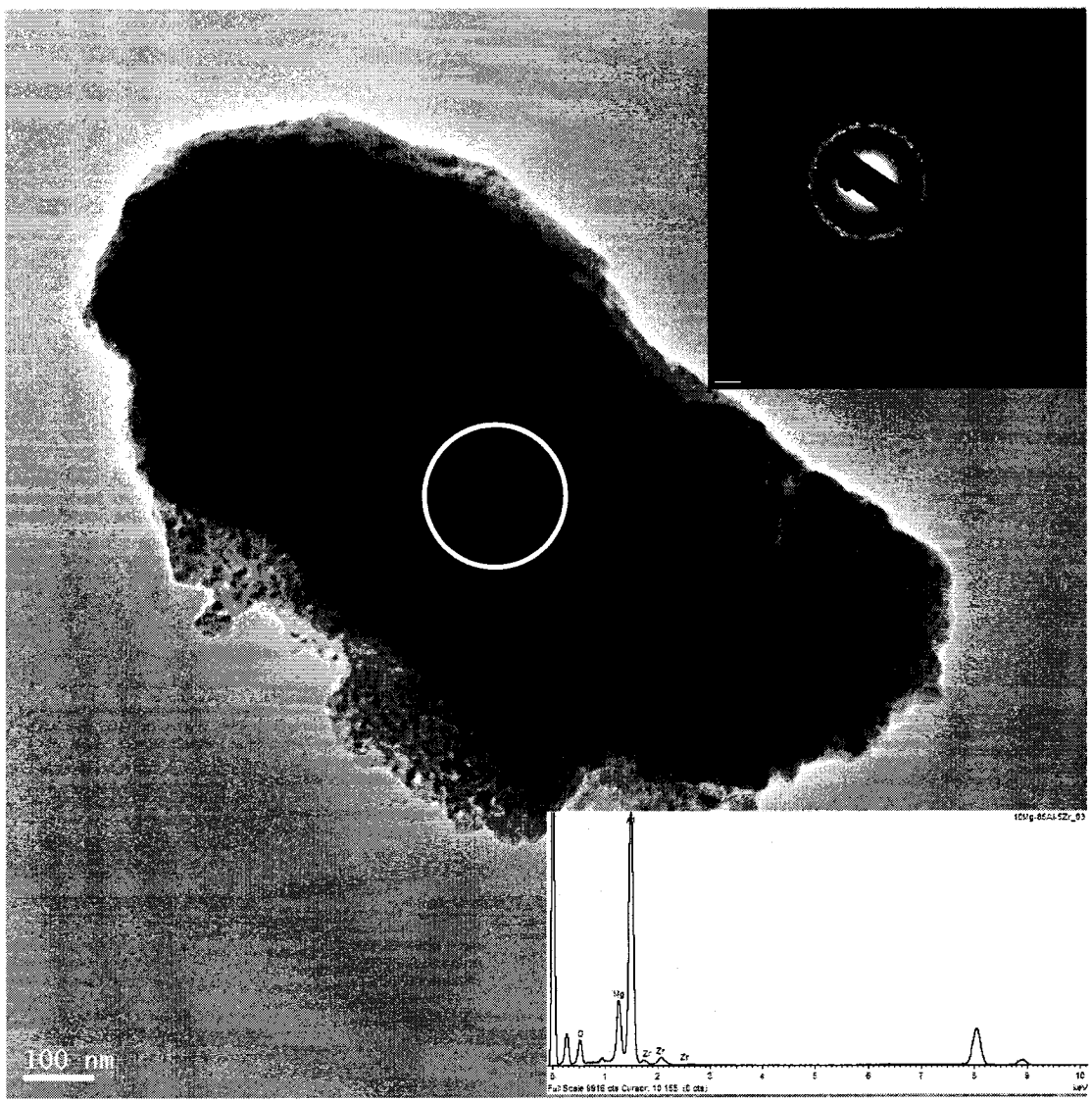

Figure 4.7: TEM image of an as-milled 10Mg-85Al-5Zr alloy particle along with EDS and SADP of the center.

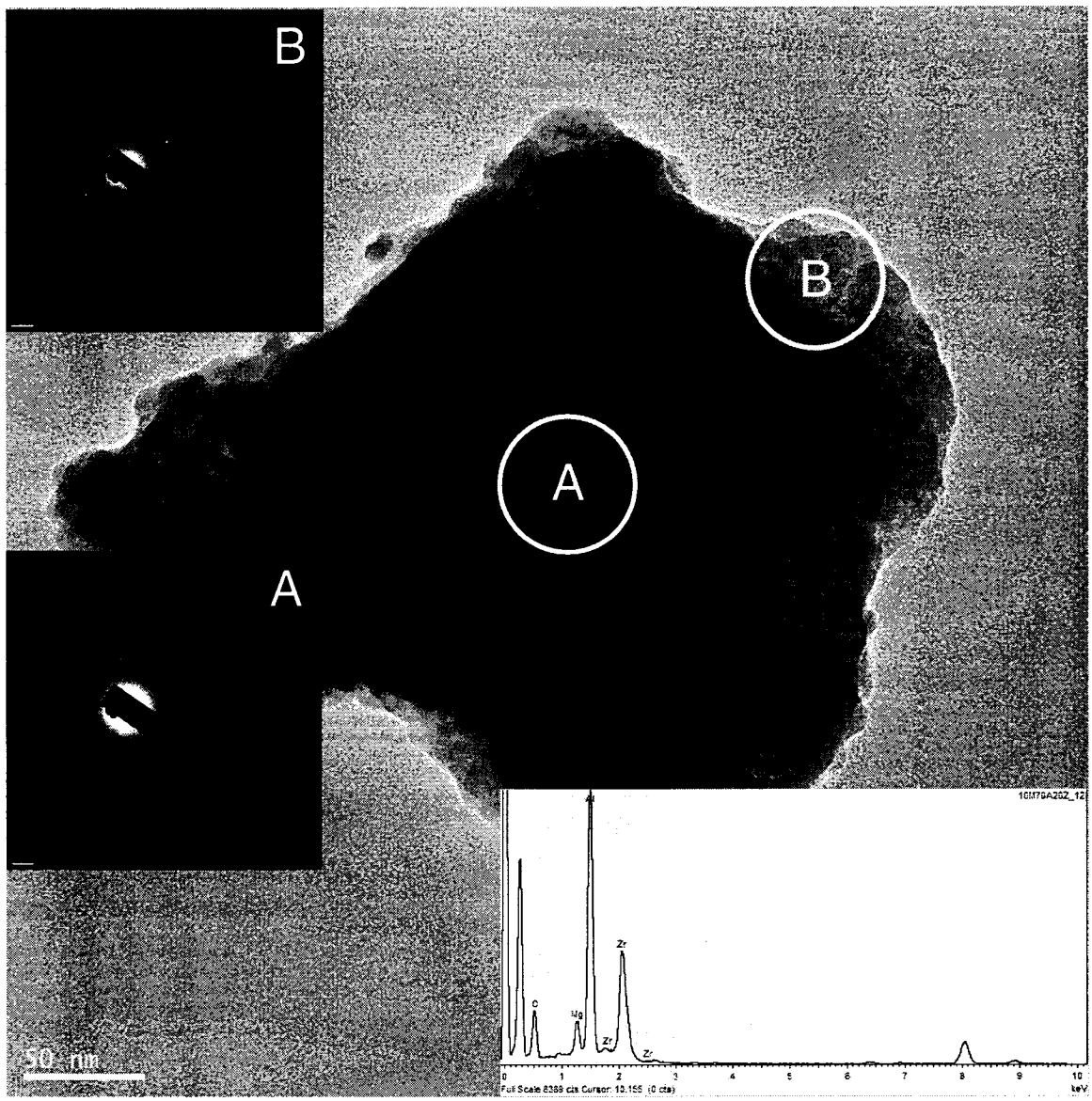

Figure 4.8: TEM image of as-milled 10Mg-70Al-20Zr, along with EDS and SADP from the center and corner locations. Note: the higher degree of amorphization of region B.

A high-resolution image of a selected edge region is shown in Figure 4.9 revealing the presence of a crystalline phase, with an interplanar spacing d = 0.213 nm, coexisting with an amorphous phase.

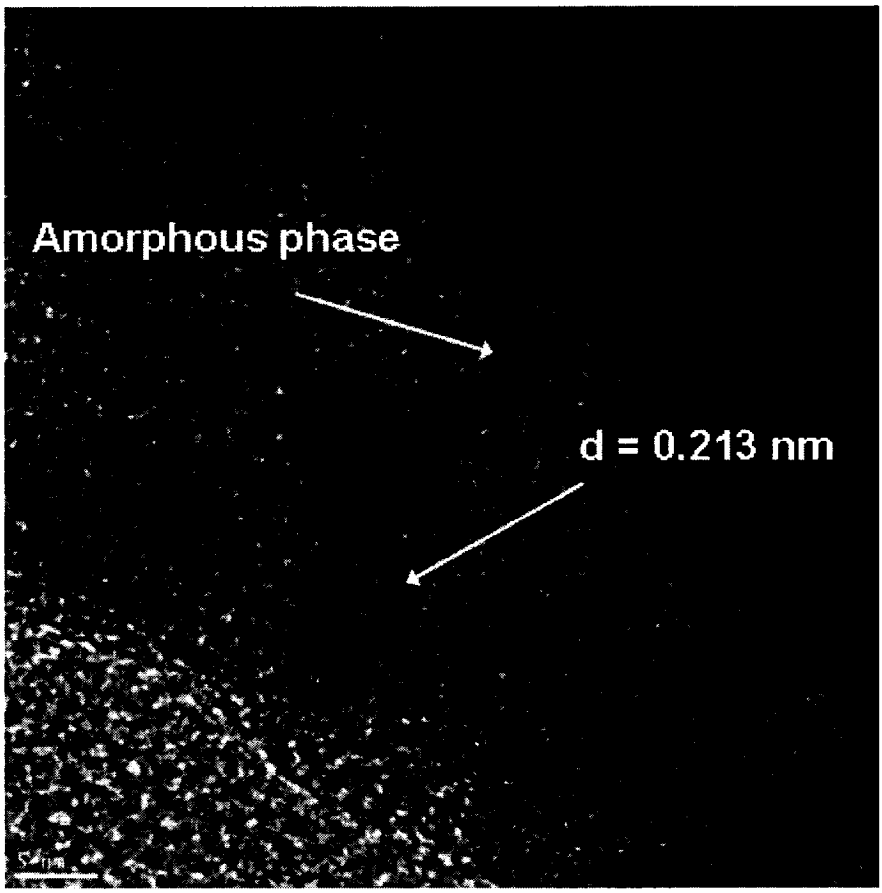

Figure 4.9: HR-TEM image of a region of the Al-10Mg-20at% Zr alloy showing the coexistence of nanocrystals and amorphous phase.

The HR-TEM image clearly shows regions of structural disorder, likely having an amorphous structure. In addition, crystalline regions showing clear atomic planes can be seen interspersed in the amorphous regions. This suggests the presence of a nanocomposite structure comprising amorphous and crystalline phases in different volume fractions. These observations confirm for the first time that such a structure can be obtained in the MAed Al-Mg alloys and the specific role of Zr in facilitating the development of a nanocomposite structure [86].

Referring to Figure 4.8 and the corresponding SADPs, it is reasonable to comment that the thicker part of the particle has experienced less deformation in comparison to the thinner part. Consequently, the thinner region has become amorphous while the thicker part continued to be highly crystalline, for this particular composition. Accumulation of sufficient defect density raises the free energy of the crystalline phase above that of the amorphous phase, thus facilitating the preferential stabilization of the amorphous phase [87].

A TEM image of the alloy with the maximum Zr concentration of 35 at% is shown in Figure 4.10 in addition to an EDS analysis and SADPs taken from two locations. The presence of a nanocomposite structure comprising nanocrystals and amorphous phases is confirmed from these images. This is manifested by the coexistence of both crystalline diffraction spots and halo-diffraction regions in the diffraction pattern taken from the corner of the particle. This indicates that for this type of alloys increasing the Zr concentration to values exceeding 20at% result in the formation of a nanocomposite structure with a pronounced fraction of amorphous phase even in the center of the particle.

In order to highlight the role of Zr in promoting the presence of an amorphous phase in these alloys, the corresponding SADPs for different Zr concentrations are shown in Figure 4.11. It can be seen that as the Zr concentration increases into the alloy so does the degree of amorphization; diffraction rings become less pronounced and the formation of the diffuse-halo becomes more evident, which can also be seen

from XRD patterns in Figure 4.3. However, it cannot be concluded from these DPs that the alloy containing 35 at.%Zr has a grater fraction of amorphous phase than the one containing 20 at.%Zr.

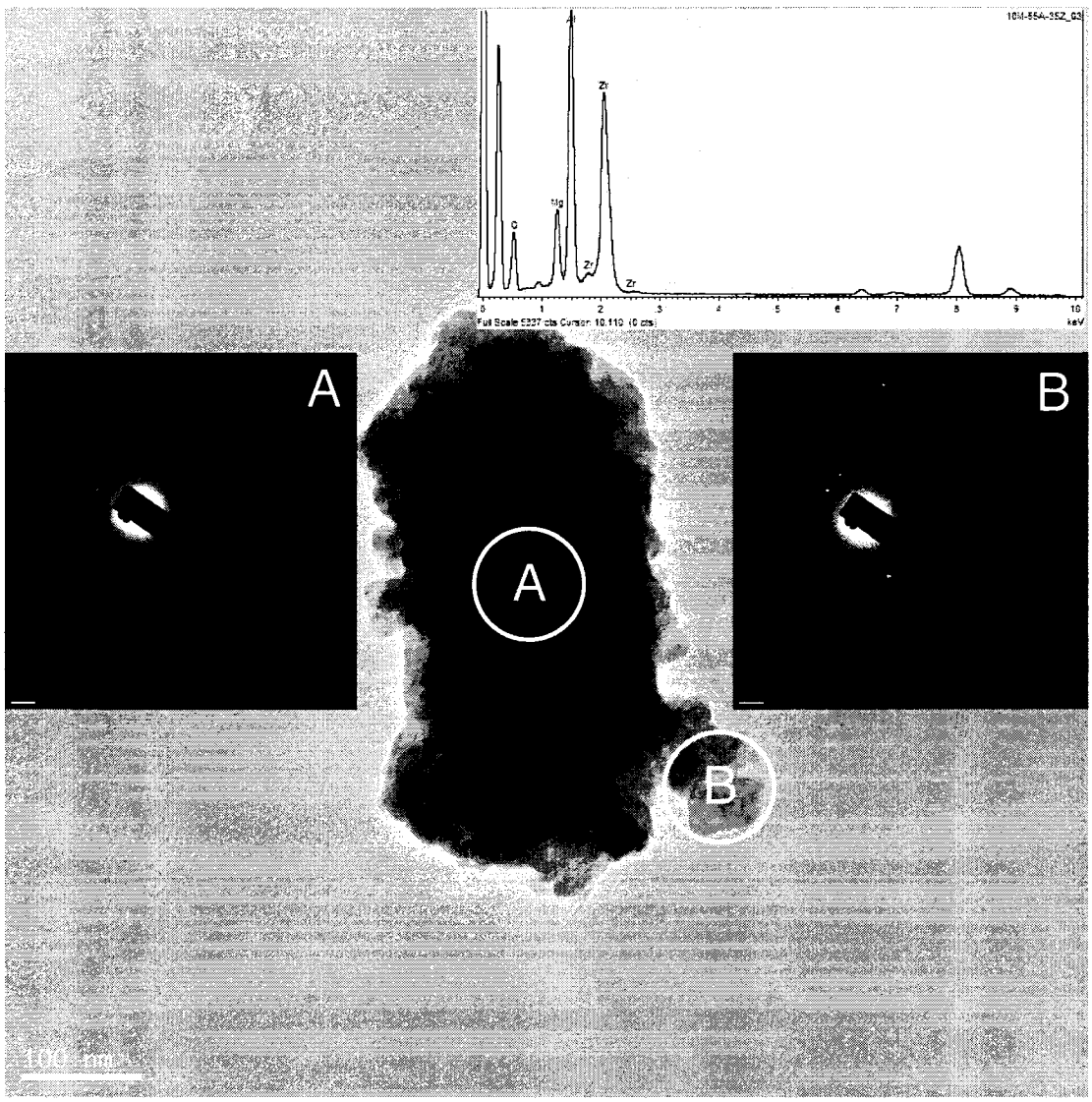

Figure 4.10: TEM image of as-milled 10Mg-55Al-35Zr showing EDS and SADPs of two locations (center and corner). They reveal the existence of a nanocomposite structure.

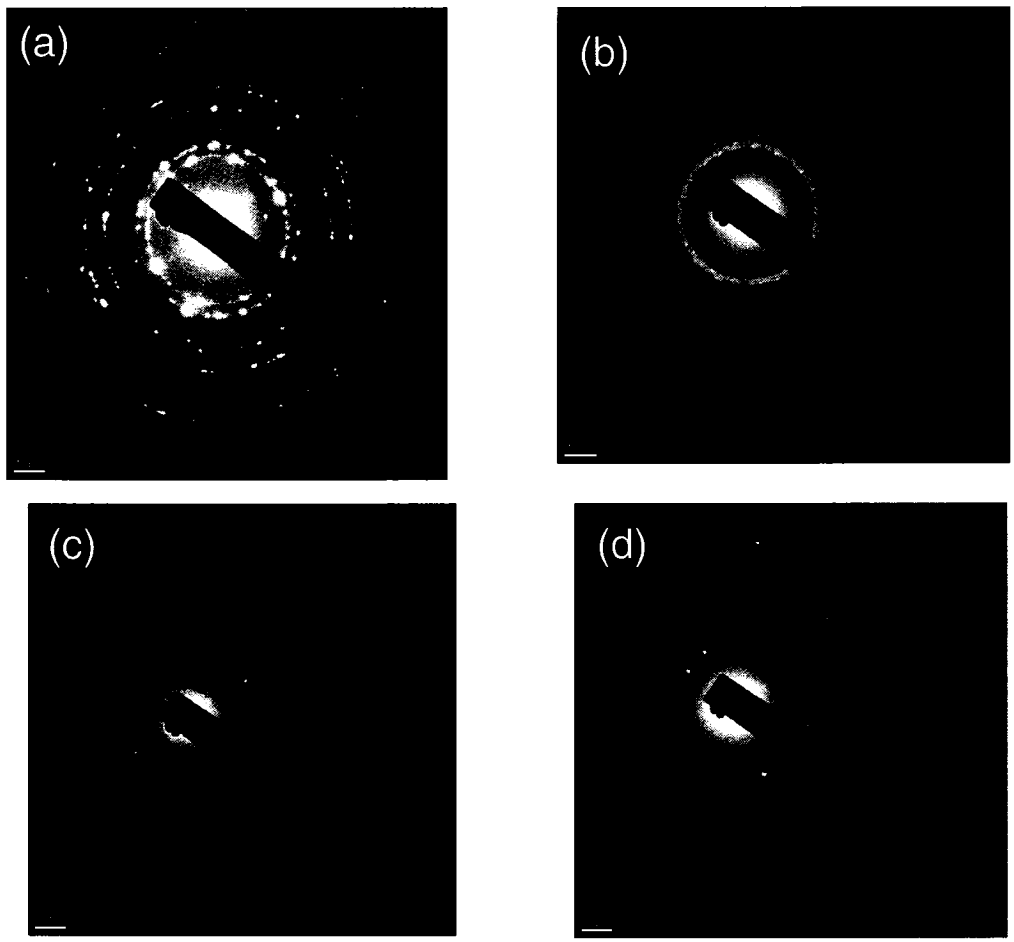

Figure 4.11: Comparison between SADPs of the Low Mg-containing alloys: (a) 10Mg-90Al, (b) 10Mg-85Al-5Zr, (c) 10Mg-70Al-20Zr, (d) 10Mg-55Al-35Zr.

4.2.3 Crystallite Size Measurement

The crystallite sizes of the resulting alloys in both as-milled and annealed conditions at different Zr concentrations are shown in Figure 4.12. The crystallite size measurements were carried out using both the Scherrer procedure from XRD patterns and direct TEM observation using both dark- (DF) and bright-field (BF) images. However, for the alloy containing 35at%Zr, measurements were taken using only DF

images since the absence of the solid solution peaks from X-ray diffractograms did not facilitate the application of the Scherrer procedure.

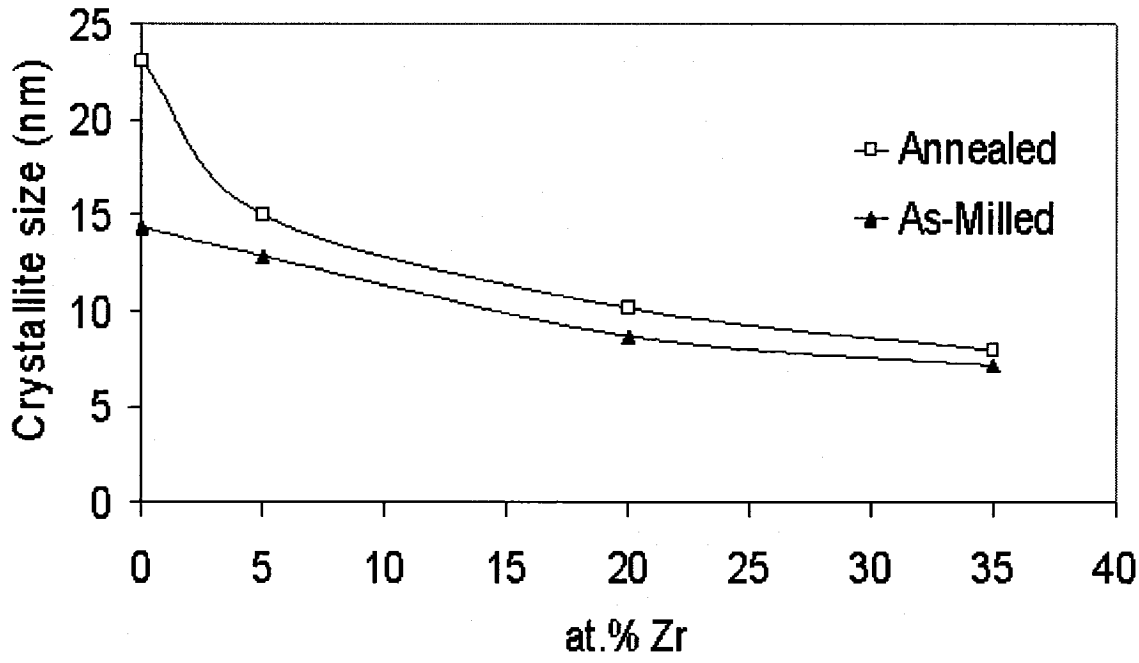

Figure 4.12: Crystallite size measurements for different Zr concentrations for as-milled and annealed alloys, highlighting the role of Zr in the refinement of the crystalline structure.

It can be seen that a reduction in crystallite size is achieved as the Zr content increases, showing an asymptotic behaviour for both as-milled and annealed powders. One interesting observation is the apparent stability of the grain structure as the Zr content increases. In fact, Zr seems to contribute to the stability of the nanocrystals and the larger the amount added, the less the post-annealing grain growth. The measured average crystallite size for the binary Al-10%Mg alloy was close to 15 nm,

which is smaller than previously reported for Al-5%Mg, being close to 26 nm [38]. This could be due to the higher Mg concentration into the alloy contributing further to the refinement in crystallite size [88]. However, these observations need more detailed study in order to highlight the role of minor Mg addition in the final crystallite sizes of the synthesized alloys.

The measurement of crystallite sizes were carried out using direct TEM observation from both bright field (BF) and dark field (DF) images. The crystallite size was determined based on the average values from images like those shown in Figures 4.13 for the $Mg_{10}Al_{55}Zr_{35}$ alloy in both as-milled and annealed conditions.

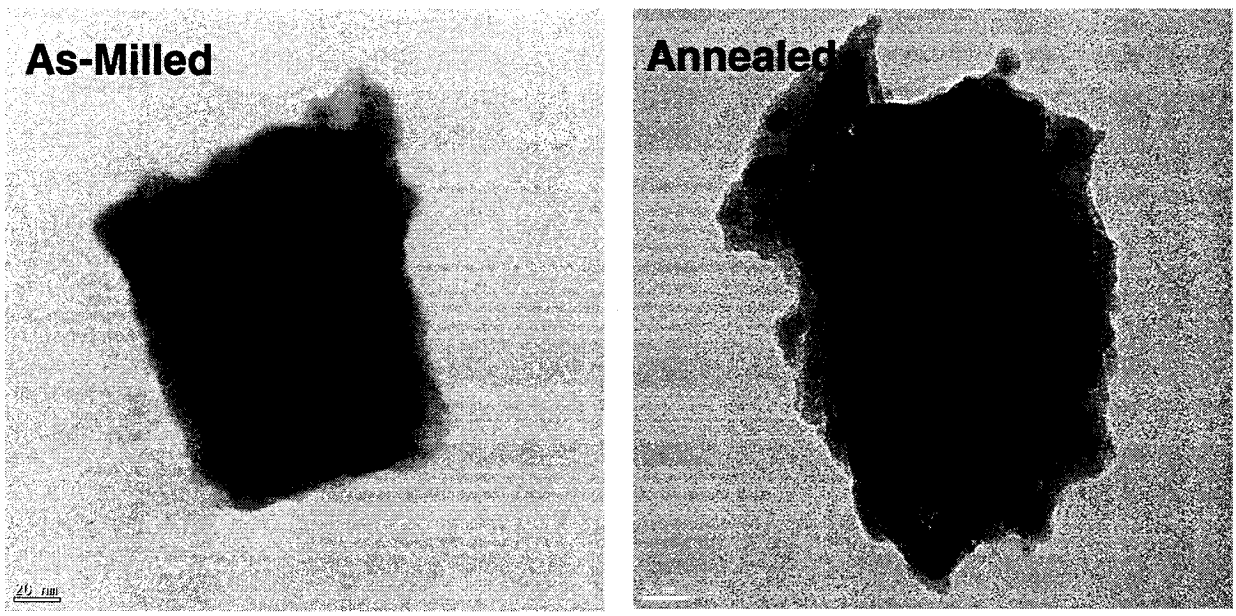

Figure 4.13: Bright field TEM images showing crystallite size for as-milled and annealed 10Mg-55Al-35Zr alloy.

It can be seen from these images that there is indeed a slight increase in crystallite size caused by annealing. However, measurements were taken with great care and in magnified images to have more in depth assessment of grain growth.

Regarding the comparison between the results obtained from the Scherrer method and direct TEM observations, it was noted that the crystallite measurements obtained using the former are larger by almost 6 % (see Appendix–B). This might be due to the fact that measurements by XRD depend primarily on the best fit of non-overlapping diffraction peaks, directly relating the broadening of the peaks to the reduction in crystallite size. This would be subject to several measurement errors in terms of determining the values of the full width at half maximum (FWHM). Furthermore, the best precision obtained in crystallite size determination by XRD is about ±10% [84].

4.1.4 Hardness Measurements

The hardness measurements of the resulting alloys were taken in order to assess the influence of Zr on the mechanical properties. The hardness values obtained from compacted samples are shown in Figure 4.14, showing a continuous increase in hardness up to 20at.%Zr. However, the value almost doubles for a Zr content of 35 at.%, which might be due to the presence of the zirconium oxide that, due to its hardness, renders the material significantly harder. However, further work is needed to investigate the dependence of hardness values on milling time and to correlate the

effect of crystallite size reduction with the obtained improvement in mechanical properties.

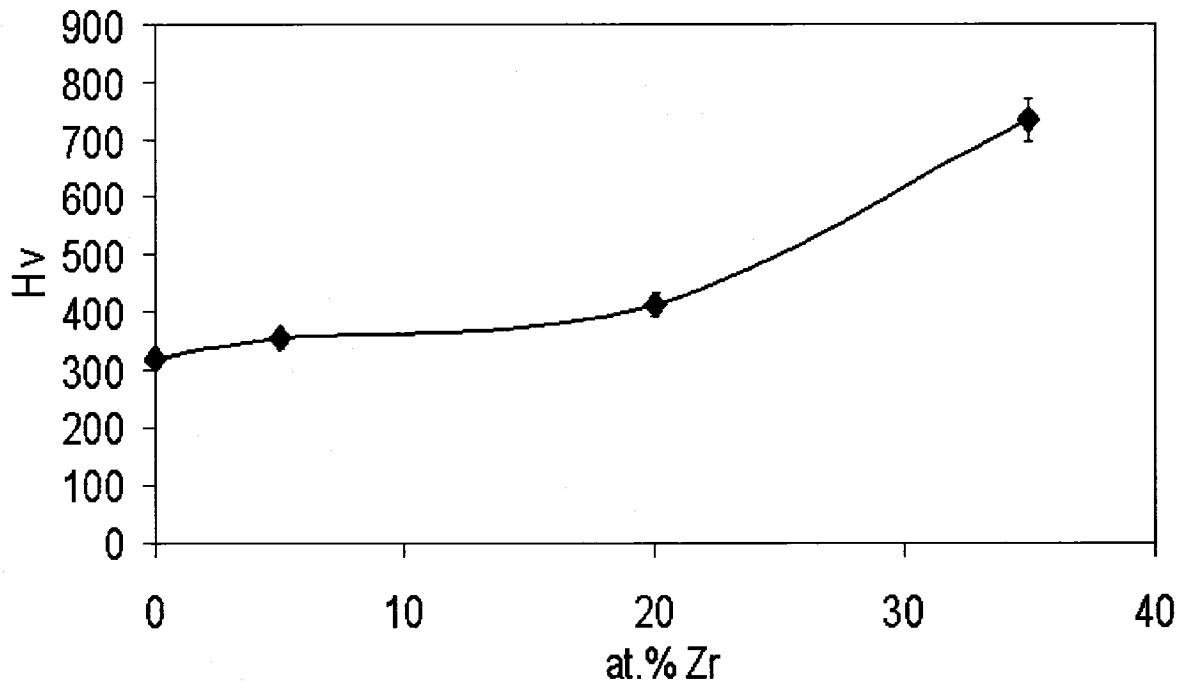

Figure 4.14: Variation of hardness with Zr concentration, showing the beneficial effect of Zr.

4.3 High Mg-Containing Alloys

In this category of alloys the concentration of Mg was maintained at 40 at.% producing alloys of nominal compositions according to $Mg_{40}Al_{60-x}Zr_x$ (*x = 0, 5, 20 and 35 at.% Zr*).

4.3.1 XRD Studies

Phase evolution of as-milled *High Mg Alloys* is shown in Figure 4.15 while the corresponding XRD patterns of heat-treated alloys are shown in Figure 4.16. In the binary $Mg_{40}Al_{60}$ alloy, the main phase found for as-milled powders was an Al(Mg) solid solution (SS), with the exception of traces of γ-$Al_{12}Mg_{17}$, which then transformed into the equilibrium β-Al_3Mg_2 after annealing. These results agree well with previous findings [34, 35] in which the β-phase was formed at this Mg concentration, only after annealing, due to the complexity of the phase and its larger lattice parameter compared to γ-phase. This indicates the need for higher energy to allow for the formation of this phase.

When 5at.% Zr was added to the alloy, it forced Mg to precipitate out of SS with the consequence formation of γ-$Al_{12}Mg_{17}$. This can be related to the presence of an Al(Mg,Zr)SS, which formed after heat-treatment. The γ-phase was also identified after heat-treating the alloy, indicative of the thermal stability of this phase. In addition, the

Al_3Zr intermetallic with a cubic Ll_2 crystal structure was also formed due to the nature of the non-equilibrium processing [16].

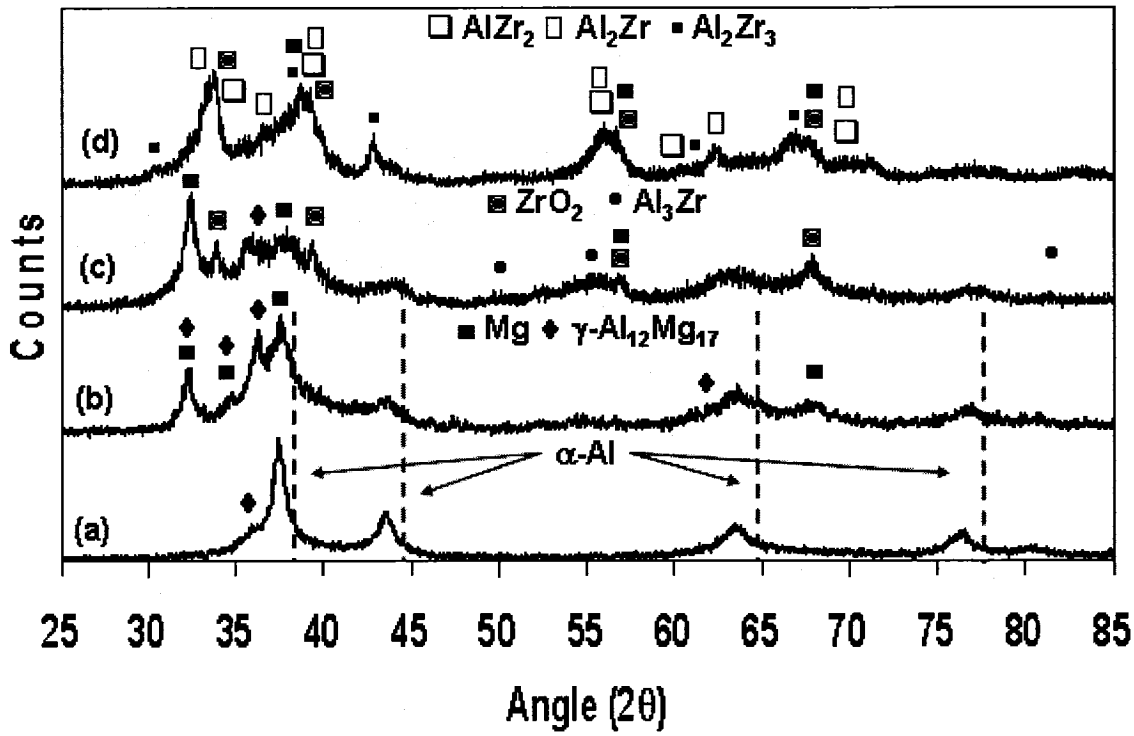

Figure 4.15: XRD patterns for as-milled Al-Mg-Zr alloys: (a) 40Mg-60Al, (b) 40Mg-55Al-5Zr, (c) 40Mg-40Al-20Zr, (d) 40Mg-25Al-35Zr.

Upon increasing the Zr concentration to 20at% the SS disappeared, giving way to Al_3Zr, some unalloyed Mg and small traces of the γ-$Al_{12}Mg_{17}$. Moreover, some Zr oxidation was detected, which is attributed to the higher affinity between Zr and O. Upon annealing, unalloyed Mg and Al_3Zr are still present, and the volume fraction of γ-$Al_{12}Mg_{17}$ increased slightly. The Al-Zr intermetallic showed good thermal stability and no phase transformation was observed. When Zr concentration was increased

further to 35at%, some Al-Zr intermetallics appeared after milling, which then transformed into the more thermodynamically stable phases upon annealing. Along with the equilibrium Al_2Zr phase, other non-equilibrium phases, i.e. $AlZr_2$ and Al_2Zr_3 were observed. Upon milling, some unalloyed Mg and ZrO_2 traces were detected for this composition as well. After heat-treatment, the $AlZr_2$ phase disappeared, suggesting low stability, whereas the other phases remained. No Al-Mg intermetallics were found to form at Zr concentrations exceeding 20 at%, which reflects the higher affinity of Zr for Al.

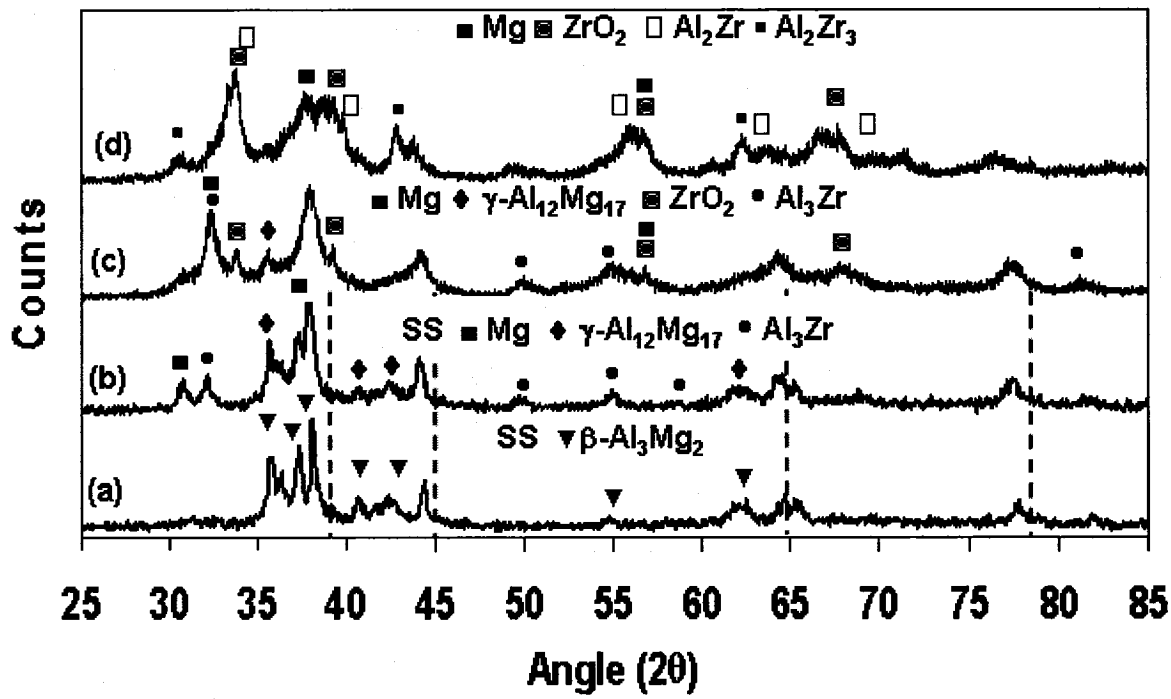

Figure 4.16: XRD patterns for annealed Al-Mg-Zr alloys: (a) 40Mg-60Al, (b) 40Mg-55Al-5Zr, (c) 40Mg-40Al-20Zr, (d) 40Mg-25Al-35Zr.

4.3.2 TEM Studies

As in the previous series of alloys, the formation of nanocomposite alloys having an amorphous phase was not evident from the XRD patterns; therefore, TEM studies were carried out. Figure 4.17 shows a TEM image of a particle of composition $Mg_{40}Al_{60}$. Moreover, selected area diffraction patterns (SADPs) where also taken from two different regions of the particle in order to verify the possible presence of amorphous phases, these locations labelled "A" and "B" are shown in the same figure. It can be seen that both DPs show clear diffraction rings indicating high crystallinity of the sample.

The TEM micrograph of the alloy containing 5 at.%Zr is shown in Figure 4.18 along with the EDS analysis taken for the whole particle the corresponding SADP images for both centre and corner areas "A" and "B", respectively.

The presence of an amorphous phase for this alloy is not evident from the SADP images due to the absence of a halo-like pattern. To further investigate the presence of an amorphous phase, high resolution TEM images were taken and the interatomic spacings were calculated using Fast Fourier Transform (FFT) and shown in Figure 4.19. Again, there is no clear indication of the presence of an amorphous phase, but only a polycrystalline material is inferred from the SADP image, with interatomic spacing of 0.209 nm. Thus, for both binary and ternary alloys containing 5 %Zr in this series of alloys, no clear presence of an amorphous phase was found.

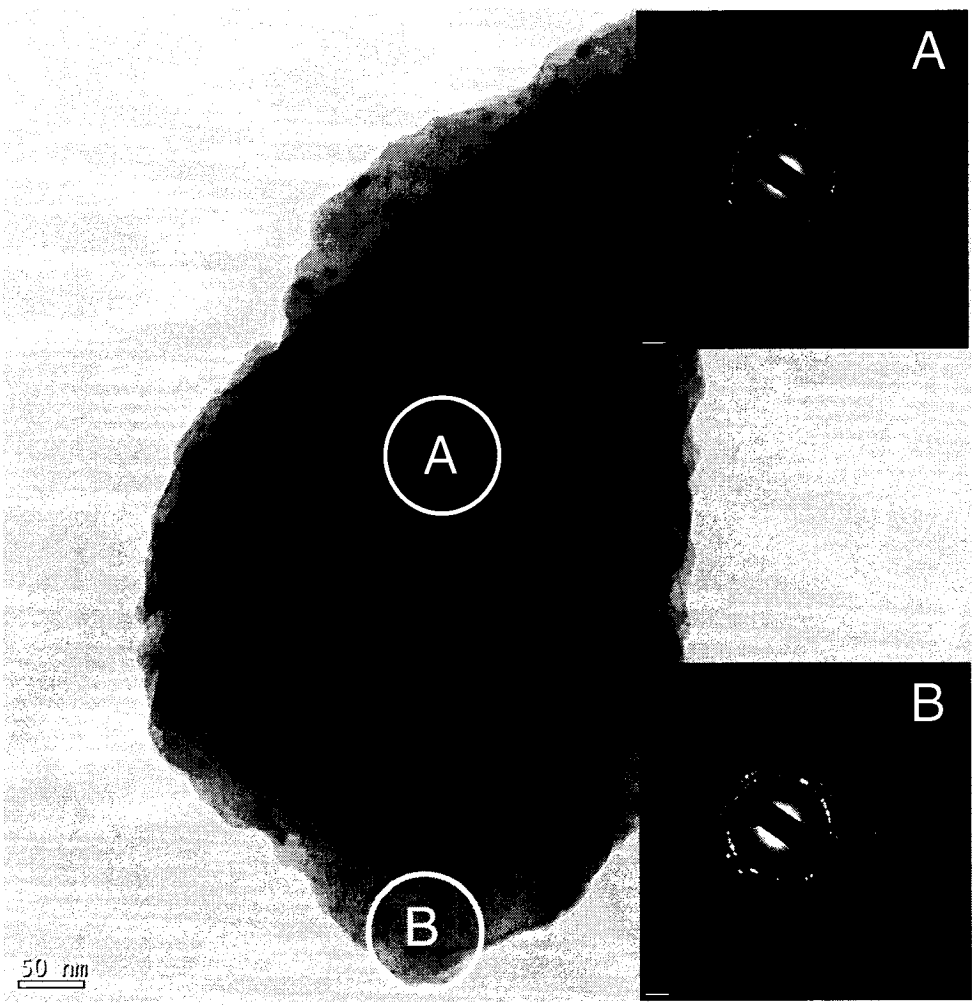

Figure 4.17: TEM BF-image of as-milled binary 40Mg-60 Alloy and SADPs from centre and corner locations showing complete crystallinity.

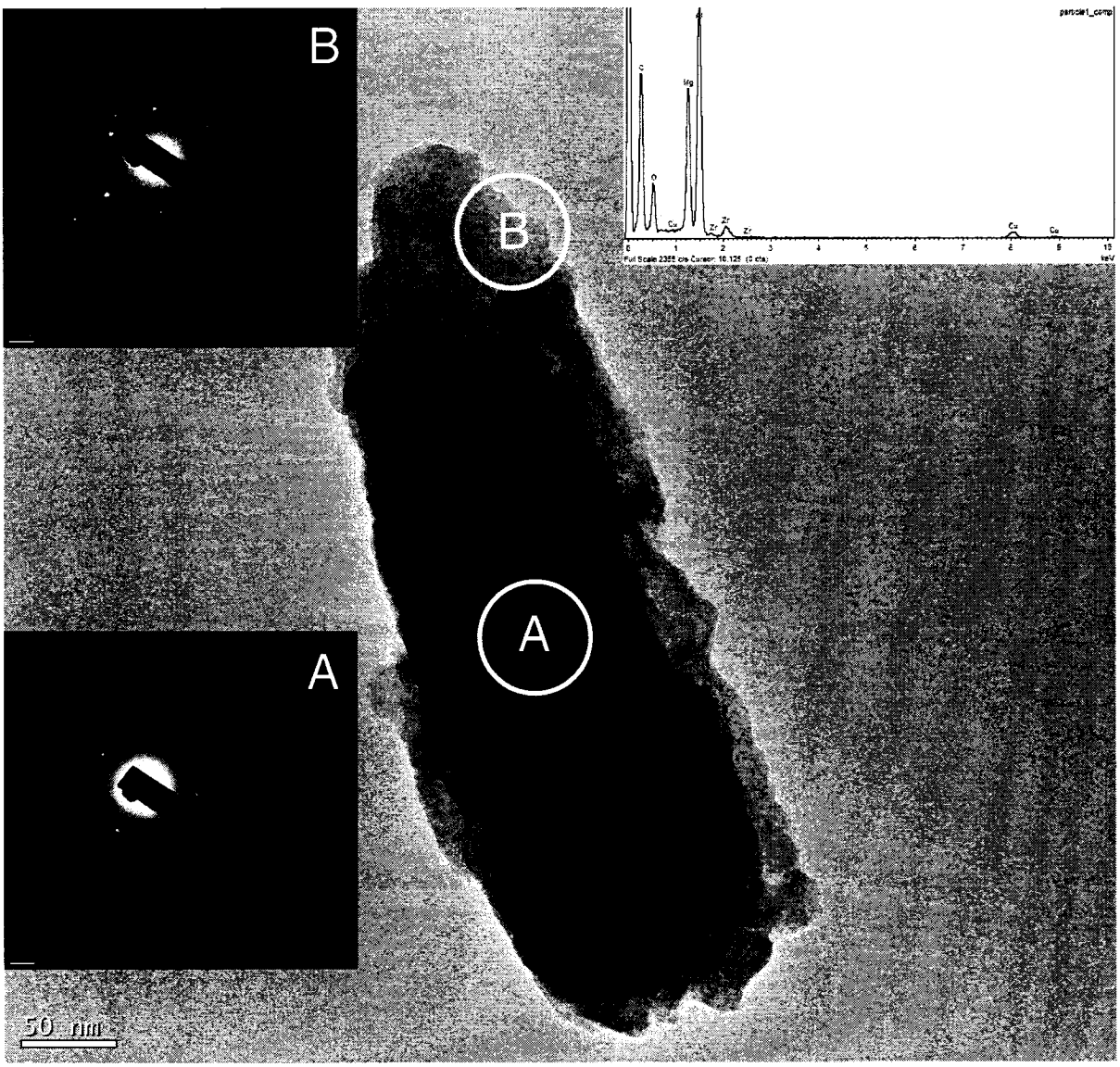

Figure 4.18: TEM image of as-milled 40Mg-55Al-5Zr alloy along with EDS and SADPs taken from center and corner regions. Note: clear diffraction rings are present in both cases.

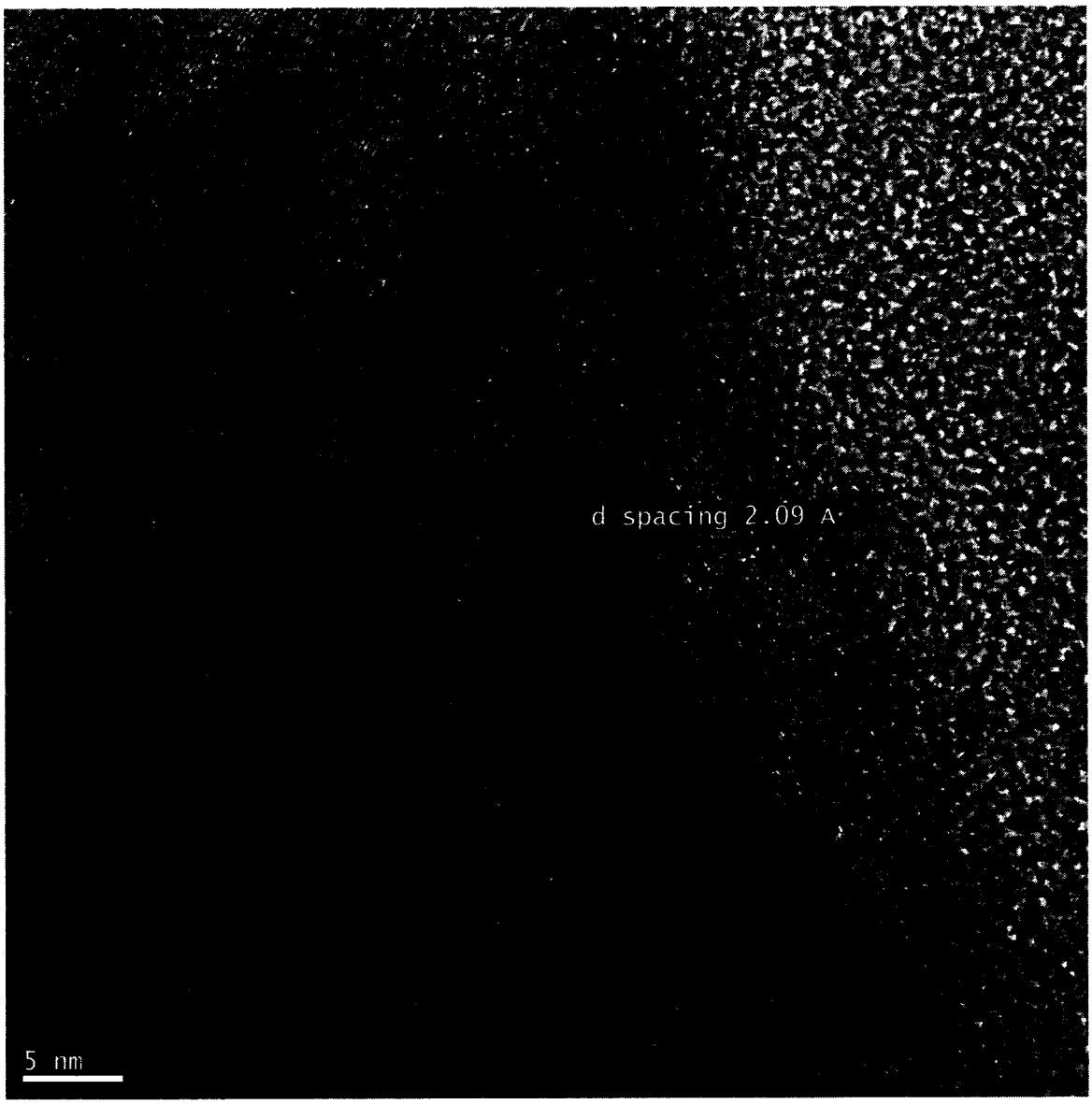

Figure 4.19: High resolution TEM image of as-milled 40Mg-55Al-5Zr showing high degree of crystallinity and interatomic spacing.

For the ternary alloy containing 20 at.%Zr, the TEM image of the selected particle is shown in Figure 4.20. In addition, an EDS spot analysis is taken for the whole particle to verify the overall composition, and the SADPs from both regions "A" and "B" are also presented.

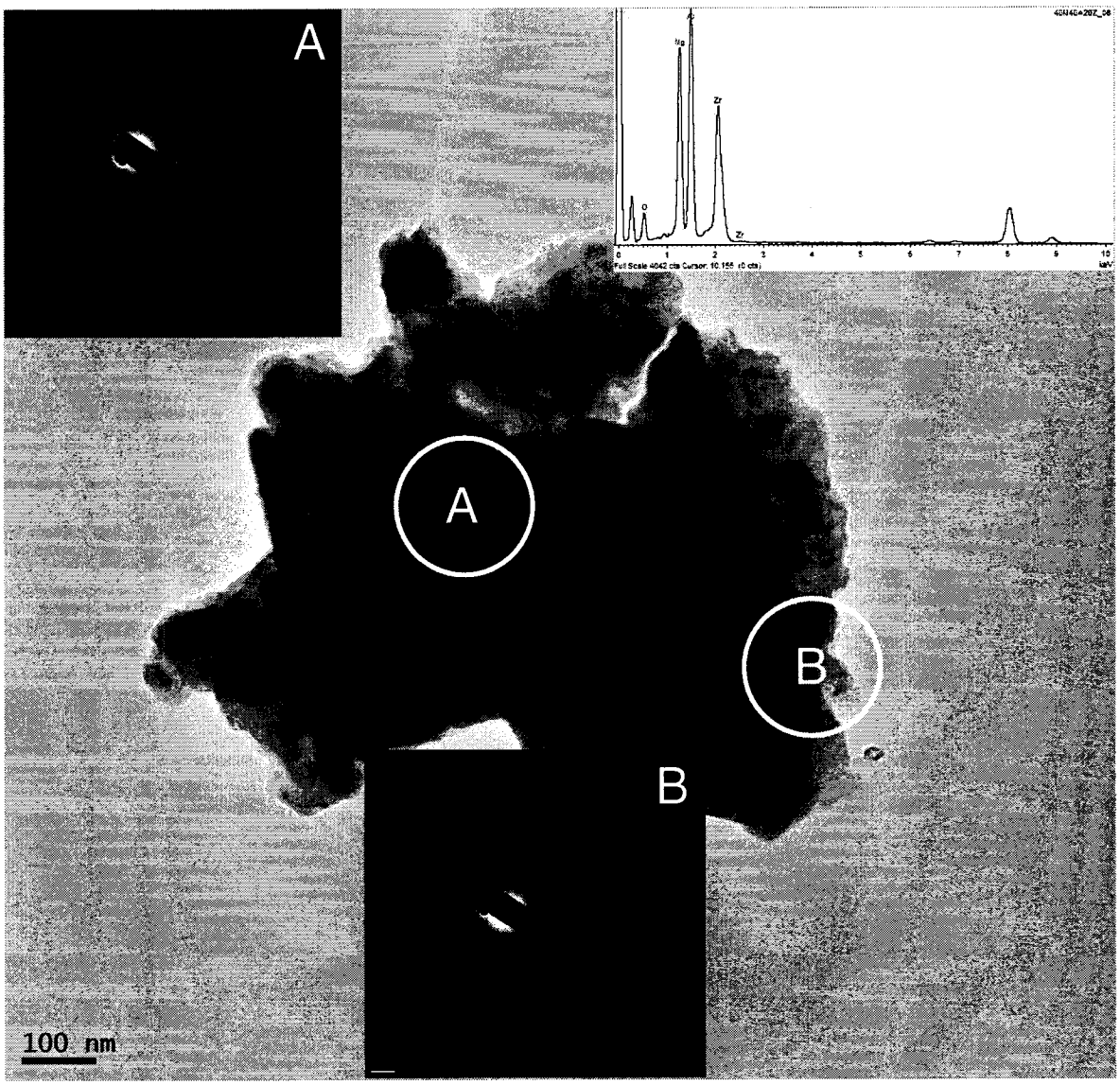

Figure 4.20: TEM image of as-milled 40Mg-40Al-20Zr alloy, along with EDS and SADPs showing the presence of nanocomposite structure at the corner area.

By examining the SADP images, the presence of an amorphous phase was evident, in particular from region "B". Therefore, a nanocomposite structure consisting of an amorphous phase with crystallites interspersed was evidenced by the coexistence of diffraction spots along with halo-like patterns, indicative of crystalline and amorphous

structures. However, it should be mentioned at this point that the SADP image taken from area "A" shows a halo typical of highly amorphous alloys. This should not be mistakenly considered as an indication of a completely/highly amorphous structure and the main reason for such a reflection is due to the larger thickness of the particle in this particular area. This can be explained by the nature of the mechanical alloying process, in which the accumulation of defects will affect the structure of the material, since defects will build-up in thicker parts preventing atomic planes from diffracting.

To reinforce this observation further, a high magnification image shown in Figure 4.21 was taken from the thinner region marked as "B", showing clearly that the borders of the particle are more transparent to the electron beam. Moreover, this might be due to the fact that aperture size is close to 250 nm and confiding such a small area is not possible without obtaining reflections from the amorphous carbon grid. Additionally, a high resolution image presented in Figure 4.22 was taken from the side of the particle in order to verify the presence of a nanocomposite structure. It can be seen by carefully examining this particular image that many randomly oriented crystals exist in addition to regions having a disordered structure, which is typical of amorphous regions. Thus, the nanocomposite structure developed in this system by increasing the Zr concentration to 20 at.%.

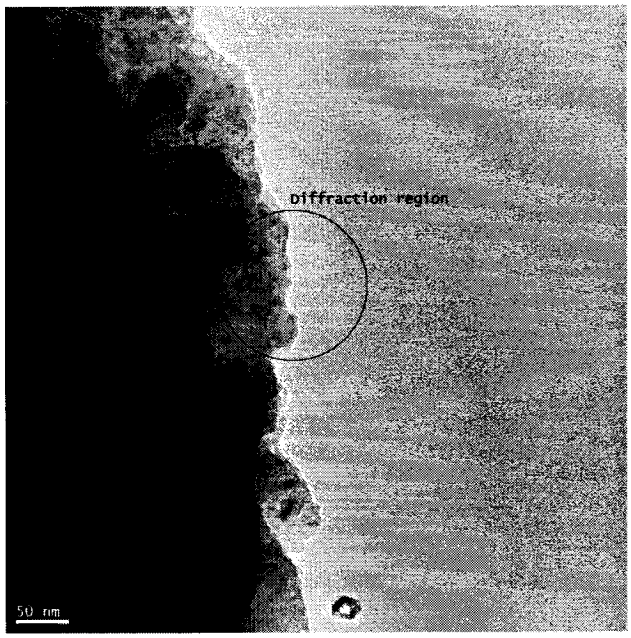

Figure 4.21: High magnification TEM image of region "B" of the nanocomposite structure of as-milled 40Mg-40Al-20Zr alloy.

The TEM image of the alloy containing 35at.% Zr is shown in Figure 4.23 along with the corresponding EDS analysis for the particle and the SADPs taken from regions "A" and "B". It can be observed that a nanocomposite structure was obtained, evidenced by the coexistence of diffraction spots and halo-like diffraction pattern. An additional observation is that the crystallinity spots from SADPs for this particular alloy are more pronounced compared to the alloy containing 20 at.% of Zr. This might be due to the higher oxidation rate that was observed in this alloy from X-ray diffractograms which promotes more crystallization of ZrO_2. However, it could be also due to the tilting of the specimen or even larger thicknesses.

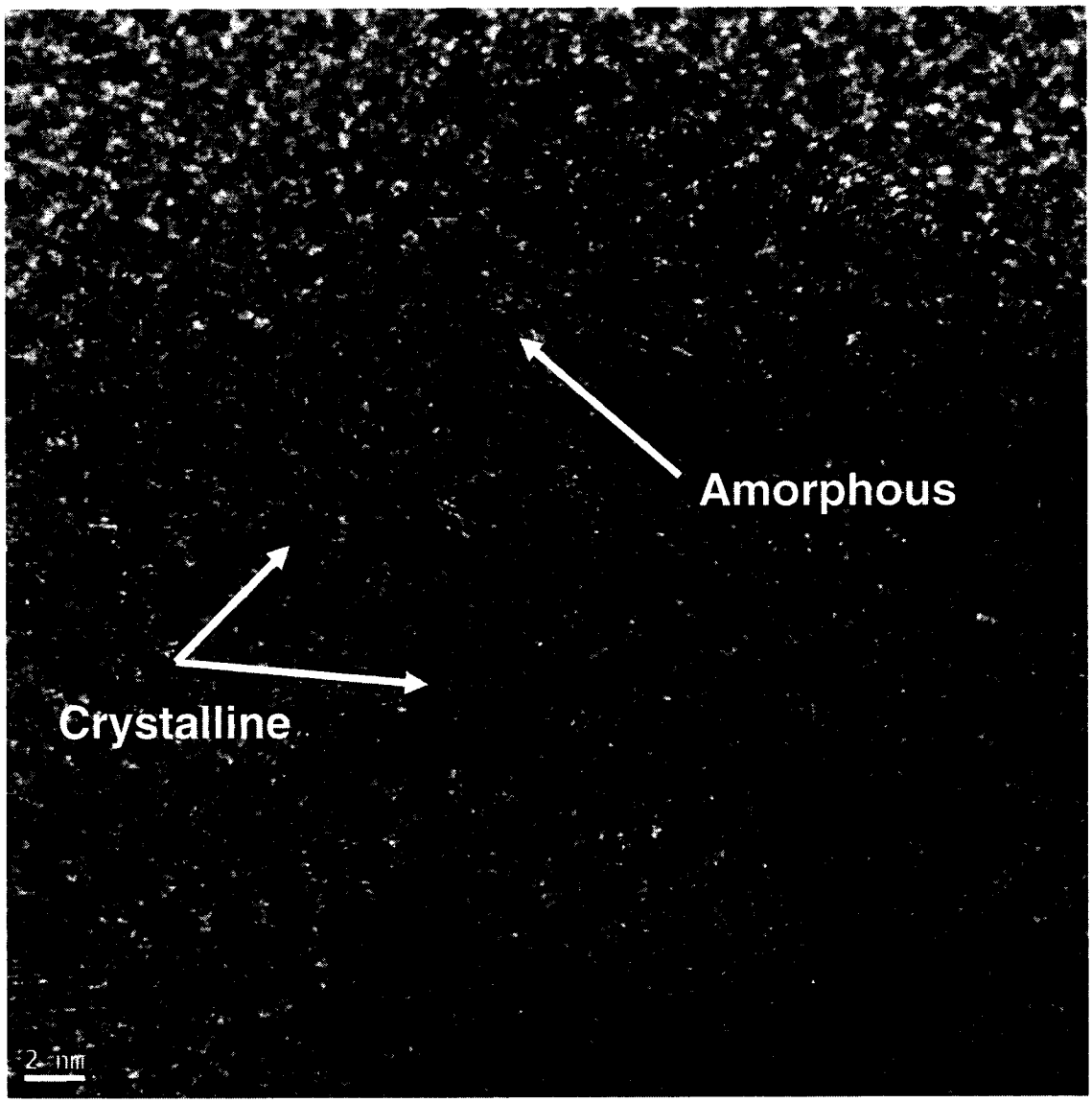

Figure 4.22: High resolution TEM image of the as-milled 40Mg-40Al-20Zr alloy, showing the coexistence of crystallites embedded in an amorphous matrix.

Figure 4.24 shows a compilation of the SADPs for this series of alloys in order to assess the progress of amorphization as a function of Zr content. In general, it can be observed that as the Zr content increases the diffraction rings diminish in intensity and the halo-like diffraction becomes more pronounced. An exception is in the case of

35% in which the possibility of having higher oxidation rates or higher thicknesses and therefore crystalline oxides led to more pronounced reflections of the crystalline phase.

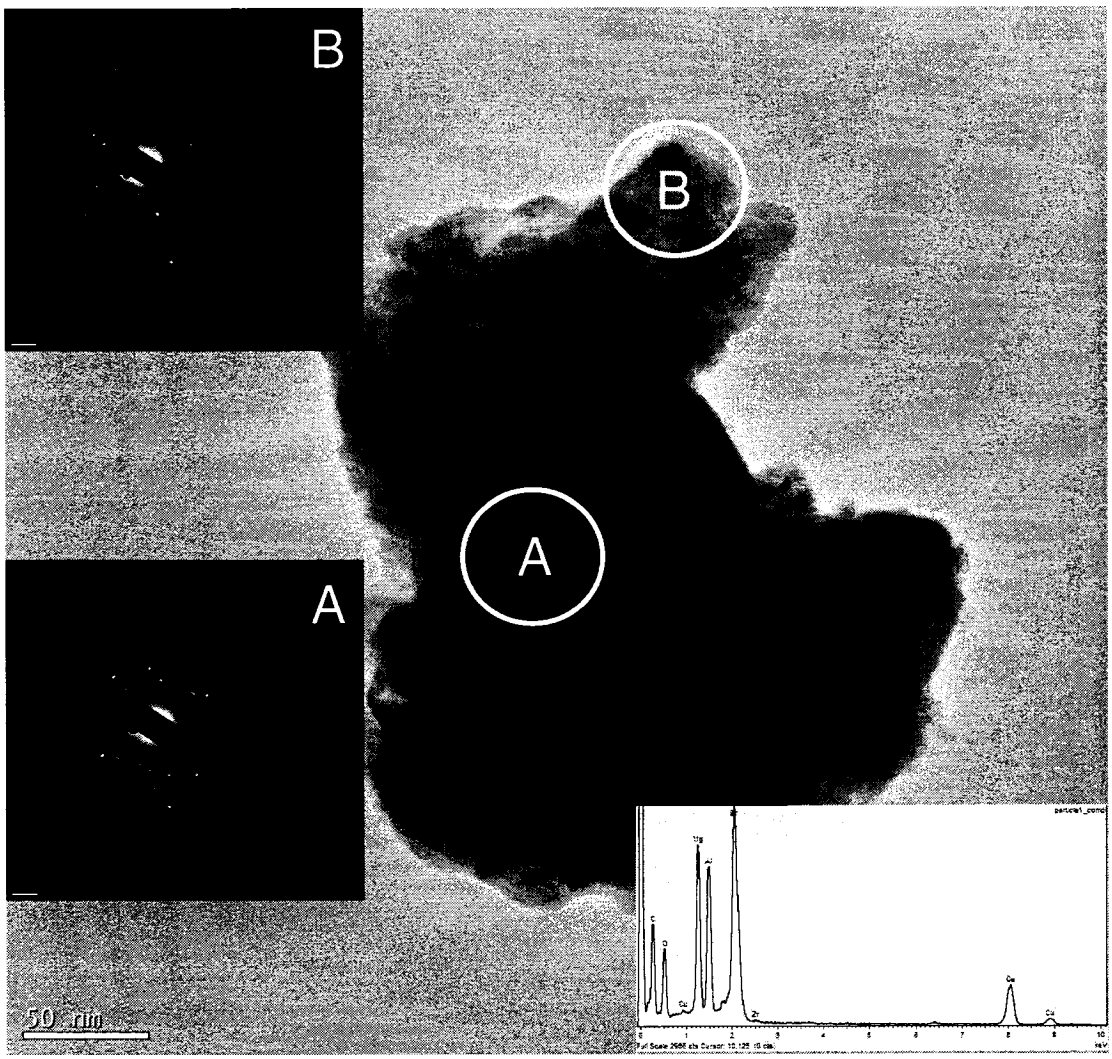

Figure 4.23: TEM image of as-milled 40Mg-25Al-35Zr particle, along with EDS and SADPs of two locations that show the nanocomposite structure.

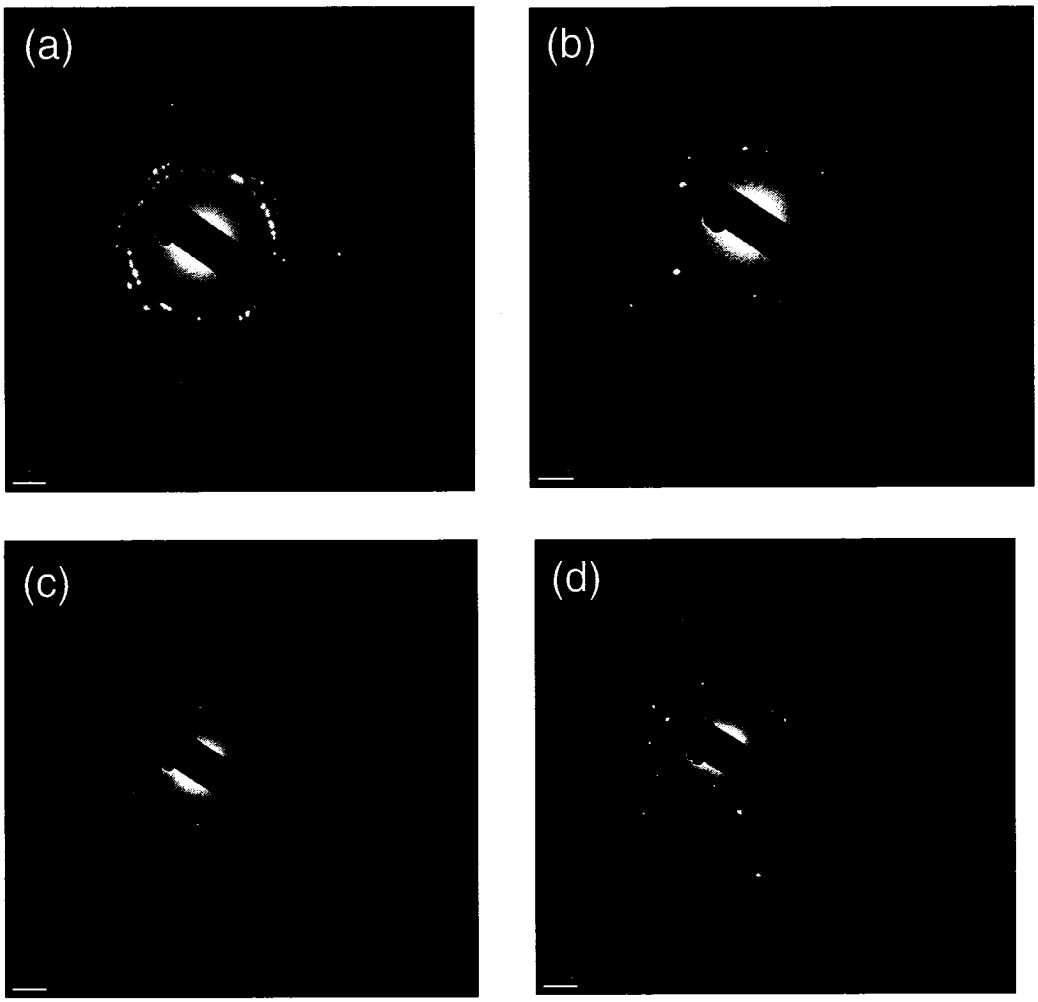

Figure 4.24: SADPs showing the formation of amorphous phase as a function of Zr content: (a) 40Mg-60Al, (b) 40Mg-55Al-5Zr, (c) 40Mg-40Al-20Zr, (d) 40Mg-25Al-35Zr.

4.3.3 Crystallite Size Measurement

in this category of alloys, the determination of crystallite sizes was performed via direct TEM observation using dark- (DF) and bright-field (BF) images only. The results for both as-milled and annealed alloys at different Zr concentrations are shown

in Figure 4.25. It can be seen that the crystallite size decreases as the Zr content increases for both as-milled and annealed powders. Also, there is an apparent stability in the grain structure as the Zr content increases, as observed by the negligible grain growth observed for alloys containing 20 and 35 at.%Zr. In the case of the alloy containing 20at% Zr, the presence of the zirconium tri-aluminide intermetallic (Al_3Zr) is thought to contribute to the stability of the nanocrystalline structure, via Zenner pinning. In general, these two alloys showed a nanocomposite structure and good structural stability when isothermally annealed at 400°C for 1 hour.

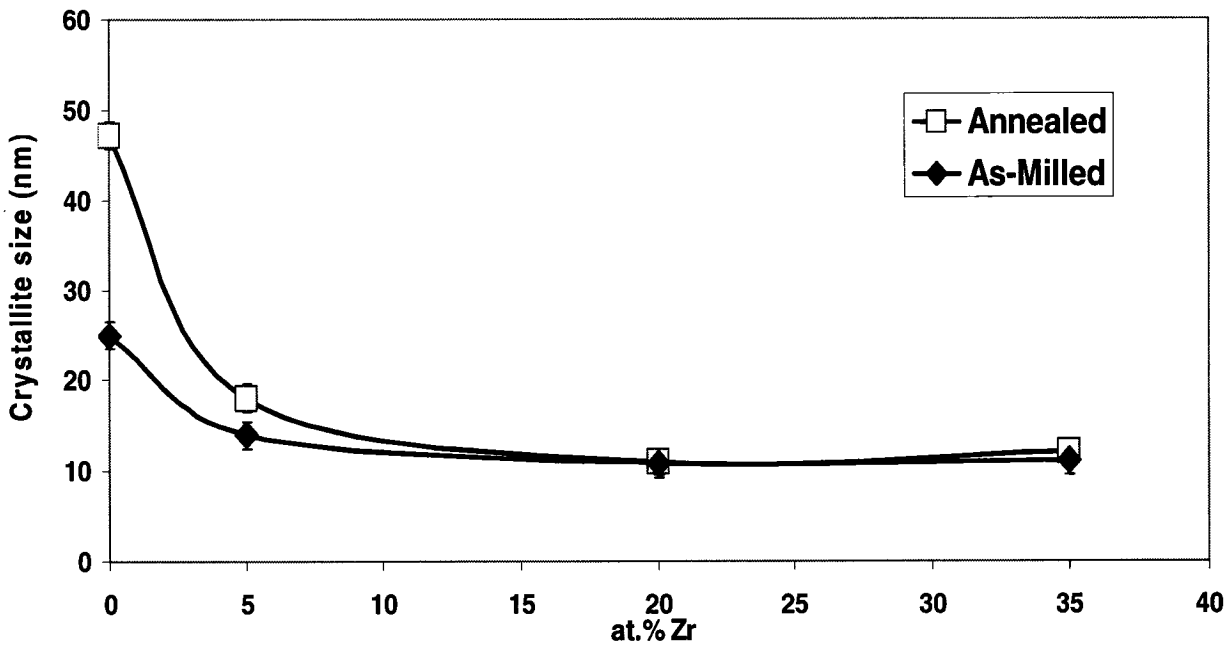

Figure 4.25: Reduction in crystallite size as a function of the Zr concentration.

As stated earlier, the measurements of crystallite sizes were carried out using direct TEM observations. For illustration purposes, dark field images of both as-milled

and annealed powder of the $Mg_{40}Al_{25}Zr_{35}$ alloy are presented in Figure 4.26. The crystallite size was determined based on the average value of several readings.

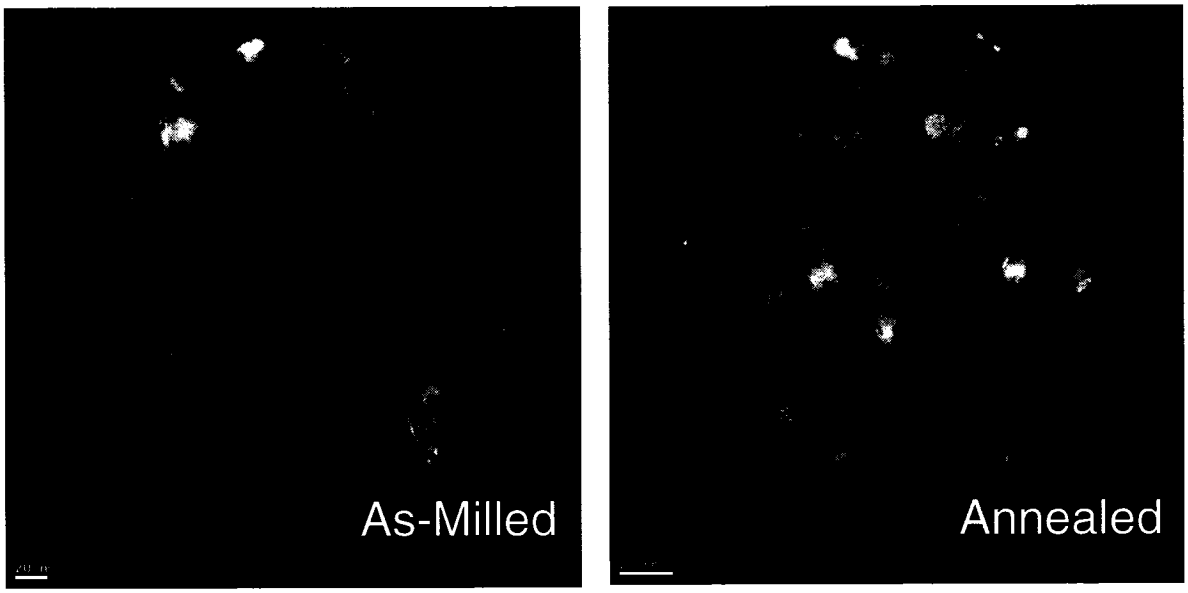

Figure 4.26: Dark field TEM images employed in the determination of crystallite size for the as-milled and annealed 40Mg-25Al-35Zr alloy.

4.3.4 Hardness Measurements

Hardness measurements performed on compacted samples are shown in Figure 4.27. The values show a continuous increase in hardness up to 20 at.%Zr where the values remain almost constant up to 35 at.%Zr. As with low Mg containing alloys this might be related to the observed presence of the zirconium oxide acting as a strengthening agent. However, the improvement in hardness might be also attributed to the formation of the nanocomposite structure and the presence of nanocrystals.

The aforementioned crystallite size measurements and average hardness values suggest that the alloy containing 20 at.%Zr combines both thermal stability and improved mechanical properties. Despite the fact that similar results were obtained for the alloy containing 35at%, it should be kept on mind that lower oxidation levels were detected for the alloy containing 20at% which might be due to the lower Zr concentrations.

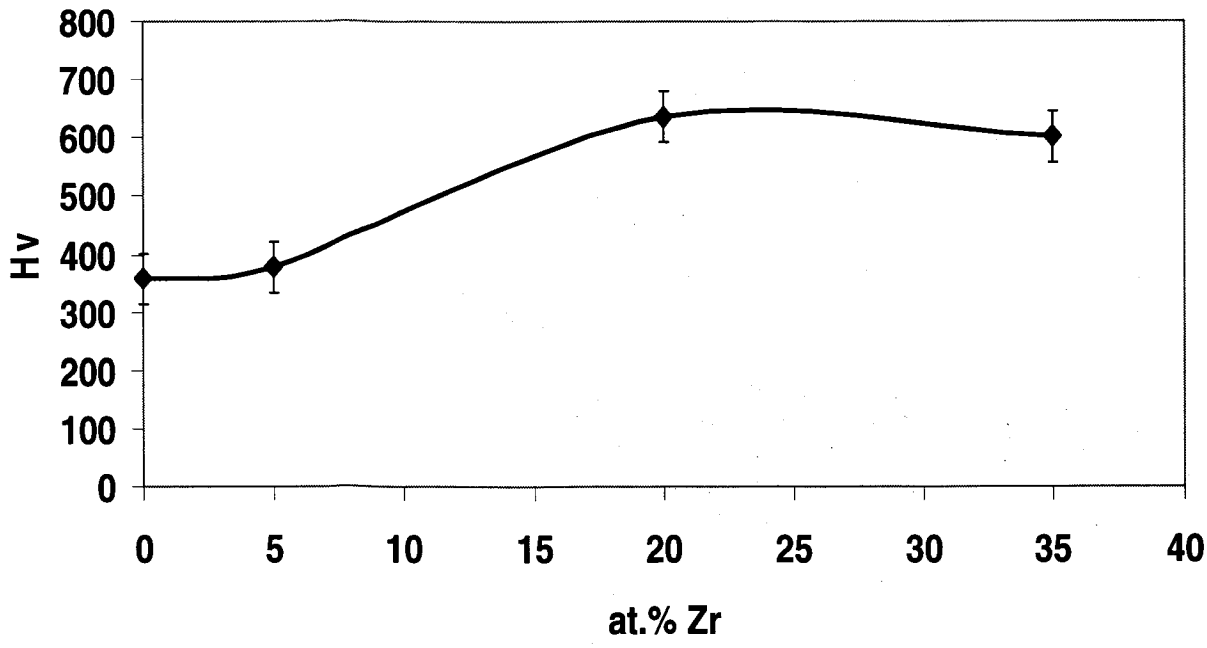

Figure 4.27: Variation of hardness for different Zr concentrations for High Mg-containing Alloys.

4.4 Low Al-Containing Alloys

In this category of alloys, the Al concentration was fixed to 10 at.% as in $Al_{10}Mg_{90-x}Zr_x$ (where x: 0, 5, 20, and 35 at.%) nominal composition which leads to one binary alloy and three ternary alloys.

4.4.1 Phase Evolution Studied by XRD

X-ray diffraction patterns of the resulting as-milled and annealed powder alloys of the *Low-Al* series of alloys are presented in Figures 4.28 and 4.29, respectively

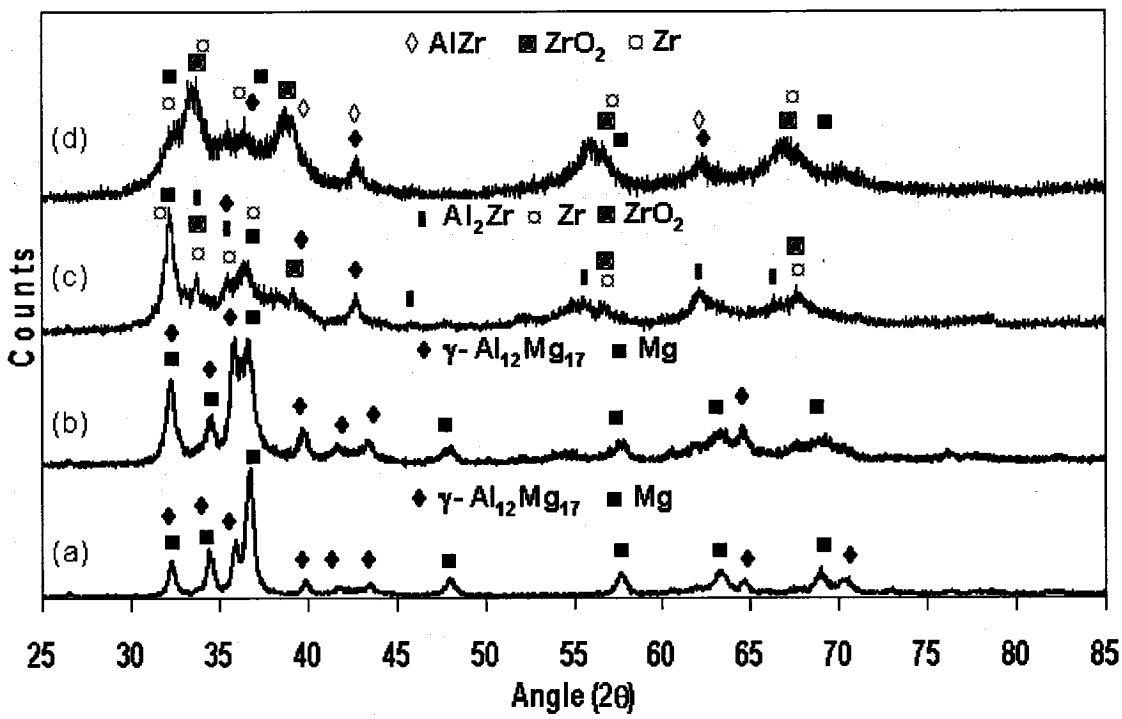

Figure 4.28: X-ray diffraction patterns of the resulting as-milled alloy powders: (a) 10Al-90Mg, (b) 10Al-85Mg-5Zr, (c) 10Al-70Mg-20Zr, (d) 10Al-55Mg-35Zr.

For the binary alloy, the γ-$Al_{12}Mg_{17}$ intermetallic along with unalloyed Mg were formed after milling. These two phases remained stable after annealing accompanied by peak narrowing indicating grain growth and stress relaxation. For this composition the phase evolution is in agreement, in terms of the presence of unalloyed Mg, with the predictions of the equilibrium Al-Mg phase diagram. Nevertheless, the formation of the γ-phase intermetallic seems to be promoted by the presence of even a small amount of Al. The γ-$Al_{12}Mg_{17}$ phase showed good thermal stability despite the fact that it is not the equilibrium phase at this particular composition.

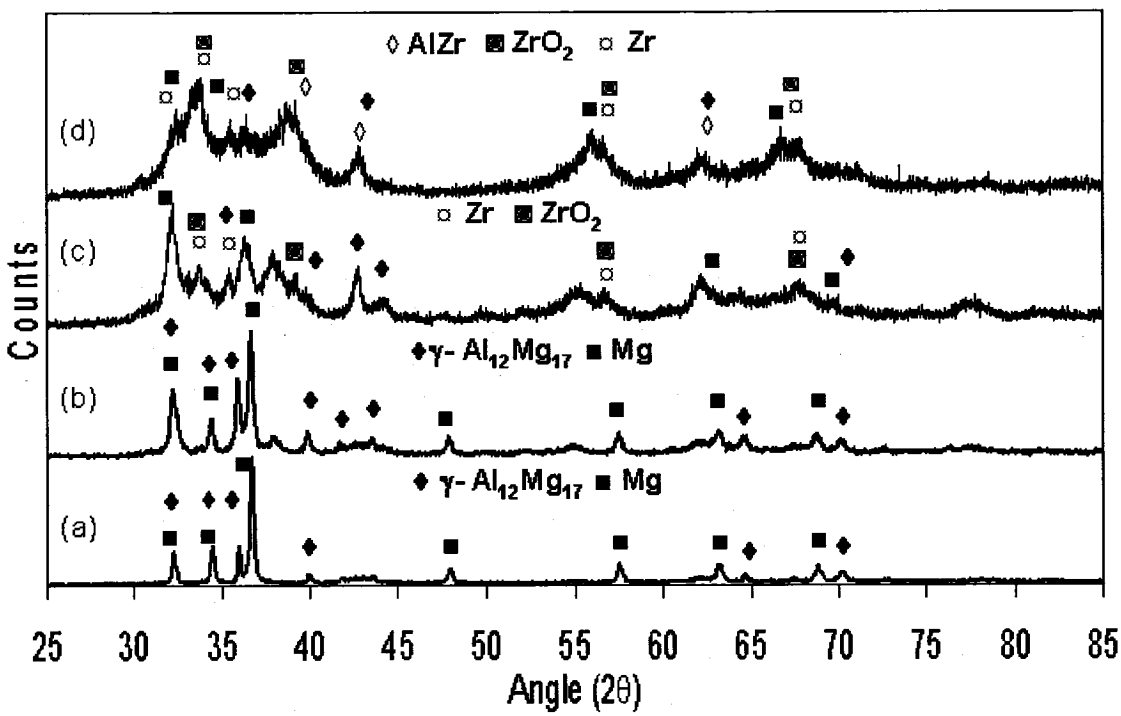

Figure 4.29: X-ray diffraction patterns of the resulting annealed alloy powders: (a) 10A-90Mg, (b) 10Al-85Mg-5Zr, (c) 10Al-70Mg-20Zr, (d) 10Al-55Mg-35Zr.

When 5at%Zr was added to the alloy, the phase constitution did not change (γ-$Al_{12}Mg_{17}$+unalloyed Mg) relative to the binary alloy. The only additional observation was that the amount of γ-$Al_{12}Mg_{17}$ increased. Upon annealing at 400°C, the present phases remained unchanged, indicating thermal stability. The only noticeable change, as in the binary alloy, was the slightly narrower diffraction peaks due to crystallite coarsening. Another feature was the apparent shift of peaks toward even lower angles and the observed broadening. This indicates that the addition of Zr caused additional structural refinement and substantial disruption as the peaks broadened compared to the binary alloy.

On the other hand, the amount of Zr present at this alloy was not detected from XRD which might be due to limited detectability of the XRD, suggesting the use of other complementary techniques to verify its presence. Figure 4.30 shows a secondary electron (SE-SEM) image of an $Al_{10}Mg_{85}Zr_5$ particle. Upon switching to the back-scattered mode Figure 4.31, it is observed that most of Zr appeared in the form of cores which is in good agreement with the results reported elsewhere [53] for cast alloys. This mainly relates to the low solid solubility of Zr in Mg which remains in the form of Zr-rich cores.

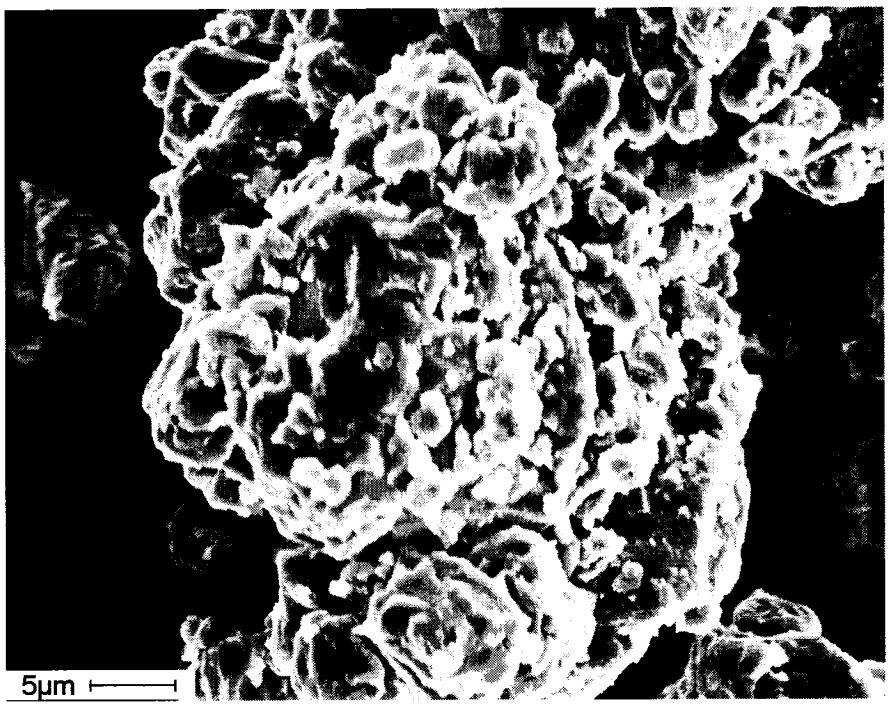

Figure 4.30: Secondary electron image of the binary 10Al-90Mg alloy.

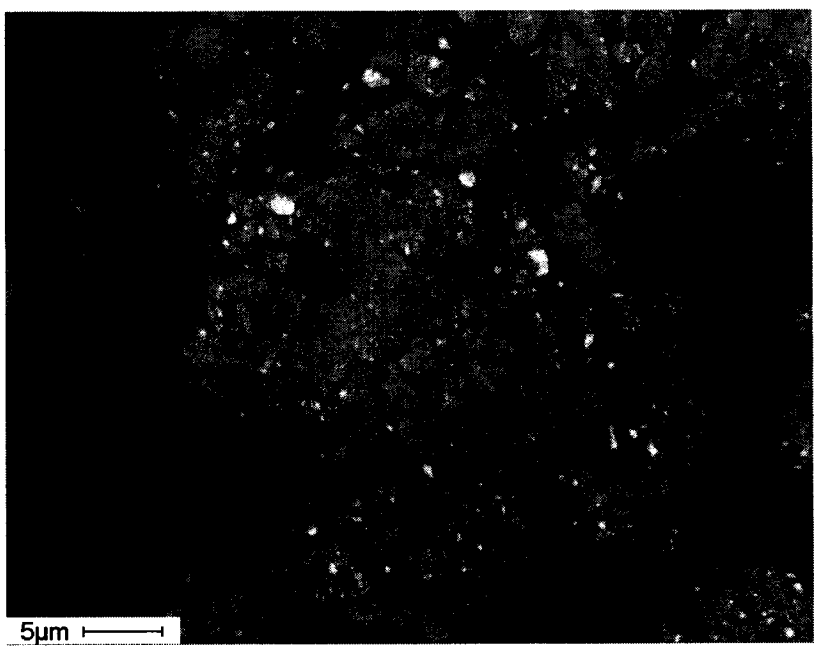

Figure 4.31: Back scattered electron image of the binary 10Al-90Mg alloy, showing residual amounts of Zr in the form of Zr-rich cores.

Furthermore, upon increasing the Zr concentration to 20at%, the XRD plot of the as-milled alloys revealed primarily the presence of some unalloyed Mg and Zr, along with, ZrO_2, and small amounts of γ-$Al_{12}Mg_{17}$ and Al_2Zr intermetallic. This might be due to the presence of low Al concentrations in this alloy which impede the formation of additional Al-Zr intermetallic phases leading to larger amounts of unalloyed Zr. In addition, the formation of Al_2Zr intermetallic instead of Al_3Zr was observed which is, as mentioned earlier, a more stable phase; however, decomposing upon annealing.

For the alloy containing 35at%Zr, the X-ray diffractogram of the as-milled alloy showed the presence of both unalloyed Mg and Zr. This is in addition to the formation of γ-$Al_{12}Mg_{17}$, AlZr intermetallic and ZrO_2. The formation of these phases shows clearly the obtained deviation from equilibrium under mechanical milling. However, no phase transformations were observed by XRD upon annealing, highlighting the high stability of these phases.

4.4.2 TEM Studies

For this category of alloys, Figure 4.32 shows a TEM image of the binary alloy of nominal composition of 10Al-90Mg, along with the selected area diffraction pattern (SADP) taken from the center of a particle.

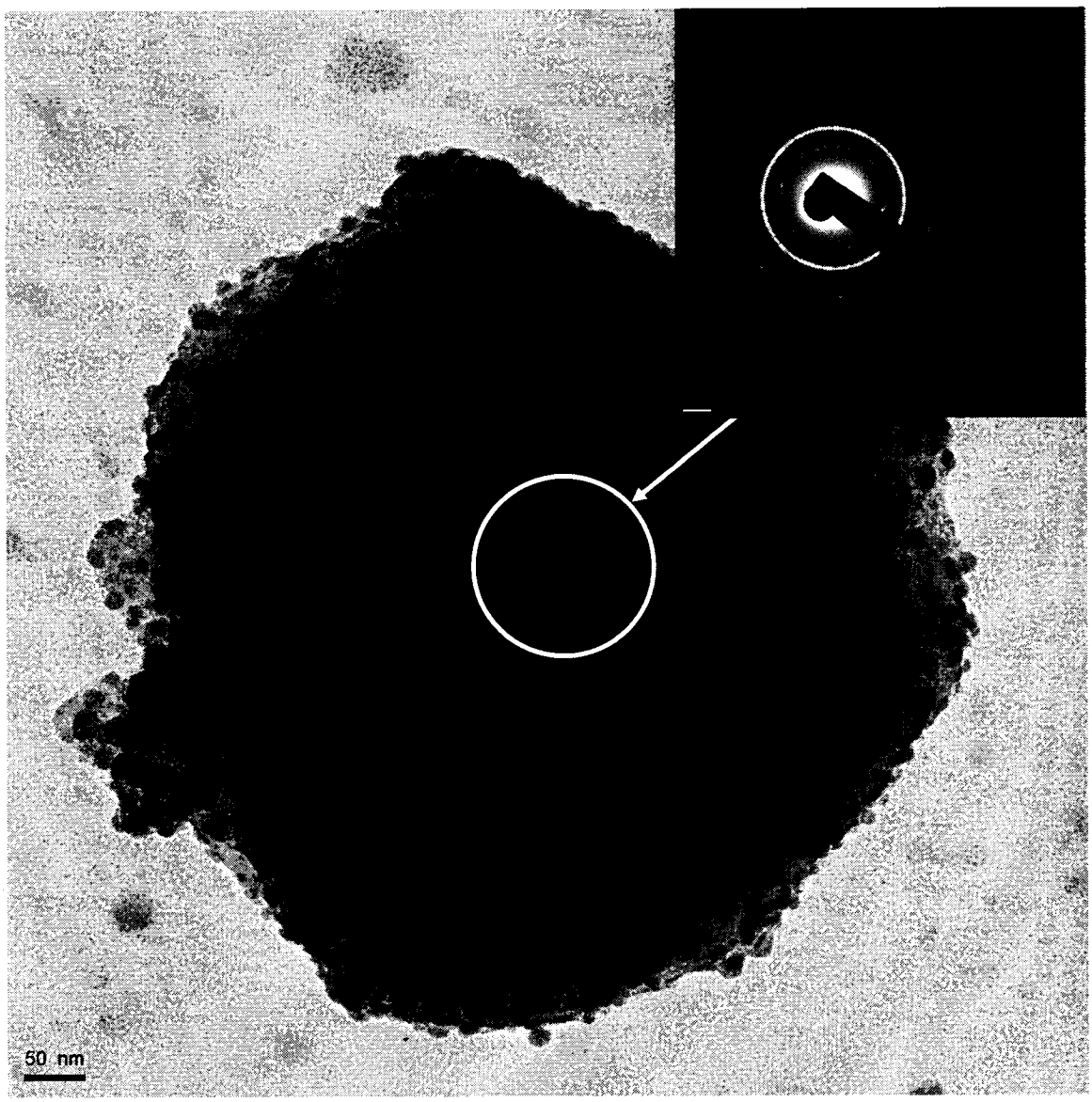

Figure 4.32: TEM image of as-milled binary 10Al-90Mg alloy, showing complete crystallinity.

As observed, the high degree of crystallinity is notorious with no apparent indication of an amorphous phase as evidenced by the presence of sharp diffraction rings. This observation is in agreement with the XRD results in which no indication of amorphization was detected.

For the alloy containing 5at%Zr, a BF-TEM image of a typical particle under study is shown in Figure 4.33.

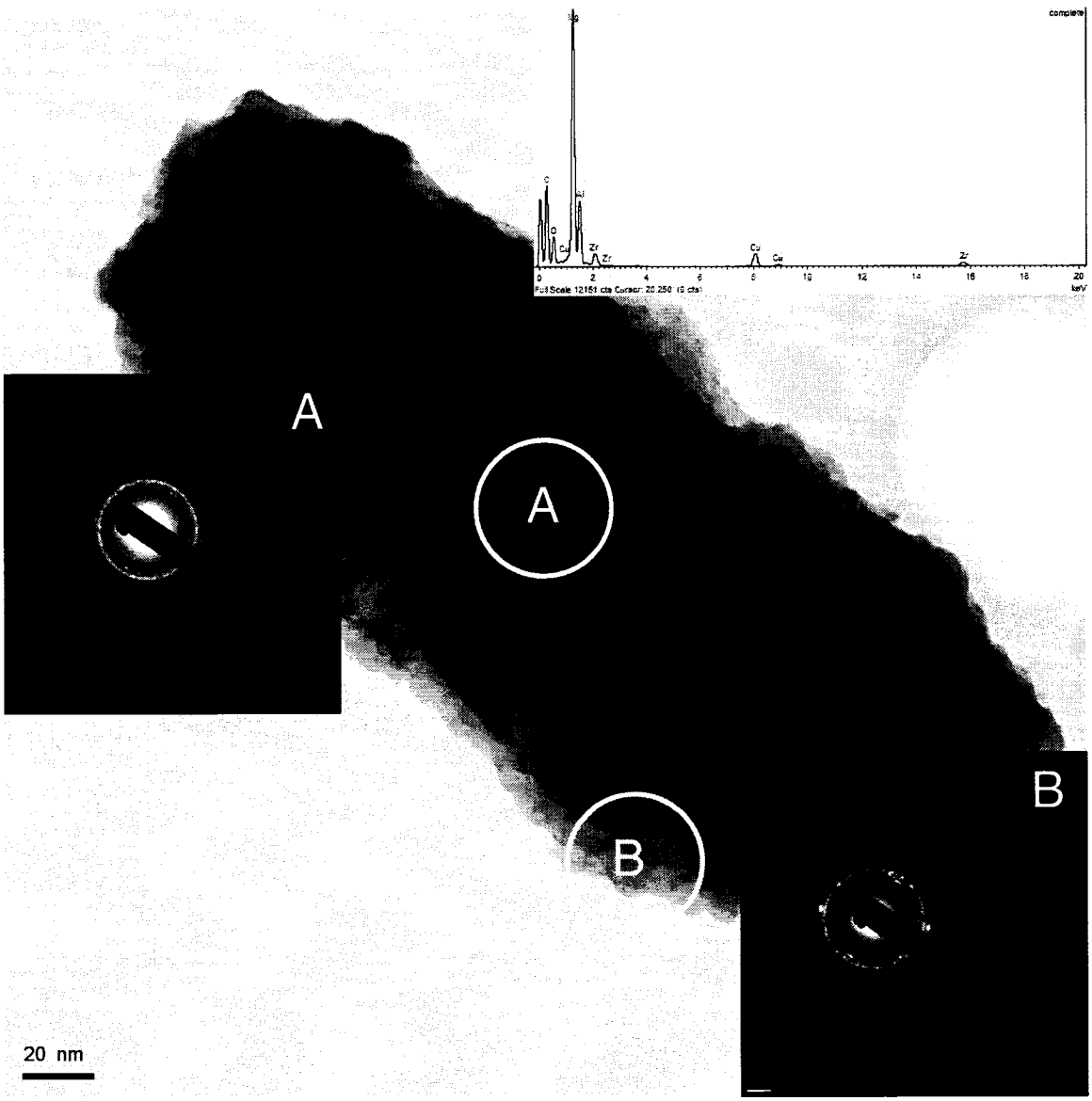

Figure 4.33: TEM image of as-milled 10Al-85Mg-5Zr alloy, along with EDS and SADP of two areas.

The EDS analysis of this particular alloy, taken from the centre of the particle, reveals once again that no compositional changes were obtained as compared with the

nominal composition. The corresponding selected area diffraction patterns (SADPs) of the alloy containing 5 at.% Zr, taken also from the center and corner of this particle (circled areas) are presented as well. The continuous rings reveal the presence of a highly crystalline material and the existence of any amorphous phase cannot be inferred from this DP. Therefore, the Al-Mg binary alloy and the alloy containing 5 at.%Zr showed no apparent presence of either a nanocomposite structure or an amorphous phase.

Further consideration was given to the previously selected particle regarding the presence of the black region located at the top as observed in Figure 4.34. The EDS analysis of this region revealed a high Zr concentration, suspected to be the Zr-rich cores shown previously from the SEM images Figure 4.31. The presence of such regions, however, did not promote the formation of an amorphous phase in this alloy evidenced by the sharp diffraction rings of the DP.

A TEM image of a typical particle with 20 at.%Zr is shown in Figure 4.35; in addition, the EDS analysis, taken for the entire particle and showing no compositional fluctuation from the starting material, is also presented. Selected area diffraction patterns taken from the centre and corner regions of the particle are shown in the same figure. However, the diffraction pattern taken from region "A" does not seem to reveal the presence of either a completely crystalline phase or the existence of halo-diffraction typical of amorphous phases; related perhaps to the higher thickness.

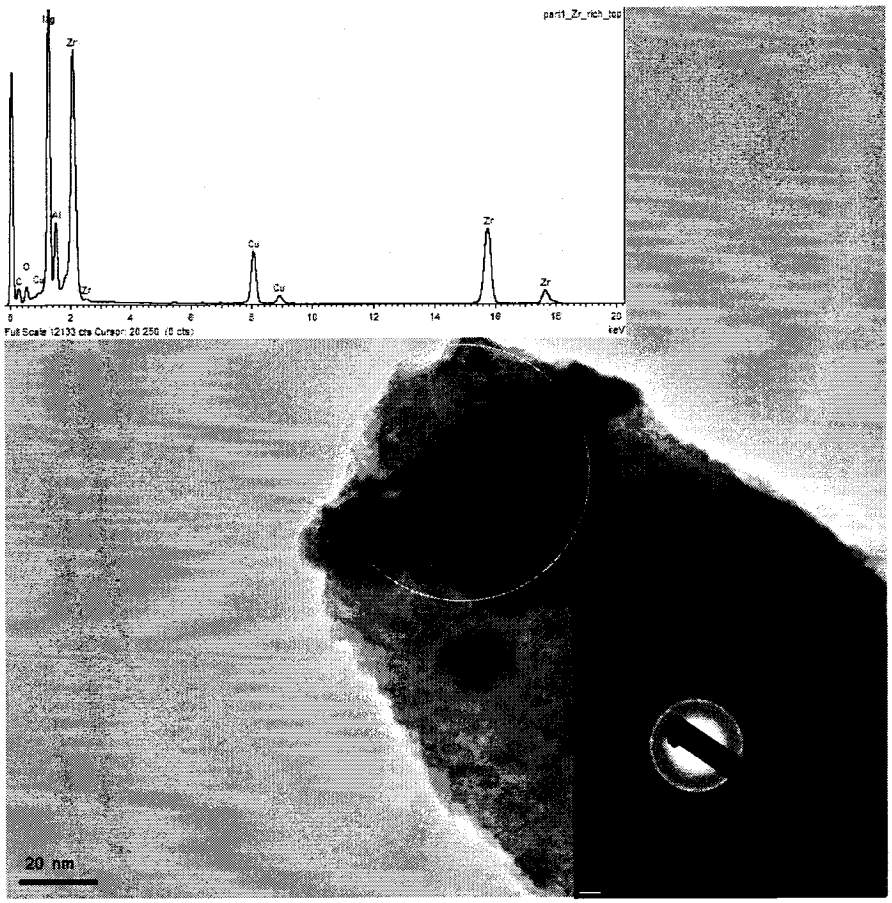

Figure 4.34: SADP and EDS of a dark (circled) region in as-milled 10Al-85Mg-5Zr alloy, showing nanocrystals with high-Zr content.

By considering the DP taken from the corner of the particle in Figure 4.33 (labelled B), it can be seen that well-defined diffraction rings were formed. Moreover, some indication of the presence of a region showing a weak-halo-diffraction pattern exists supporting the presence of a nanocomposite structure. In order to obtain further evidence of the amorphous phase, HR-TEM was used in an attempt to directly observe the nanocomposite structure.

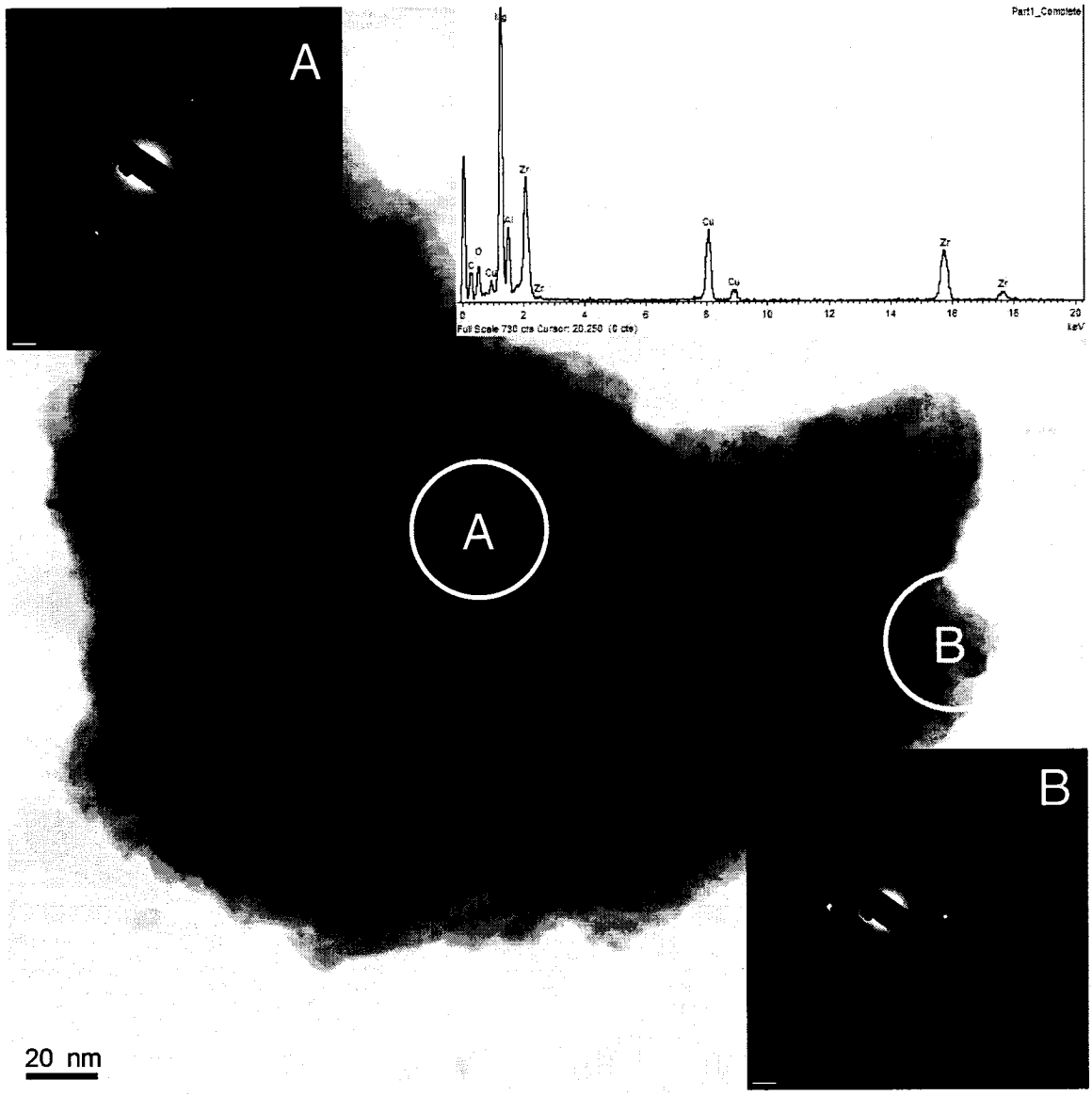

Figure 4.35: TEM of as-milled 10Al-70Mg-20Zr alloy, showing the presence of amorphous materials.

The high resolution image taken from the corner of the particle is presented in Figure 4.36, showing the presence of regions having crystalline ordered structure along with low range order regions, indicative of an amorphous phase. However, by

considering several particles from the same composition, it should be stated here that the amorphous phase is present in residual amounts which seems to be the reason for the absence of a pronounced halo-diffraction DP compared to other series of alloys.

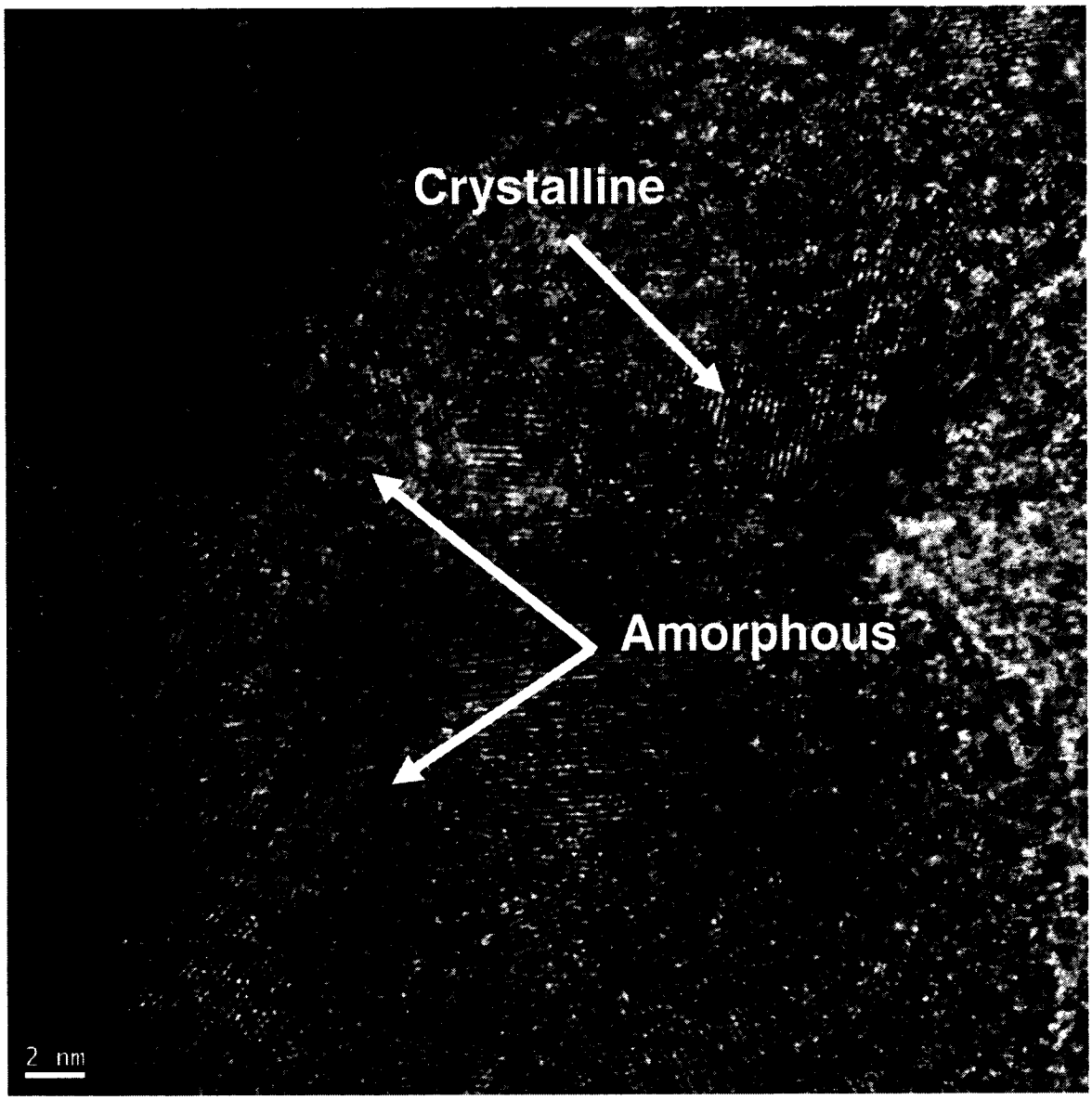

Figure 4.36: HR-TEM of region B in Figure 4.35 the corner position of the as-milled 10Al-70Mg-20Zr powder alloy. Note the presence of both crystalline ordered structure and amorphous regions.

The TEM image along with the EDS analysis and SADP for the alloy containing 35at%Zr are shown in Figure 4.37. It can be seen for the EDS analysis that no significant compositional fluctuation in this particle exists compared to the starting composition of this alloy.

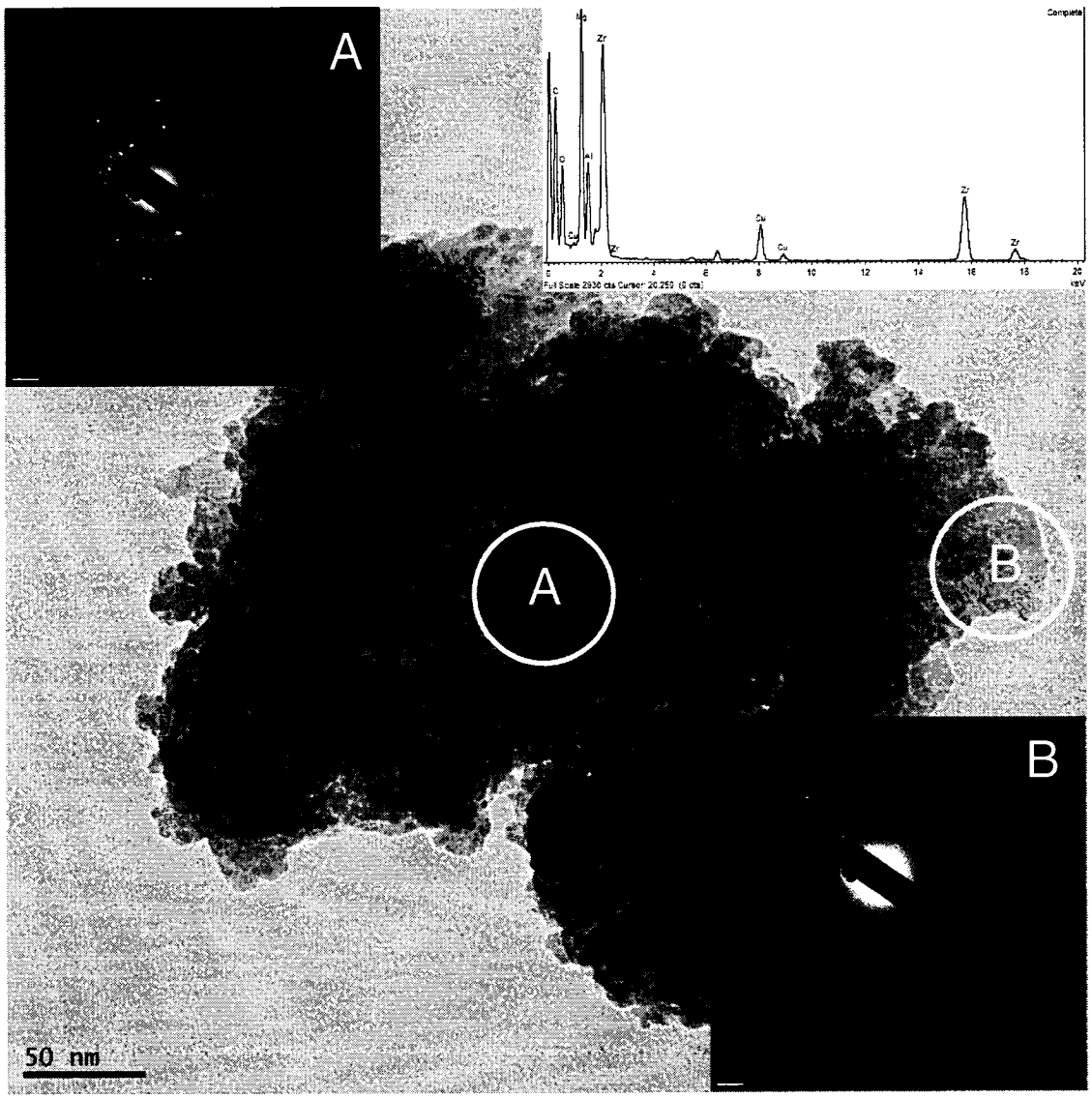

Figure 4.37: BF-TEM image, SADPs and EDS of as-milled 10Al-55Mg-35Zr alloy, showing different crystallinity levels in different locations.

Moreover, the SADP taken from area "A" shows clear presence of crystalline regions as observed from the diffraction rings and no convincing evidence of the presence of an amorphous phase. However, the SADP taken from the corner of the particle marked as region "B" shows a halo-diffraction corresponding to an amorphous region. This might be due to the possible reflection from the amorphous carbon grid. However, a low degree of crystallinity is apparent from this region.

Thus, high resolution TEM was carried out to facilitate direct observation of the possible formation of a nanocomposite structure comprising an amorphous phase. The HR image taken from area "B" of the previously selected particle is shown in Figure 4.38. By carefully examining the HR image it can be seen that the nanocomposite structure is clearly present. This proves that the nanocomposite structure existed in this alloy; however, with small volume fractions of amorphous phase. This might be the main reason for the absence of such observation from the SADP of region "A".

Figure 4.39 shows a series of diffraction patterns highlighting the progress of amorphization as the Zr content increases. However, it should be stated that for the alloy containing 20at%Zr, the presence of an amorphous phase was more pronounced compared to the one containing 35%Zr. In general, for this series of alloys the amount of amorphous phase was lower than alloys from other series, which might be related to the lower Al concentration (10 at.%).

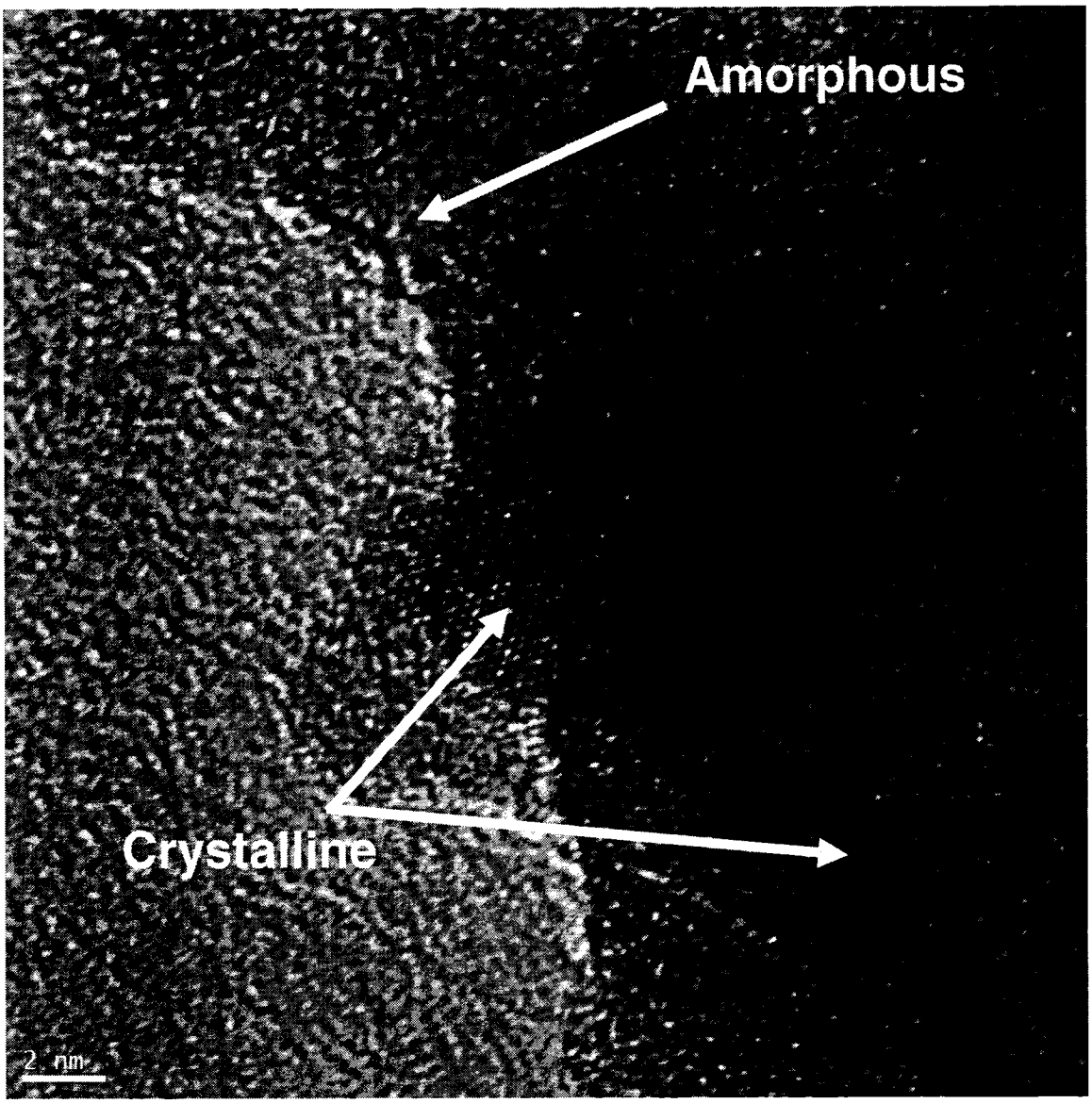

Figure 4.38: HR-TEM image of the as-milled 10Al-55Mg-35Zr alloy, showing the coexistence of both crystalline and amorphous regions.

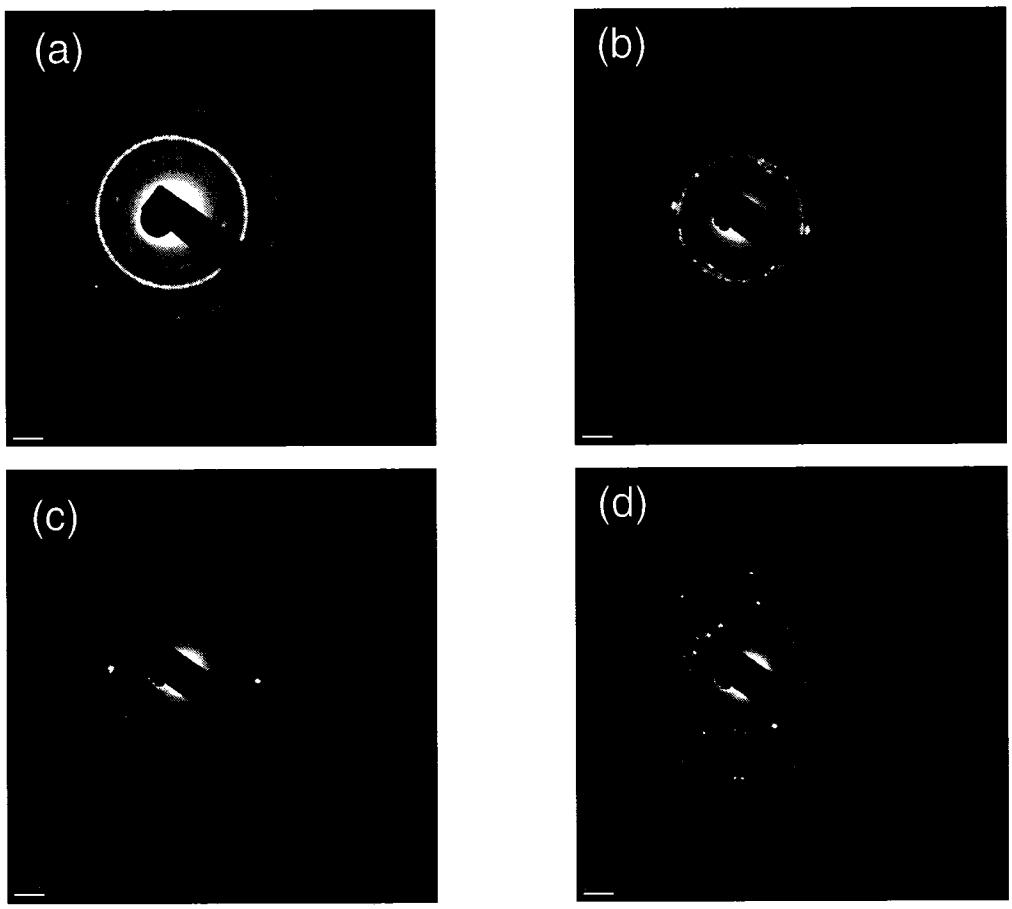

Figure 4.39: Progress of amorphization as a function of Zr content: (a) 10Al-90Mg, (b) 10Al-85Mg-5Zr, (c) 10Al-70Mg-20Zr, (d) 10Al-55Mg-35Zr.

4.4.3 Crystallite Size Measurements

In this category of alloys, the measurement of crystallite size was performed via direct TEM observation using Dark field (DF) images only. The results for both as-milled and annealed alloys at different Zr concentrations are shown in Figure 4.40. For as-milled, the crystallite size decreases by almost half the value upon the addition of 5at%Zr and then increases slightly at 35at% Zr. It should be stated that these are

average values, and that the small changes in crystallite size values for 5 and 20 at.%Zr are not considerable.

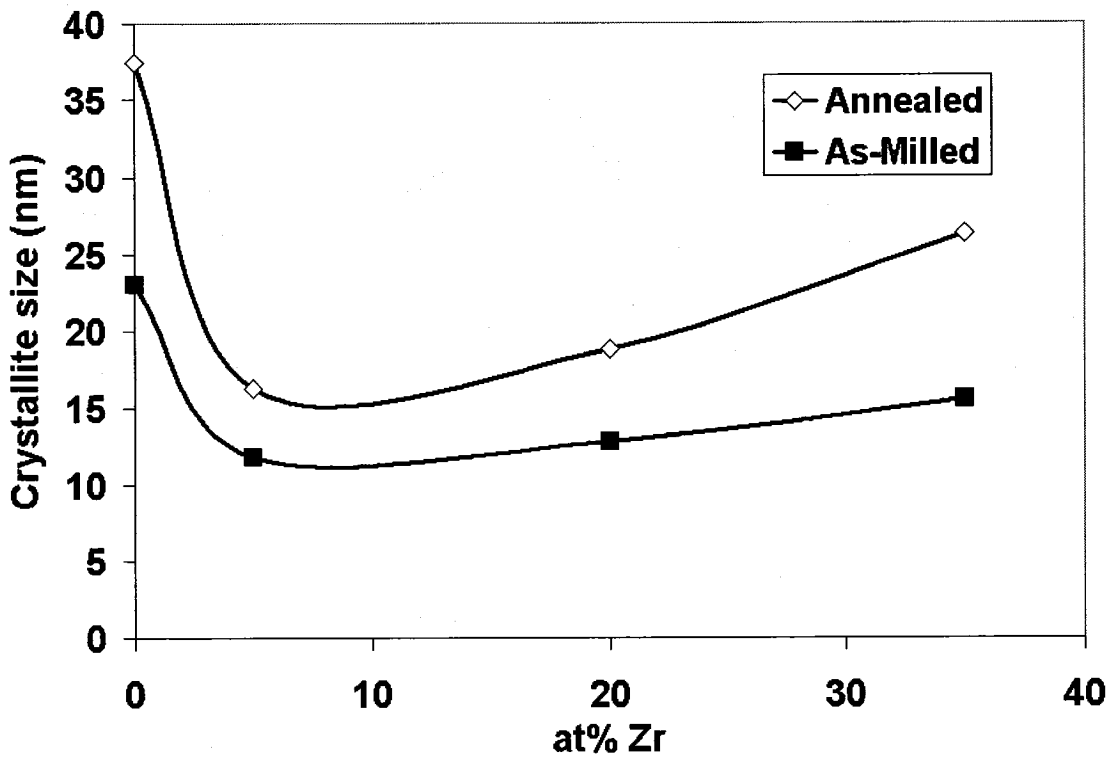

Figure 4.40: Variation in crystallite size at different Zr concentrations.

The role of Zr can be examined more carefully by examining the crystallite size measurement of the annealed alloys. In contrast to the previous series of alloys in this research, the addition of Zr did not prevent grain coarsening after the heat-treatment. The rate of grain growth was different for each alloy series being more pronounced in the binary alloy and the alloy containing 35at%Zr. Surprisingly, the alloy containing 5at%Zr shows better thermal stability compared to other alloys. Therefore, it can be stated that for alloys containing low Al concentrations thermal stability cannot be

improved by increasing the Zr content. This might be due to the absence of Al-Zr intermetallics that contribute to thermal stability, especially zirconium tri-aluminide, Al_3Zr which seems to play a significant role in retarding grain growth. Additionally, despite the fact that both alloys containing 20 and 35at%Zr showed nanocomposite structures, the formation of such structure did not contribute considerably to the thermal stability of the nanocrystals, which might be due to the lack of Al_3Zr formation. Thus, it might be stated here that the obtained thermal stability in the nanocomposite structure is subject to the formation of larger fractions of the amorphous phase and/or the Al_3Zr intermetallic, which proved to be an important factor in controlling grain growth.

Two bright field images of the $Al_{10}Mg_{55}Zr_{35}$ in both as-milled and annealed conditions are shown in Figure 4.41, the crystallite size was determined based on the average values.

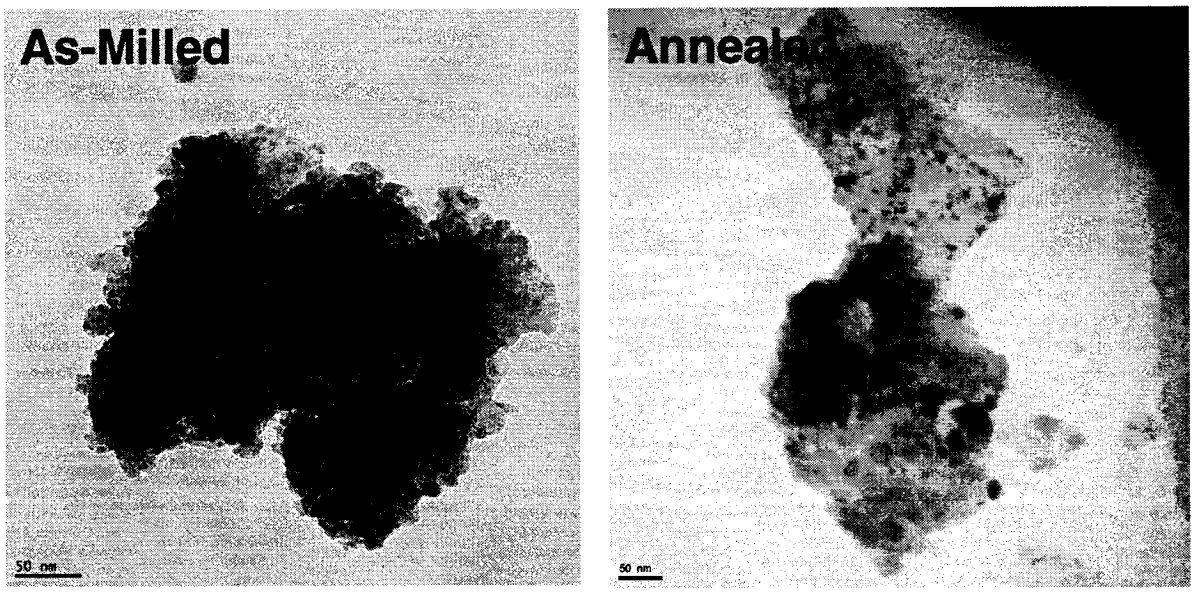

Figure 4.41: TEM bright field images for crystallite size measurement for as-milled and annealed 10Al-55Mg-35Zr alloy, provided for comparative purposes.

4.3.4 Hardness measurements

The hardness measurements of the resulting alloys were taken from compacts in order to evaluate the effect of Zr addition. Figure 4.42 shows a slight improvement in hardness by adding Zr to the binary alloy, which increased slightly upon increasing Zr concentration to 20at%. One interesting observation is that despite the presence of ZrO_2 in the alloy containing 20at%Zr, the hardness value was close to that for the 5at%Zr alloy which has no ZrO_2. This might be considered as an indication of the lower fraction of oxides present into this alloy compared to the alloy containing 35at%Zr. The alloy with the highest Zr concentration showed the highest value of hardness. Overall, the hardness values obtained for this category of alloys are lower than values obtained for other series. This could be related to the lower Al concentration leading to the absence of intermetallics that contribute to the hardness of the material or the absence of significant fraction of the amorphous phase.

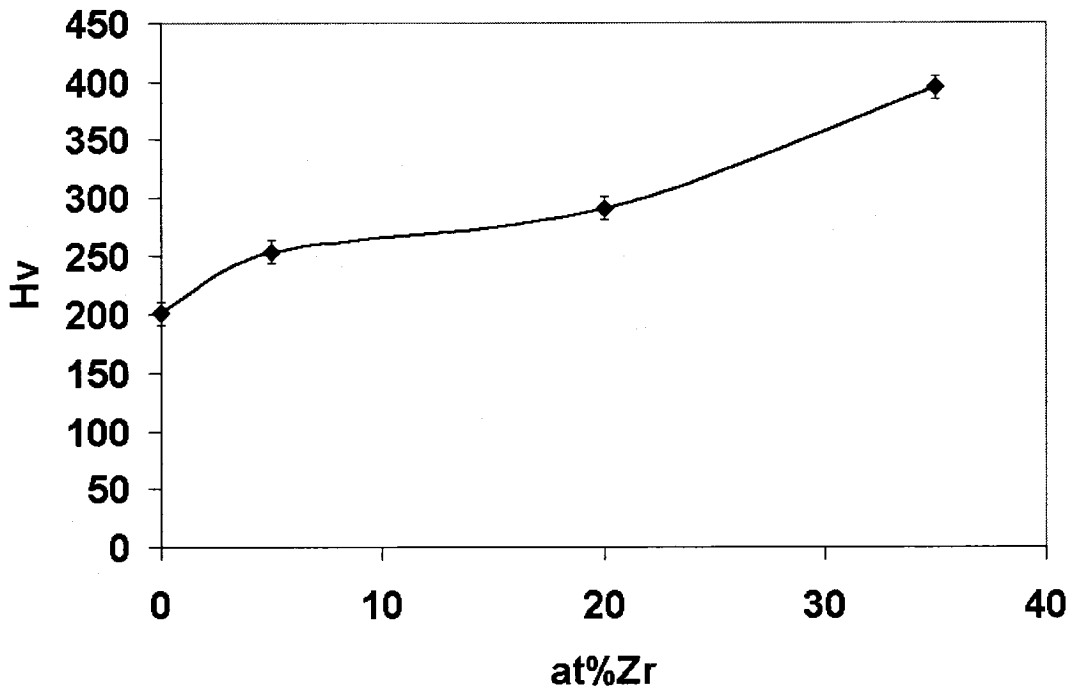

Figure 4.42: Hardness values at different Zr concentrations for the Low Al-containing alloys.

4.5 High Al-Containing Alloys

In this category of alloys, the Al concentration was maintained at 40 at.% while varying the Zr content according to the nominal composition of $Al_{40}Mg_{60-x}Zr_x$ (x = *0, 5, 20 and 35 at.% Zr*).

4.5.1 XRD Studies

Phase evolution for this series of alloys was followed using XRD analyses. The X-ray patterns of as-milled and heat-treated alloys are shown in Figures 4.43 and 4.44, respectively.

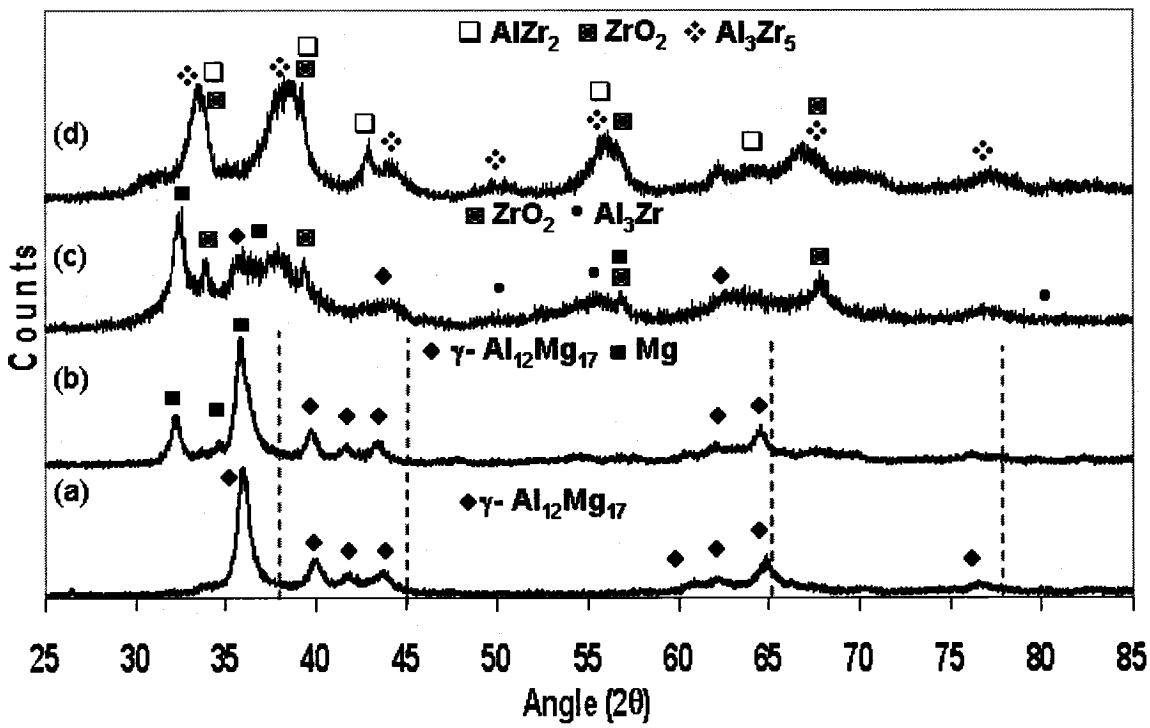

Figure 4.43: XRD patterns for as-milled Al-Mg-Zr alloys with different Zr contents; (a) 40Al-60Mg, (b) 40Al-55Mg-5Zr, (c) 40Al-40Mg-20Zr, (d) 40Al-25Mg-35Zr.

For the binary alloy containing 40 at% Al, the γ-$Al_{12}Mg_{17}$ intermetallic was the main phase present after milling, which remained stable after annealing. For this particular composition, the phase evolution is in agreement with the predictions of the equilibrium Al-Mg diagram. Therefore, upon annealing, no phase transformations were observed by XRD, except for some narrowing noted from the X-ray peaks upon annealing, which indicates grain growth and stress relaxation.

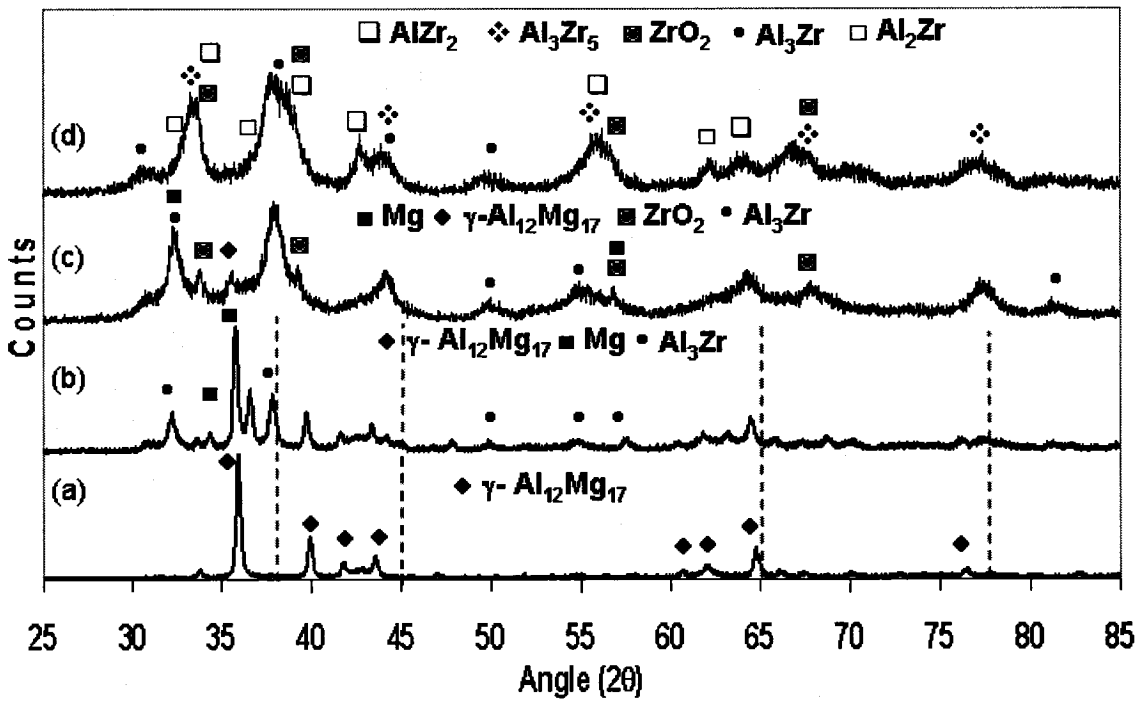

Figure 4.44: XRD patterns for annealed Al-Mg-Zr alloys; (a) 40Al-60Mg, (b) 40Al-55Mg-5Zr, (c) 40Al-40Mg-20Zr, (d) 40Al-25Mg-35Zr.

Upon introducing 5 at.% Zr to the alloy, it forced some Mg to dissociate from the intermetallic phase, thus remaining unalloyed. This could be related to the negligible

solubility of Zr in Mg and the fact that Mg and Zr do not form any intermetallic compounds. It was not possible to detect Zr in as-milled alloys which might be due to the detectability limit of the X-ray diffractometer, the low concentration of Zr, or the presence of Zr in the form of an amorphous material. The γ-phase was identified after heat-treating the alloy, which is indicative of the thermal stability of the phase. Along with that phase, Al_3Zr intermetallic was detected in which the annealing energy promoted its formation.

When the Zr concentration was increased to 20at% small traces of γ-phase were present in addition to Al_3Zr and some unalloyed Mg. Moreover, Zr oxidation was detected which is attributed to the higher affinity between Zr and O. Upon annealing, the presence of unalloyed Mg and Al_3Zr was maintained with the appearance of larger amounts of γ-$Al_{12}Mg_{17}$. The Al-Zr intermetallic showed good thermal stability and no phase transformation was observed.

Some Al-Zr intermetallics appeared after milling the alloy containing 35 at.%Zr, which then transformed into more thermodynamically stable phases upon annealing. The equilibrium phases did not form upon milling and the formation of less stable intermetallics was observed. A high temperature phase like Al_3Zr_5 formed during milling, which indicates the degree of deviation from equilibrium state of this process. Along with the aforementioned intermetallic phase, traces of $AlZr_2$ and ZrO_2 were detected. Upon annealing, partial return to the equilibrium state was observed evidenced by the presence of some equilibrium phases at this Zr concentration, i.e.

Al_2Zr. However, the non-equilibrium phases obtained in the as-milled state were still present which might be related to the duration of the annealing process, i.e. higher temperatures or longer times are needed to initiate phase transformation; although traces of the more stable Al_3Zr were detected. For this particular composition, however, no Mg was detected and traces of ZrO_2 were obtained. No Al-Mg intermetallics were found to form at Zr concentrations exceeding 20 at.%, which reflects the higher stability of Al-Zr intermetallics over Al-Mg.

4.5.2 TEM Studies

Figure 4.45 shows a BF-TEM image of the binary alloy of nominal composition 40Al-60Mg. Additionally, the selected area diffraction pattern taken from the center of this particle "region A" is shown in the same figure. From the diffraction pattern, no signs of amorphization are observed, but instead the presence of clear continuous diffraction rings. The interplanar spacings were determined to correspond to the γ-phase, which is the predominant phase from the X-ray diffractograms in both as-milled and annealed alloys. This can be confirmed by considering the d values obtained from the diffraction rings Figure 4.46 which correspond with those reported for the γ-phase. The results are presented along with their space groups in Table 4.1.

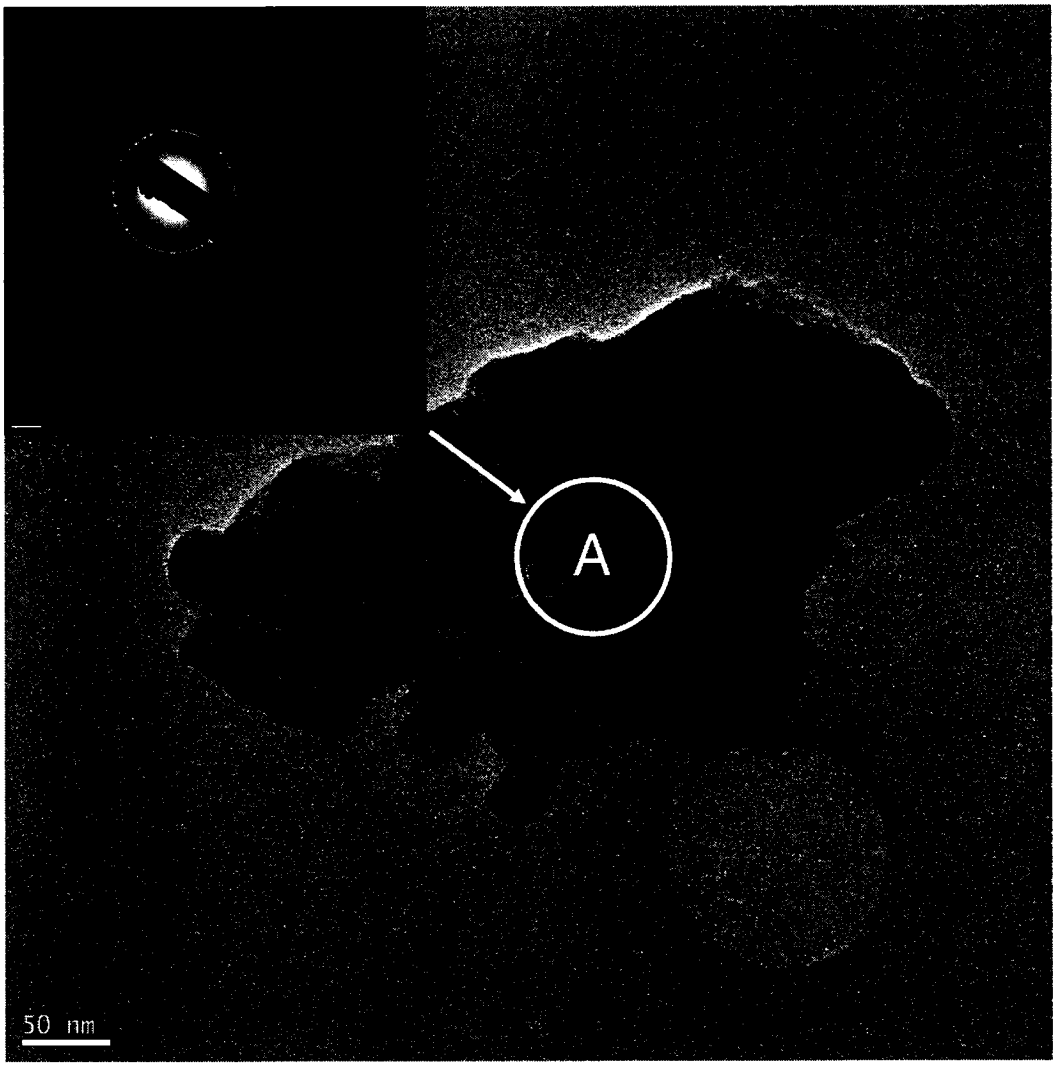

Figure 4.45: TEM image of binary 40Al-60Mg alloy along with SADP showing complete crystallinity.

Figure 4.46: d values taken from SADP of the as-milled 40Al-60Mg alloy, corresponding to the γ-$Al_{12}Mg_{17}$ intermetallic phase.

Table 4.1: d values corresponding to γ-phase observed in the as-milled 40Al-60Mg alloy.

(h k l)	Location (2□)	Reference value (Å)	Measured d value (Å)
330	36.191	2.48	2.48
332	40.227	2.24	2.27
510	43.917	2.06	2.07
550	62.260	1.49	1.5
721	65.186	1.43	1.44

A BF-TEM image of the alloy containing 5 at.% Zr is shown in Figure 4.47. Moreover, the EDS analysis of the whole particle and the selected area diffraction pattern (SADP) taken from the center "region A" and corner "region B" of a particle (circled area) are presented in the same figure.

The continuous rings that can be seen from the diffraction patterns taken from the center location reveal the presence of a highly crystalline material and non-existence of an amorphous phase. However, the SADP taken from the corner of the particle shows lower degree of crystallinity and the possible coexistence of crystalline and amorphous phases, but with low proportions of the latter. However, there is a contribution in such case from the location where the DP was taken from the grid material in this case since it was difficult to only confine the corner location.

Therefore, the Al-Mg binary alloy and the alloy containing 5 at.% Zr showed neither a nanocomposite structure nor an amorphous phase, emphasizing that the addition of adequate amounts of the transition element is crucial to promote amorphization in these types of alloys.

For the ternary alloy containing 20 at.% Zr, the TEM image of the selected particle is shown in Figure 4.48. In the same figure, the EDS analysis and the SADPs of both regions (center "A") and (corner "B") are also shown. It should be mentioned here that the same alloy was presented in the *High Mg-alloys* section. Therefore, for comparison purposes and detailed analysis refer to the *High Mg-containing* alloys.

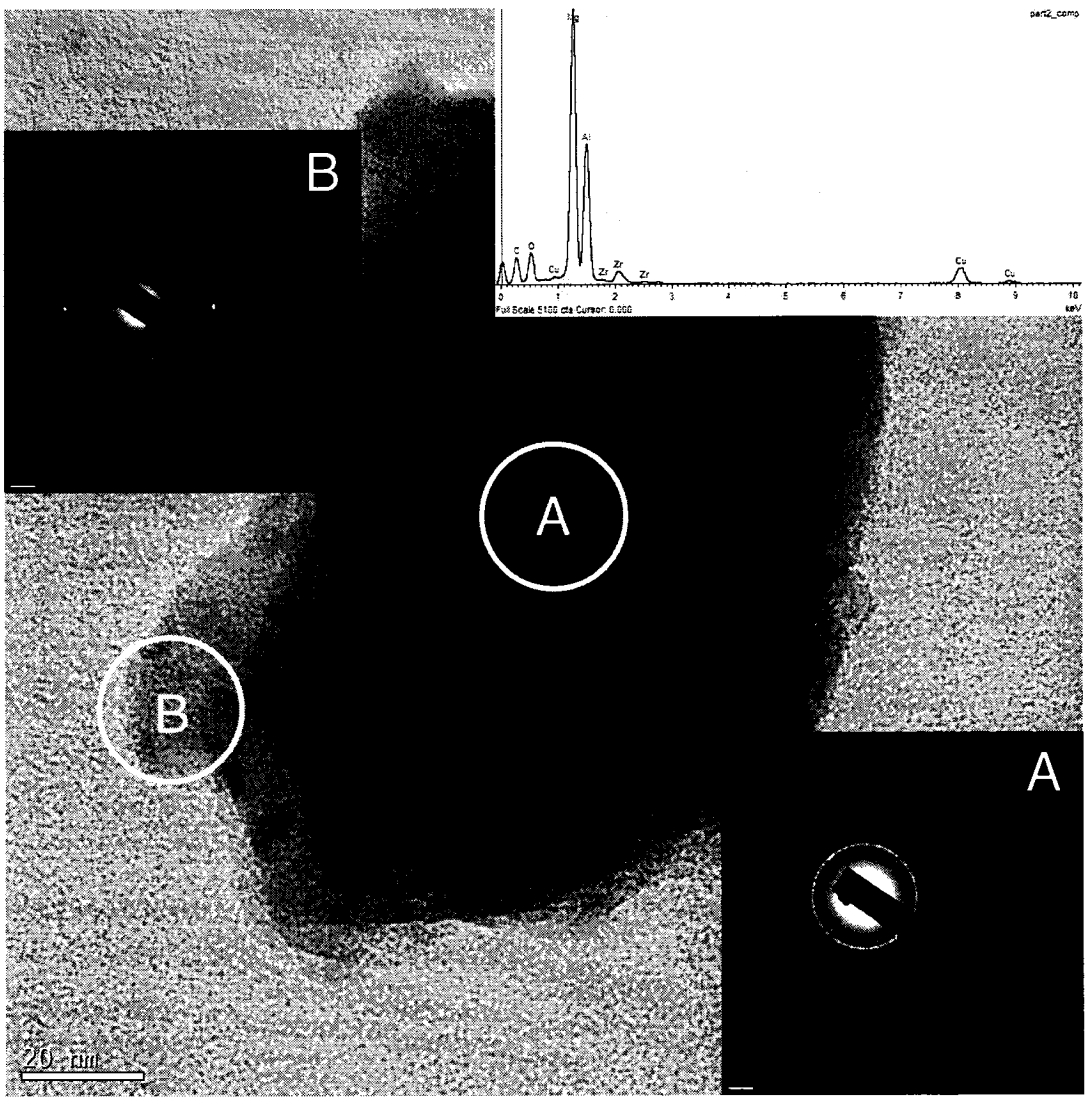

Figure 4.47: TEM image of as-milled ternary 40Al-55Mg-5Zr alloy, showing EDS and SADPs taken from two locations.

As with other high-Zr containing alloys, the SADP image taken from location "A" shows a halo-diffraction typical of fully amorphous alloys. It was revealed earlier that this is due to the higher thickness of the particle at this location evident by the

thickness contrast. The accumulation of structural defects leads to blockage of diffracting planes.

On the other hand, it can be seen that traces of amorphous phase were clear from diffraction patterns (DP) of the second location "B". The nanocomposite structure was obtained in this alloy which is manifested by the coexistence of diffraction spots along with halo-diffraction patterns, typical of amorphous structures. The BF diffraction pattern and HR-TEM image taken from this alloy were also shown previously into the category of *High Mg-alloys*.

The TEM image of the alloy containing 35 at.% Zr is shown in Figure 4.49, accompanied by the corresponding EDS analysis for the whole particle and the SADPs taken from both areas "A" and "B". It can be observed that when the Zr concentration was increased to 35 at%, a nanocomposite structure was not obtained as can be seen by the continuous diffraction rings from SADPs, since the presence of an amorphous phase cannot be inferred from these DPs. To study these observations closely, high-resolution TEM was carried out in order to reveal the internal structure of the material and to confirm the absence/existence of an amorphous phase. The high resolution image taken from a corner region is shown in Figure 4.50 which shows no clear presence of an amorphous phase manifested by the presence of atomic planes.

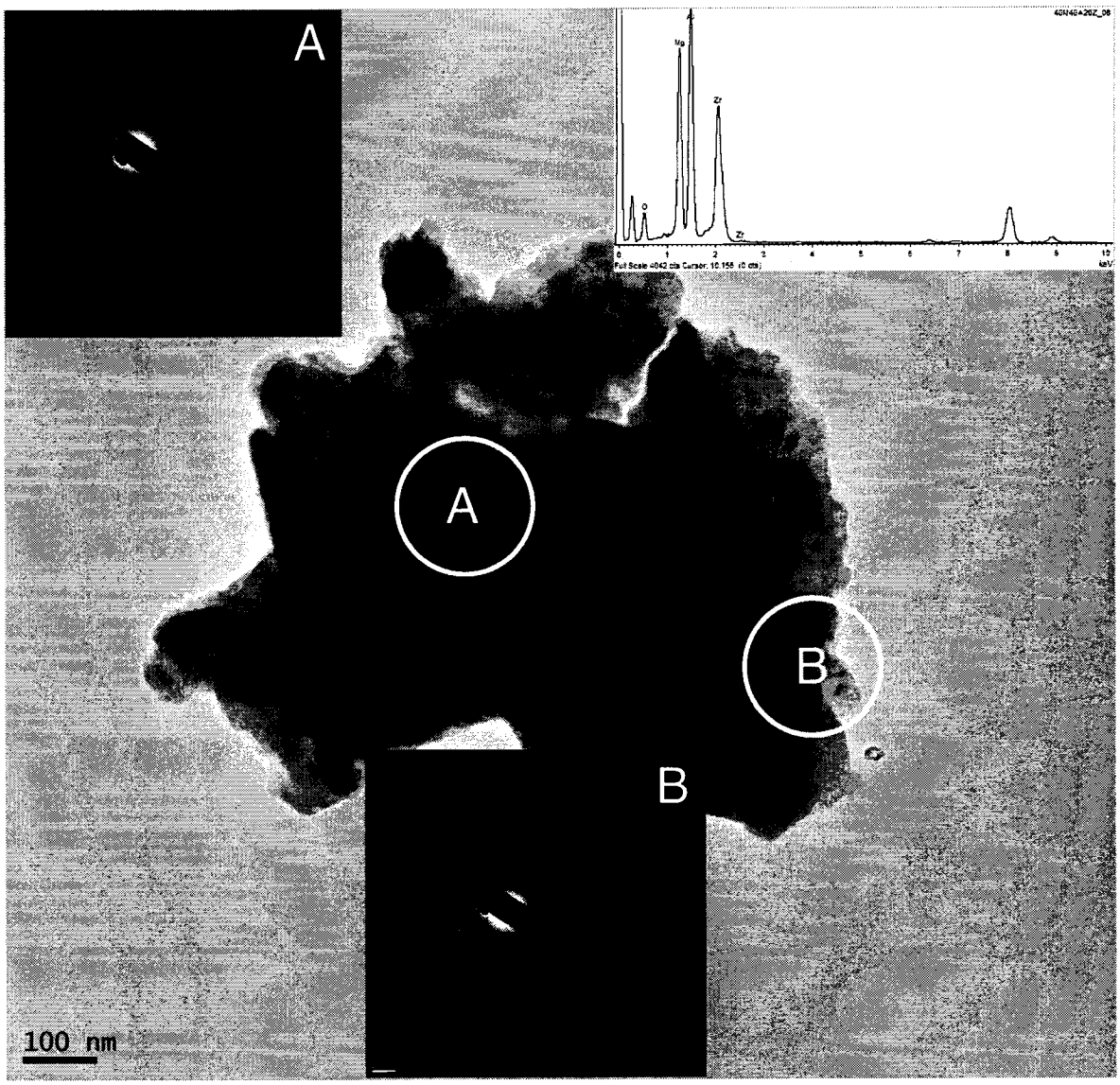

Figure 4.48: BF-TEM image of as-milled 40Mg-40Al-20Zr alloy.

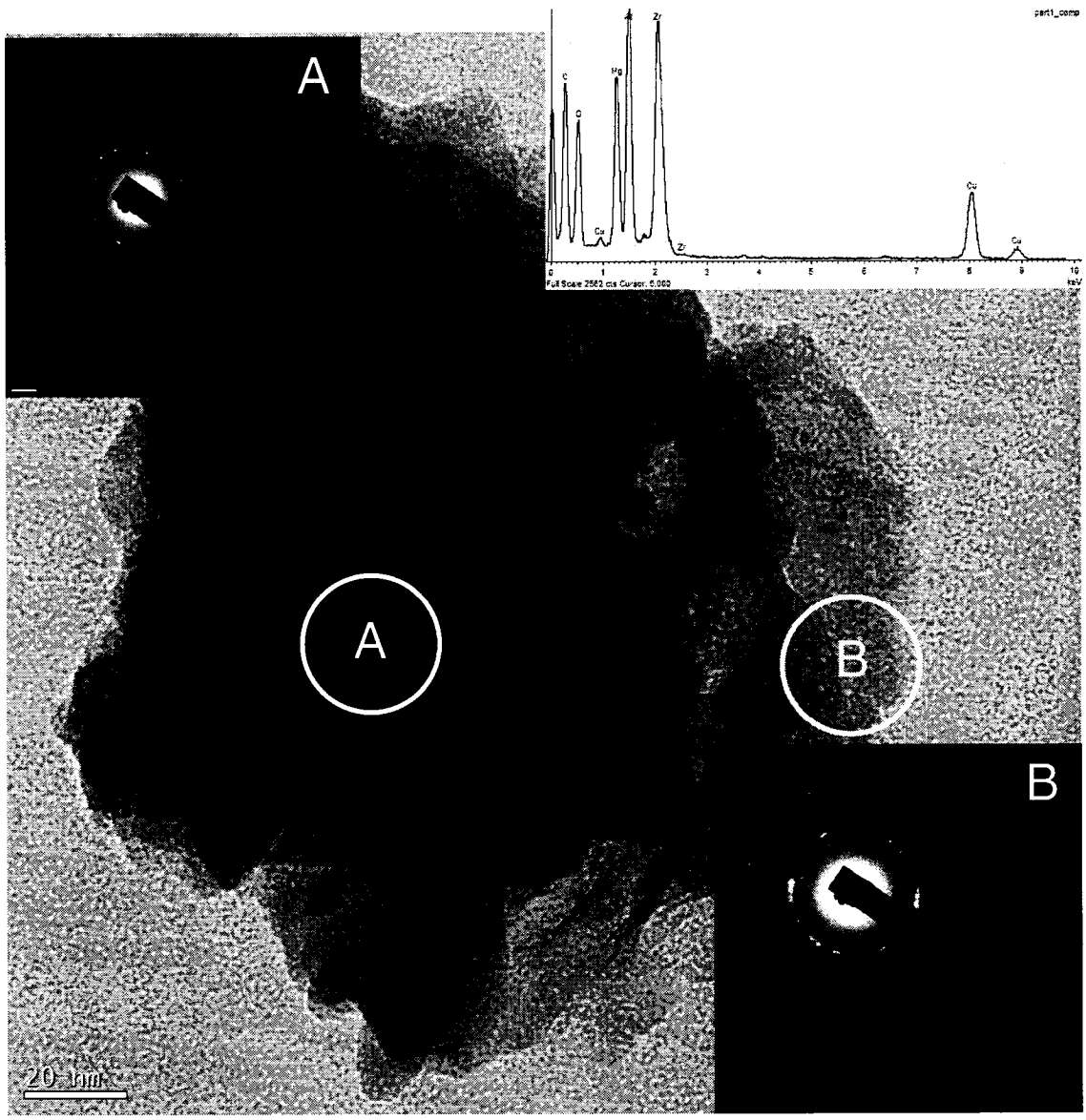

Figure 4.49: BF-TEM image of as-milled 40Al-25Mg-35Zr alloy.

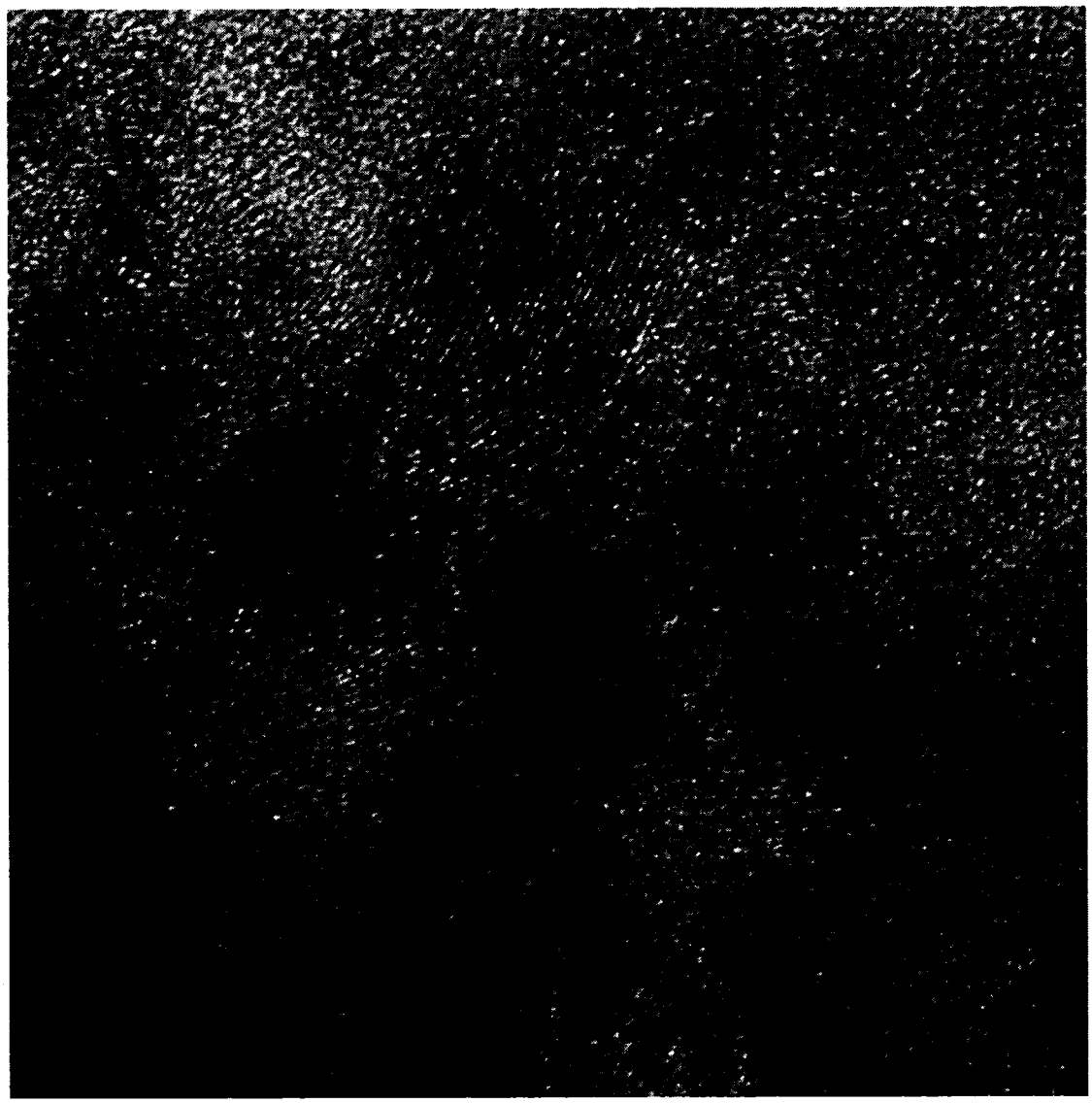

Figure 4.50: High resolution TEM image of the corner position showing no amorphous phase and perfectly ordered crystalline structure.

This might be due to the presence of local concentration of some elements which promote crystallinity. To further study this possibility, an EDS analysis was performed at the corner location and shown in Figure 4.51. It can be seen from the EDS analysis that this particular area is Mg-rich which might be responsible for the absence of an amorphous phase at the corner of the alloy. The observation of the possible

dependence of amorphization on local concentration needs more in-depth investigation which can be performed by closely studying other corner locations or even other particles.

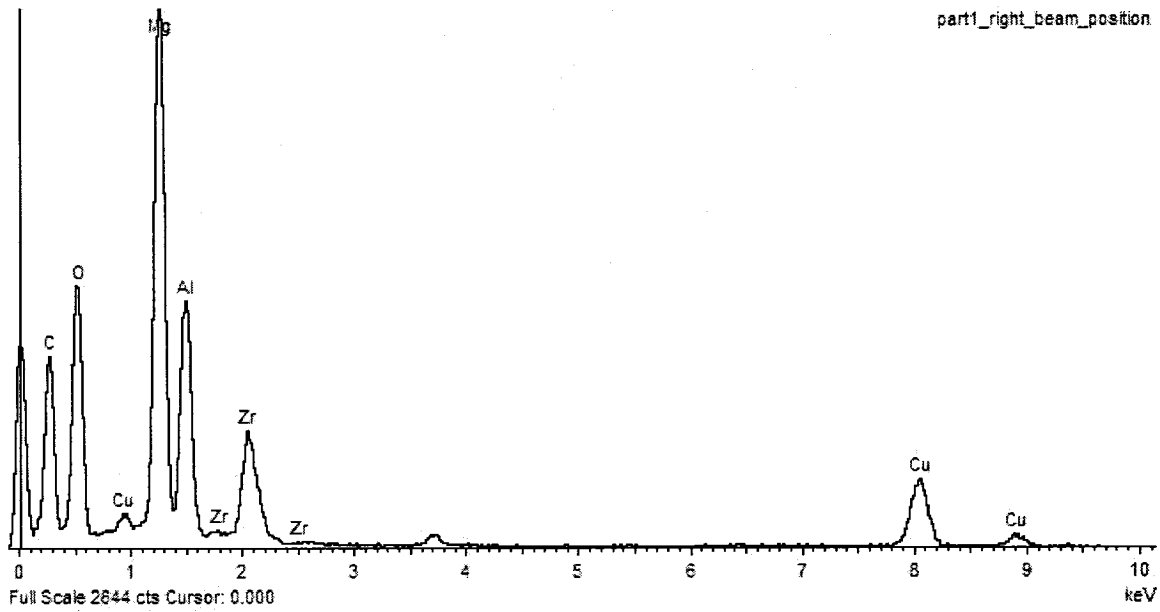

Figure 4.51: EDS analysis of the corner position of the as-milled 40Al-25Mg-35Zr alloy.

For that reason, another particle of the same composition was considered and shown in Figure 4.52. The SADP taken from the center and the corner locations of the particle regions "A" and "B" are also shown in the same figure. It can be seen that continuous rings exist from both locations indicating crystallinity and lack of halo-diffraction patterns, associated with the presence of an amorphous phase. To complement these observations, a high resolution TEM was obtained to study these findings closely.

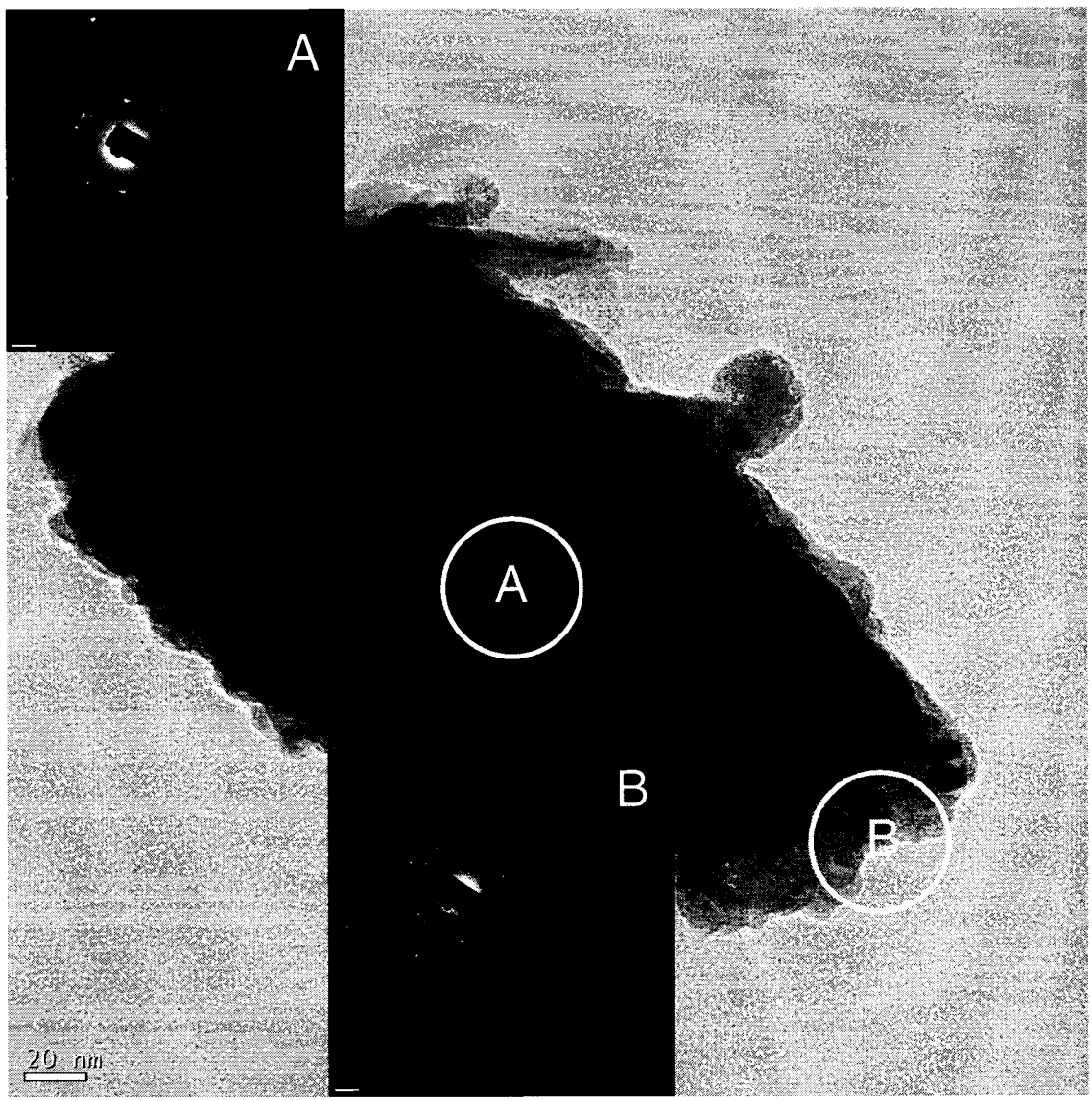

Figure 4.52: TEM image of a second particle to further study the absence of amorphous structure in the as-milled 40Al-25Mg-35Zr alloy.

The HR-TEM taken from region "B" of the particle under study is shown in Figure 4.53. By carefully examining this HR image, it can be observed that small fractions of amorphous phase exist, which were not detected in the SADPs. To ensure that this

observation is not limited to the tiny area under study, the HR-TEM was taken from another location at the bottom of the particle and shown in Figure 4.54. It also confirms the presence of a small fraction of amorphous phase, evidenced by the lack of ordered atomic planes at some locations.

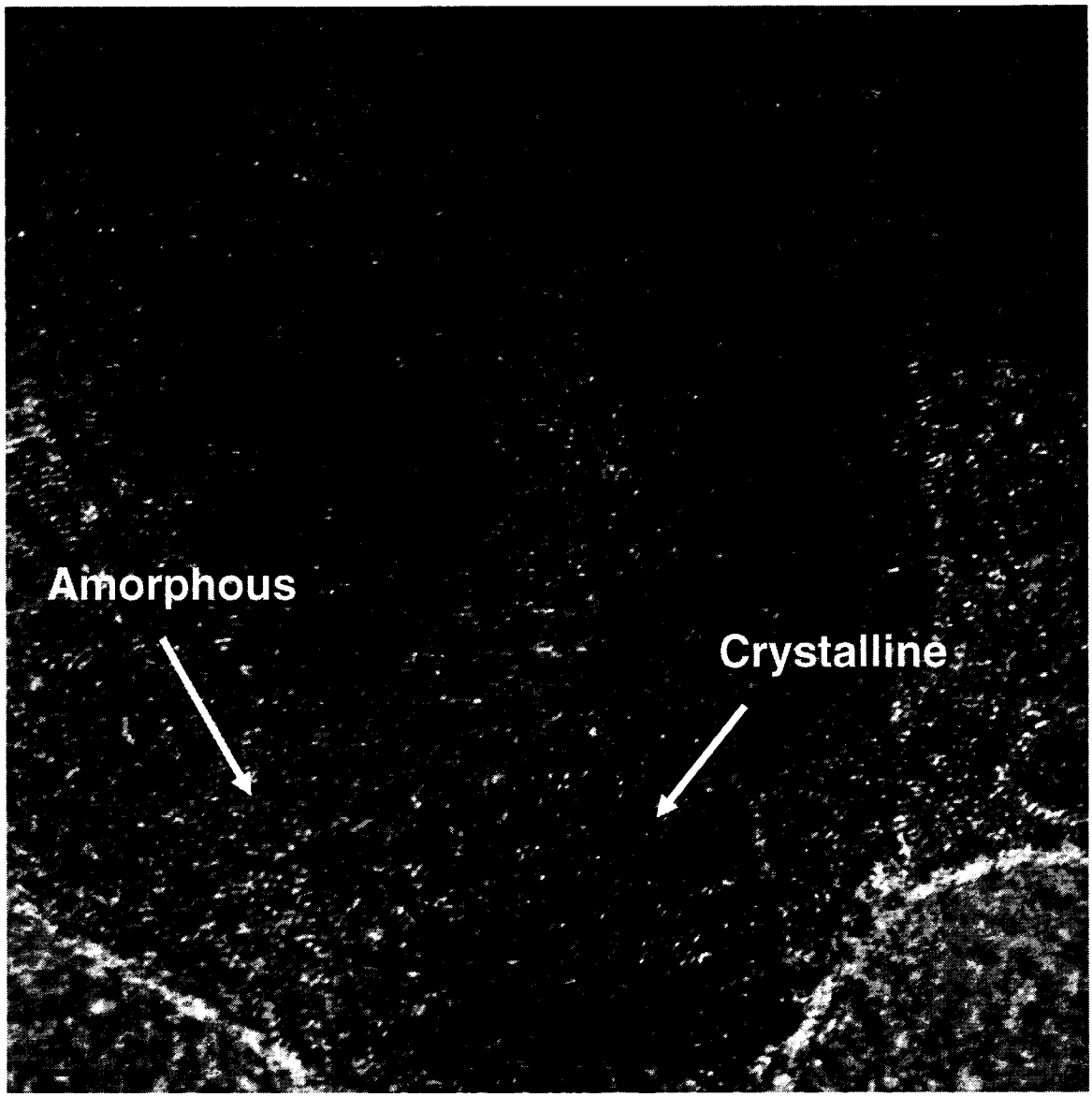

Figure 4.53: HR-TEM image of the bottom location "B" showing the presence of a small fraction of an amorphous phase that might not be seen by SADP.

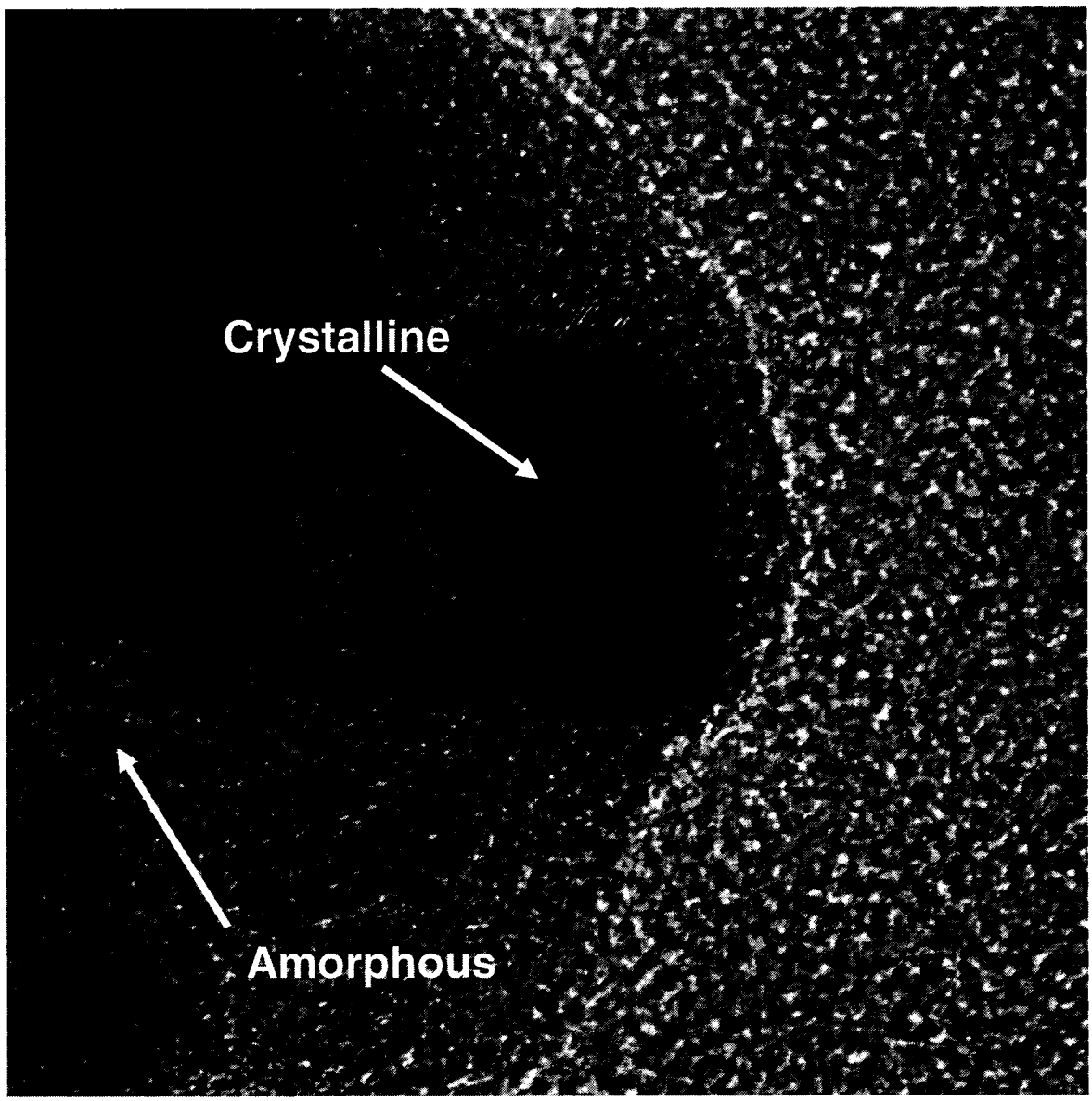

Figure 4.54: HR-TEM image of another corner region located at the bottom of the sample, confirming the presence of small fraction of an amorphous phase.

An EDS analysis of such areas was obtained to investigate the possible presence of any local compositional gradient, and is shown in Figure 4.55 which reveals higher Zr-concentrations. This emphasizes the role that Zr plays in the amorphization of Al-Mg

alloys, explaining the presence of a fraction of amorphous phase at the corner regions of the particle. This observation is governed by the presence of high Zr concentrations into the alloy since in previously considered case, where Zr concentration was high in some areas, no amorphization was obtained (Figure 4.34). An additional observation is the low Mg concentration at this location which might be another reason for the presence of an amorphous phase. The lack of substantial amount of amorphous phase in this particular alloy might be attributed also to the higher oxidation rate, observed from X-ray patters, leading to increased crystallinity in the alloy, unlike the alloy containing 20at%Zr, where more Zr is free to promote the formation of an amorphous phase.

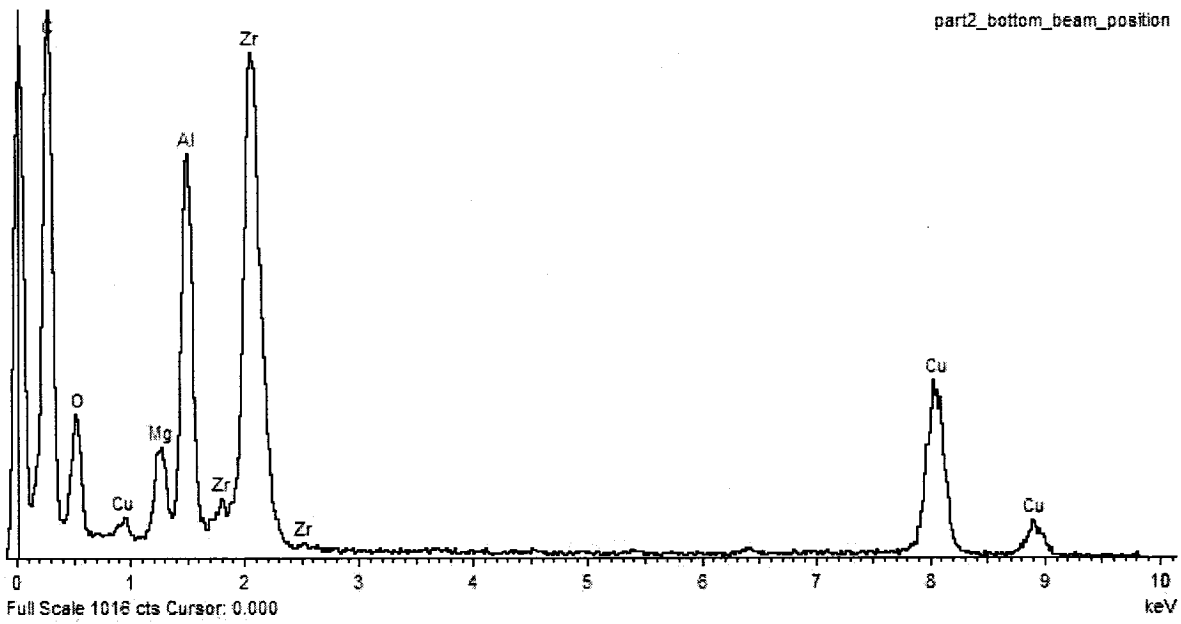

Figure 4.55: EDS analysis of a partially amorphous region of an as-milled 40Al-25Mg-35Zr alloy, showing a Zr-rich location with a minor amount of amorphous phase.

4.5.3 Crystallite Size Measurement

The crystallite sizes of the resulting alloys in both as-milled and annealed conditions with different Zr contents are shown in Figure 4.56. The determination of crystallite size was performed via direct TEM observation using bright and dark field images. In the as-milled state, no considerable change in crystallite size was observed in the whole Zr interval, however, a marked increase was obtained in the heat-treated powders for the binary and 5at.% Zr alloys. The apparent stability in the grain structure as the Zr content increases to 20 and 35at%, as observed by the negligible grain growth, can be related to the presence of Al_3Zr, which contributes to the stability of the nanocrystalline structure via Zener-pinning action. In general, both high Zr containing alloys presented a nanocomposite structure and good structural stability when exposed to isothermal annealing conditions. Bright field TEM images of the alloy containing 35at%Zr are shown in Figure 4.57 for comparative purposes.

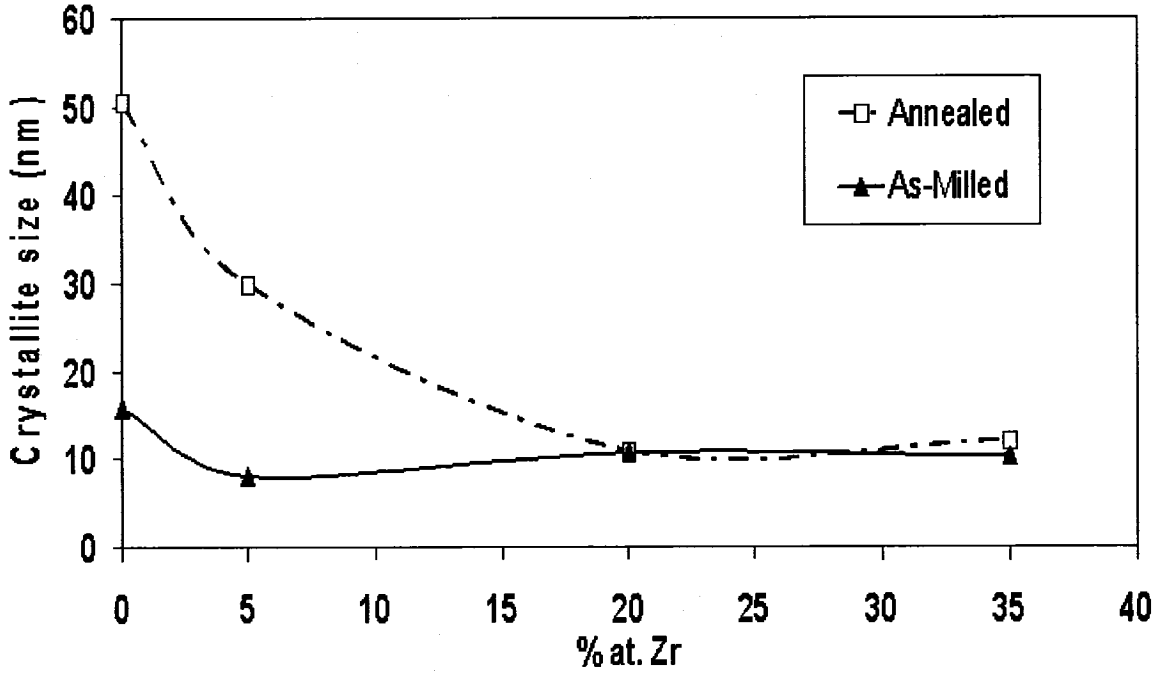

Figure 4.56: Crystallite size at different Zr concentrations for as-milled and annealed High Al-containing alloys.

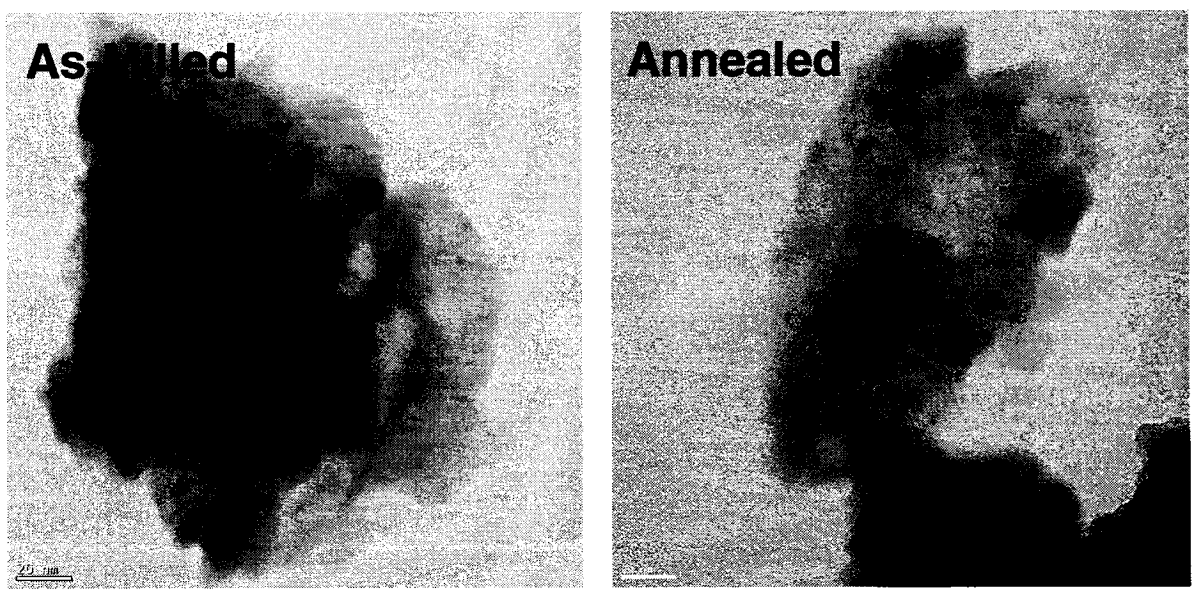

Figure 4.57: Bright field TEM images used for crystallite size determination for as-milled and annealed 40Al-25Mg-35Zr alloy.

4.5.4 Hardness Measurements

The hardness measurements of the resulting alloys were taken from compacts in order to evaluate the effect of Zr addition. Figure 4.58 shows that improvement in hardness by adding Zr to the binary alloy follows a parabolic behaviour. For the alloys containing more than 5at%Zr, this increase in hardness might be due to the presence of zirconium oxide. Among all the alloys under investigation, the alloy containing Zr concentration of 35at% in this category represented the highest hardness value, which is very close to the alloy containing 35at%Zr in the *Low*-Mg alloys group.

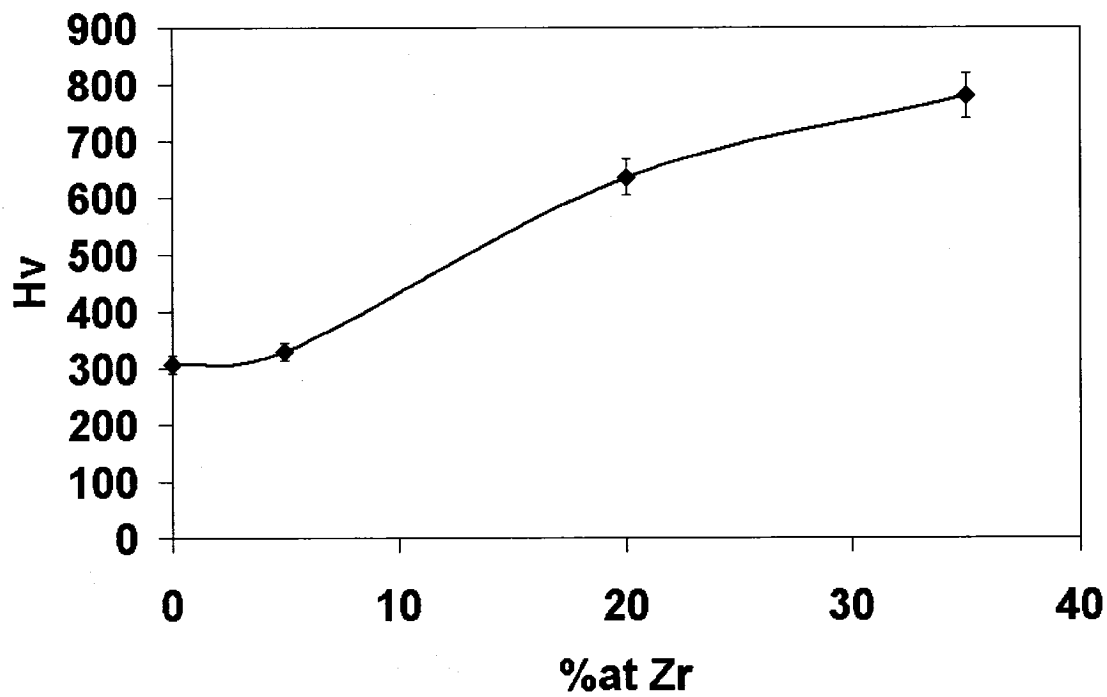

Figure 4.58: Variation of hardness with different Zr concentrations.

Chapter 5

Comprehensive Discussion

Considering all the results presented earlier, this section is intended to provide a comprehensive summary in order to compare the different types of alloys prepared in this study and to highlight the main observations and conclusions. For the upcoming section, a comparison between the results will be considered in terms of different aspects which can be summarized in the following points:

- The effect of employing mechanical alloying to promote the deviation of these systems from equilibrium state. More specifically, in extending the homogeneity range of the γ-$Al_{12}Mg_{17}$ phase and in the formation of the Al_3Zr intermetallic.

- The effect of different compositions on the formation of the nanocomposite structure, comprising nanocrystalline and amorphous phases.

- The role of Zr on crystallite size and in retarding grain growth.

- The stability of the as-milled structure.

- The variation of hardness with Zr different contents and alloy composition.

As a starting point, the alloys will be presented as an Al-Mg-Zr ternary diagram to view the location of each composition and the area covered by each category. Figure 5.1 shows the location of the alloys, in which each category of alloys is marked. As observed, the alloys are located mainly on the left side of the diagram where Zr varies between 0 and 35at%. This diagram will be used in order to assess the formation of some metastable phases and the possible deviation from equilibrium due to the use of mechanical alloying. Moreover, the compositions where the nanocomposite structure was obtained will be highlighted in similar diagram.

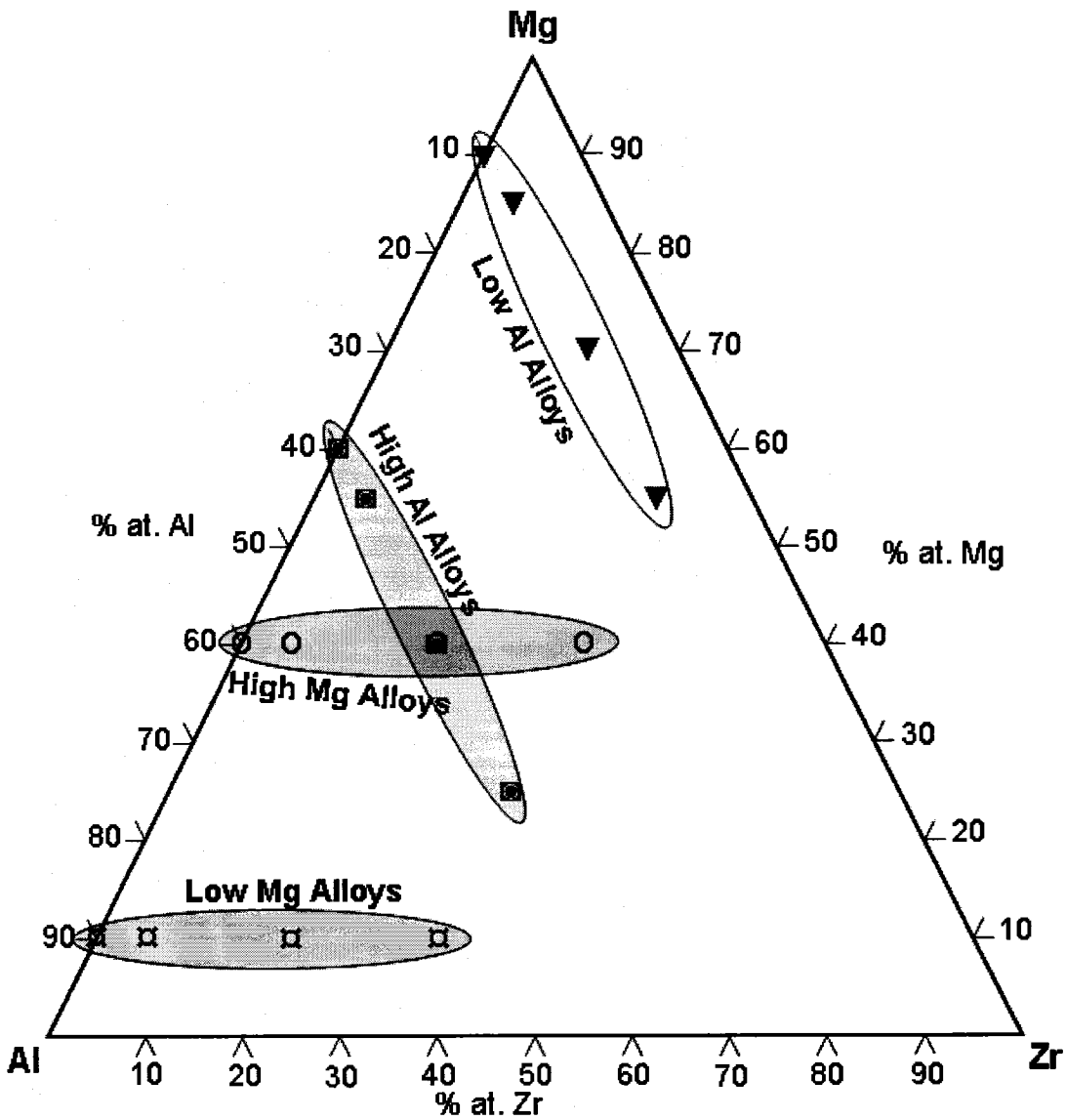

Figure 5.1: Location of the alloy groups in an Al-Mg-Zr ternary diagram.

5.1 Extended Homogeneity Range of γ-phase

It was stated earlier that one of the main characteristics of mechanical alloying is the possibility of forming metastable phases at homogeneity ranges beyond

equilibrium values. This advantage was the main focus for several research papers, especially for Al-Mg alloys [34, 33]. In this present study, the deviation from equilibrium imposed by mechanical alloying is assessed in terms of the formation and extension of solubility limits of γ-$Al_{12}Mg_{17}$. The γ-phase has a cubic structure and forms in the binary Mg-Al alloys at equilibrium conditions and Mg concentrations between 45 and 60.5at%. The earlier study by Zhang et al. [34] have shown that the homogeneity range of the γ-phase could be extended to values between 60 and 80at.% Mg. Additionally, reports by Singh et al. [33] have highlighted the extension of homogeneity range for this intermetallic phase to values ranging from 50 to 70at% Mg. In addition to studying the effect of mechanical alloying on the extension of the γ-$Al_{12}Mg_{17}$ homogeneity range, the effect of ternary additions is considered.

The Mg compositional ranges where the γ-phase was detected in all alloys systems are shown in Figure 5.2. It can be seen that for the MAed binary alloys a noticeable deviation exists in the homogeneity range of the γ-phase compared to equilibrium values. The γ-$Al_{12}Mg_{17}$ was obtained in this research for values between ~ 40 and ~ 90 at.% Mg for as-milled alloys, although it was detected in minor quantities in some cases. Moreover, the γ-phase showed good thermal stability, being detected for Mg concentrations ranging from 50 to 90 at.%. The reduction in homogeneity range from 40 to 50 at.% Mg was due to the transformation of the γ-phase to the equilibrium β-phase which was promoted by annealing. Referring to Figure 4.60, it can be seen clearly that the obtained extension in homogeneity range of binary Al-Mg alloys in

this research was over a wider range of Mg composition compared to earlier work, which might be attributed to the milling conditions used in their research and the compositions they have studied.

However, it should be mentioned that due to the fact that the γ-phase was existing partially in some alloys, the actual Mg concentration for the formation of the phase is close to the value of the starting alloy powders. At this point, the extension in homogeneity range was explained solely by taking into account the non-equilibrium nature of the processing technique; the effect of adding Zr to the alloy, however, will be considered in the coming paragraphs.

Upon adding 5 at.% Zr, it can be seen that the homogeneity range of γ-phase was extended to Mg concentrations between ~ 40 and ~ 85at%. However, for the ternary alloy, there are no equilibrium values for Al-Mg-Zr to compare these values with, but the extension in homogeneity range was pronounced compared to the equilibrium values of the binary Al-Mg alloy. When the Zr content increased further to 20at%, the homogeneity range of the γ-$Al_{12}Mg_{17}$ reduced to values between ~ 40 and ~ 70%Mg. Moreover, the γ-phase was still present for alloys containing 35 at.% Zr but in compositions limited to ~ 55at%Mg only. This general trend suggests that upon increasing the Zr concentration into these alloys, the formation of γ-phase becomes more difficult due to the formation of zirconium aluminides, as will be explained in the next section.

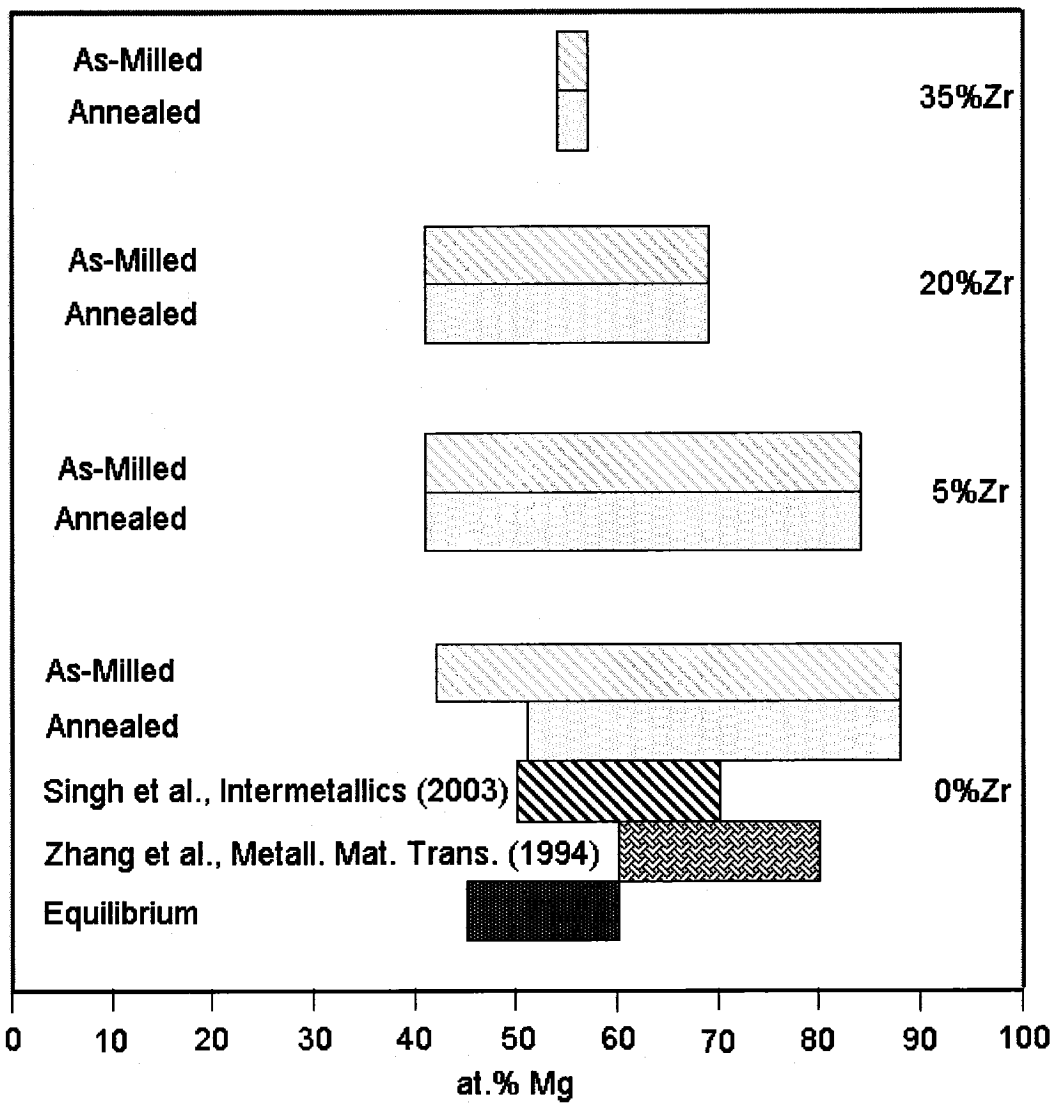

Figure 5.2: Homogeneity ranges of γ-phase a function of Mg concentration.

5.2 The Formation of Al_3Zr and the Extension of Homogeneity Range

In this research, Al_3Zr appeared in most cases of Zr compositions in the as-milled and/or annealed states. This phase can be present in two crystal forms, the $L1_2$ cubic

structure, considered as a metastable structure and the equilibrium tetragonal DO_{23} structure at room temperature. It has been stated earlier that retaining this intermetallic phase in the $L1_2$ structure shows to be beneficial in providing desirable mechanical properties in terms of improved ductility, as compared to the tetragonal DO_{23} phase, which causes embrittlement in the alloy. The formation of Al_3Zr intermetallic in the $L1_2$ cubic structure can also be beneficial in improving the high temperature properties of structural materials [89]. This was attributed mainly to the fact that Al_3Zr has a density of 4.1 g/cm^3 and a melting temperature of about 1580°C.

Despite the fact that $L1_2$ cubic structure is a high temperature phase, the employment of MA was beneficial for the formation of this phase, also suppressing the transformation to the tetragonal DO_{23} crystal structure. In other cases, the transformation of this phase into the cubic structure was promoted by annealing.

The departure from equilibrium in terms of the formation of the Al_3Zr phase at different compositions is evaluated in Figure 5.3. It can be seen that the Zr compositions leading to the formation of the Al_3Zr are bounded to values between 25 and 35 at% in the binary Al-Zr alloys produced under equilibrium conditions. Referring to Figure 5.3, it is noted that for the alloys containing Zr concentrations of 24 and 33at%, the formation of Al_3Zr can be obtained under equilibrium conditions

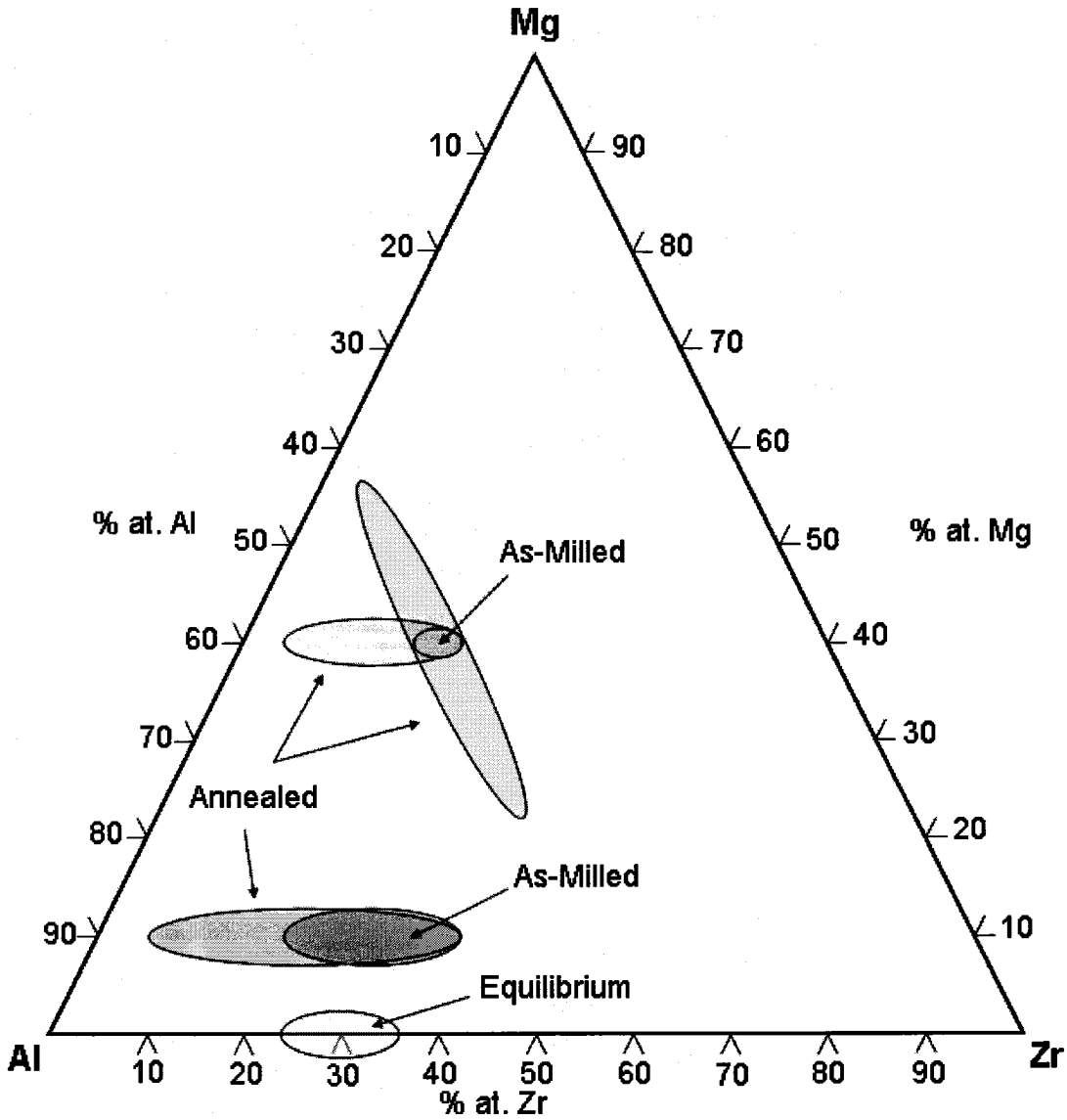

Figure 5.3: Departure from equilibrium in the formation of Al_3Zr caused by the nature of the mechanical alloying process.

. In this case, some departure from equilibrium concentrations is observed, with the formation of this intermetallic extending from 20 to 35 at.% Zr in the as-milled

condition. This was observed in the *Low Mg-containing* alloys, where the formation of zirconium tri-aluminide extended post-annealing to values as low as 5 at.%Zr.

In the case of *High Mg-containing* and *High Al-containing* alloys, the formation of Al_3Zr was limited in the as-milled condition to a value of 20 at.% Zr. This might be due to the high Al concentration into these alloys, leading to the formation of other non-equilibrium Al-Zr intermetallics. However, after annealing, the formation of Al_3Zr was observed through a wider compositional range. For the *High Mg-containing* alloys, the homogeneity range of this intermetallic was extended to values between 5 and 20 at.% Zr. As for the *High Al-containing* alloys, it was extended through a wider range of Zr content, i.e. Zr concentrations from 5 to 35 at.%. For some compositions where the formation of such a phase can be predicted from the phase diagram, the formation of Al_3Zr occurred after annealing. For the *Low Al* containing alloys, the formation of this phase was not observed in either as-milled or annealed conditions which can be explained by the low Al content. This highlights the role of Al in the formation of Al_3Zr in which there exists a minimum concentration of Al required to promote the formation of the Al_3Zr.

In general, the interest in Al_3Zr is mainly due to the fact that, in addition to improving ductility, it seems to contribute significantly to the stability of the nanostructure. However, this particular observation will be addressed in more detail in one of the upcoming sections.

To have a more appropriate assessment of the deviation of mechanical alloying in terms of formation of Al_3Zr beyond the equilibrium values, the results obtained in this research should be compared to values obtained from the ternary Al-Mg-Zr phase diagram not to the binary Al-Zr phase diagram. However, the existing ternary Al-Mg-Zr phase diagrams from literature were depicted for specific temperatures and due to the randomness nature of mechanical alloying process it was not possible to find the exact temperature in which the alloying process is occurring. Moreover, it was stated in the literature review chapter that until now, no study was able to accurately determine the milling temperature because the alloying action occurs randomly at local collision points in the milling container.

5.3 Formation of the Nanocomposite Structure

In this research, the development of the nanocomposite structure was observed for the first time in Al-Mg-Zr ternary alloys. Such a structure, comprising of nanocrystals embedded into an amorphous matrix, was developed using mechanical alloying. These alloys are expected to have improved mechanical properties in addition to good thermal stability.

The compositions where the nanocomposite structure was obtained are shown in the ternary Al-Mg-Zr diagram, Figure 5.4. It can be seen that this nanocomposite structure was observed in all cases where the Zr concentration exceeded 20 at.% Zr, regardless of the Al concentration.

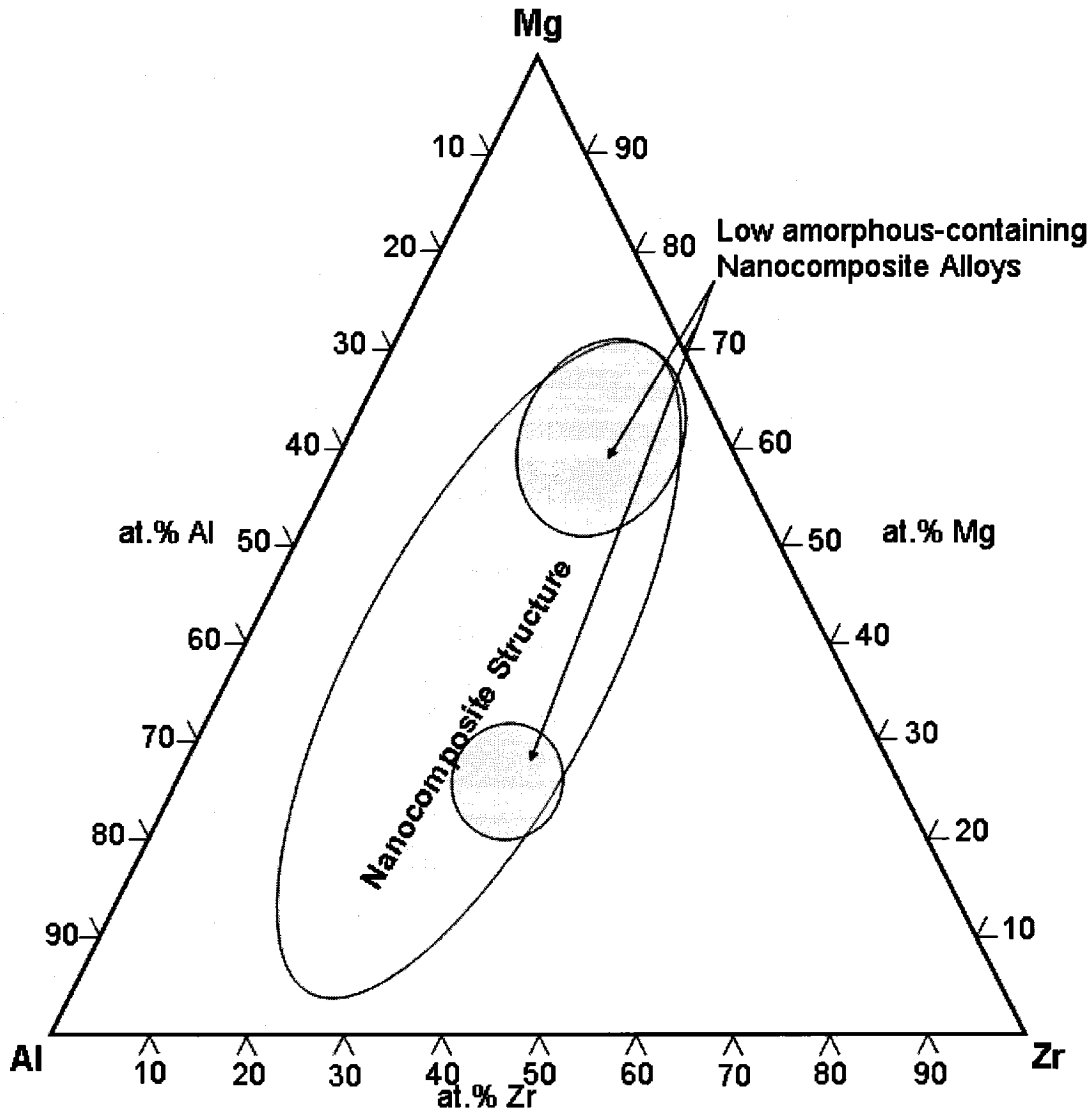

Figure 5.4: Location of the nanocomposite structure as observed in this research.

Nevertheless, the fraction of amorphous phase was not the same in all cases and for some compositions the presence of amorphous phase was found in residual amounts. As observed, the nanocomposites comprising low fraction of the amorphous phase occurred in alloys containing *Low Al* concentrations, close to 10at%. An additional observation is that in some alloys, $Al_{40}Mg_{25}Zr_{35}$ in particular, there exist

some Mg-rich areas where the nanocomposite structure was not observed. This suggests that Mg does not promote the formation of the amorphous phase, which might be related to the smaller fraction of amorphous phase observed in the *Low Al-containing* alloys.

5.4 Crystallite Size Formation and the Role of Zr in Retarding Grain Growth

5.4.1 Stability of Metastable Cubic $L1_2$ Al_3Zr Dispersoids

One of the main concerns in developing nanomaterials is the stability of the structure since nanomaterials produced by MA are considered being in a metastable state and grain growth may occur upon exposure to higher temperatures. Thus, the interest in studying the factors affecting the stability of the crystal structure and the possible suppression/minimization of grain growth with the addition of particular elements/second phases has grown recently in nanomaterials research. In this study, thermal stability was of particular interest due to the formation of a nanocomposite material that comprises amorphous and nanocrystals in which both can undergo undesirable structural transformations upon exposure to high temperatures. Additionally, the factors affecting the stability of the nanocomposite structure will be considered in the following paragraphs where the role of Zr in stabilizing the nanostructure is discussed.

Earlier studies [90, 91] have shown that the formation of cubic $L1_2$ structured Al_3Zr dispersoids can be achieved via rapid solidification. In the study of Nes [91], the Al-Zr alloy was annealed at a temperature of 460°C and cubic structured Al_3Zr dispersoids were found to be stable up to a maximum annealing time of 700 h. However, in both of the aforementioned studies the Zr concentration was limited to a maximum value of 0.5wt%. Thus, with these low concentrations of Zr it was quite surprising to learn that the presence of these dispersoids has a profound influence on the stability of the nanostructures.

Other later studies [92, 93, 94] have also confirmed the formation of Al_3Zr intermetallic compound in the $L1_2$ cubic structure by implementing non-equilibrium processing routes, i.e. mechanical alloying and rapid solidification. However, different studies have reported different temperatures where Al3Zr transformed into the tetragonal equilibrium phase. In the work of Guo et al. [92] Al_3Zr was found to transform into the equilibrium DO_{23} tetragonal structure when the annealing temperature exceeds 500°C. These alloys were produced by rapid solidification and the Zr content was limited to a maximum value of 15at%.

In another study, Srinivasan and Chattopadhyay [95] processed Al-Ni-Zr alloys by rapid solidification and it was found that the Ll_2 cubic structure shows significant resistance to coarsening up to temperatures exceeding 425°C. Such behaviour was attributed to the similarities in structure and lattice constant between Al and Al_3Zr. The coarsening of Al_3Zr was evaluated in two cases; when present in Al_3Ni matrix and

when present in the Al matrix. It was found that the coarsening was lower in the latter case due to the presence of low energy coherent interfaces [95].

For studies of alloys produced by mechanical alloying, Suryanarayana et al. [89] milled blended powders of compositions Al-25%Zr-M (M= Fe and Ni) and successfully obtained the $L1_2$ structure in all cases; however with amounts depending on the content of the ternary element. In all cases the transformation of this phase to the equilibrium tetragonal structure occurred upon annealing to a temperature ~ 900°C, which seems to be high compared to other studies that found the cubic $L1_2$ structured Al_3Zr to be stable up to 600°C [57].

Another study [16] considered the formation of metastable Al_3Zr by employing MAing and the effect of elemental additions of Li, Cr, Fe, Ni, and Cu on the thermal stability of the prepared alloys. It was found that the metastable $L1_2$ cubic structure was stable up to 550°C in alloys containing 25%Zr. It was also reported that the addition of Li and Cr suppresses the transformation of the $L1_2$ phase up to 750 and 740°C, respectively.

On the other hand, and to highlight the importance of alloying elements on the stability and formation of Al_3Zr dispersoids, a model was developed by Robson and Prangnell [96]. They used an integrated modeling approach which predicted that the addition of Mg accelerates the precipitation kinetics of Al_3Zr compared to binary Al-Zr alloys. They also predicted that different Mg concentrations will have an effect on

the precipitation of dispersoids. However, in this research the Al_3Zr showed good thermal stability and no transformation was observed perhaps due to the lower annealing temperatures compared to previously reported data by other researchers where the cubic Al_3Zr was stable at even higher temperatures.

5.4.2 Effect of Al_3Zr in Retarding Grain Growth

Now for the effect of Al_3Zr on the suppression of grain growth, it is well-established that the formation of second-phase particles renders structural stability via the application of Zener drag force (pinning) on grain boundaries [97]. To have an overall and homogeneous effect on grain retardation it was stated that the distribution of the second-phase particles should be uniform throughout the whole structure, which is achieved by combining the right choice of alloying elements and the wise decision on materials processing. This combined effect will cause pinning of low- and high-angle boundaries by the existence of dispersed and closely spaced second-phase particles. These particles could form due to the process itself or during subsequent annealing and before recrystallization takes place [97].

These second-phase particles have a pinning effect on grain boundaries characterized by a significant increase in recrystallization temperature for the alloys. An additional reason for such an increase is attributed to the possible effect of these particles on the formation of more uniformly distributed dislocations. Furthermore,

these dispersion particles have noticeable stability which was attributed to the low solubility of the particle in addition to the low interfacial energy [90].

For the combined effect of different additions of alloying elements on Al-Mg alloys, a study by Lee et al. [98] indicated that good thermal stability was observed on Al-Mg-Sc-Zr alloys upon exposing these alloys to temperatures up to 550°C [98]. They also produced Al-Mg-Zr alloys by equal-channel angular pressing, finding that the alloy was not stable at temperatures above 277°C. However, they did not indicate if the formation of the tri-aluminide (Al_3Zr) phase was observed. The absence of this intermetallic will certainly affect the stability of the crystal structure. This might be the reason for the loss of thermal stability when exposing the alloy to temperatures higher than 277°C. This observation is different from the present study in which the tri-aluminide was present and imposed structural stability in most cases up to an annealing temperature of 400°C. This might be due to the low concentration of Zr in their alloy (only 0.2%) or the nature of the alloying process. They [98] concluded that the superior grain stability in the Al-Mg-Sc-Zr is attributed to the presence of $Al_3(Zr_xSc_{1-x})$ precipitates that are more stable at high temperatures. Other studies [61] also observed an improved grain stability due to the precipitation of $Al_3(Zr_xSc_{1-x})$ which showed effectiveness in inhibiting recrystallization. It is thought that the strong drag force is caused by the coherence with the Al matrix, such that pronounced recrystallization occurred when coherency is lost.

In this present study, it was shown in a previous section that the formation of Al_3Zr was extended over a wider range of Zr concentration especially in the post-annealing conditions. By looking into the results presented in chapter 4, it can be observed that the presence of this zirconium tri-aluminide proved to be beneficial in retarding grain growth in most cases. More evidence can be seen by referring to Figure 4.40, where the lack of grain stability in this category of alloys, "*Low Al-containing alloys*" can be attributed to the absence of Al_3Zr according to XRD. The low Al content in these alloys seem to be directly responsible for the lack of the formation of Al_3Zr. However, it should be pointed out that the optimum results in grain growth suppression were obtained in cases where the formation of Al_3Zr occurred in as-milled alloys. Some grain growth retardation was obtained, though in cases where the formation of Al_3Zr was a result of annealing.

5.5 Influence of Mg on Grain Refinement

It might be of interest at this stage to comment on the role of Mg in refining the crystal structure of the developed alloys since a study by Furukawa et al. [88] on Al-Sc suggested that Mg has an influence on grain refinement and there exist an optimum concentration of Mg in which finer grains can be obtained. In their study, they examined a series of Al-0.2%Sc alloys prepared by equal channel angular pressing (ECAP) in which the Mg content was varied from 0 to 5%. They observed that the addition of 3 % Mg produced the smallest grain size, ~ 0.2 μm. However, in their study the Mg content was limited to 5% and more elaboration is needed to highlight

the role of Mg in refining the microstructure. Nevertheless, in this research no significant effect of Mg was observed on crystallite size refinement as the crystallite size measurements were comparable in almost all cases regardless of the Mg content into the alloy. The difference between the results obtained in this study compared to the previously reported ones could be related to the formation of nanocrystalline alloys in this research.

5.6 Hardness Values

By considering all the alloys produced in this study, it can be observed that hardness values vary significantly depending on the composition of the starting material. The alloy with the maximum hardness value was $Al_{40}Mg_{25}Zr_{35}$, in having an average hardness value close to 780 HV, and crystallite size of about 10 nm. Moreover, this alloy appears to be thermally stable with grain growth being almost negligible following annealing. This alloy seems to be the best alloy in combining thermal stability and improved mechanical properties. However, it should be mentioned that the oxidation in this alloy was relatively high, which might contribute further to the improvement in hardness values.

For other alloys, like $Al_{55}Mg_{10}Zr_{35}$, hardness values close to 720 HV and a crystallite size of 9 nm were obtained. Little grain growth was observed in this alloy upon annealing, indicative of thermal stability. The common feature among this alloy and the aforementioned one is the increased Al and Zr concentrations. This indicates

that the addition of Al and Zr to the Al-Mg-Zr alloys in high quantities will improve the hardness of the material in addition to the improved stability of the nanostructure. However, no studies were found on the mechanically milled Al-Mg-Zr system where hardness values can be compared to those obtained in this study. The only study [59] found to correlate the higher Zr concentrations to the improvement in hardness for Al-Zr alloys was published for alloys produced by inert-gas condensation.

To compare values obtained from different studies, Srinivasan and Chattopadhyay [95] investigated the hardness of the resulting melt spun Al-Ni-Zr alloys in which a maximum of 500 HV was reached. They attributed this improvement to the formation of nanostructures and the presence of trapped solutes. In general, mechanical alloying seems to improve the hardness of the material significantly compared to melt-spinning. This is because of the nature of the process due to the introduction and accumulation of structural defects into the material. To highlight this, a study by Moon et al. [93] showed that mechanically alloyed Al-Cu-Zr powders had a maximum microhardness value close to 990 HV with a crystallite size of about 22.7 nm in the as-milled and then compacted state using spark plasma sintering (SPS).

5.7 Recommended Alloys

In view of the results obtained for the alloys shown in Figure 5.5, there seems to be a combination of structural stability and improved hardness values. Both of these alloys fall into the nanocomposite structure area, which highlights the benefits of

having a nanostructure on the mechanical properties as well as thermal stability. The improvement of hardness seems to be related to the higher Al and Zr concentrations in these alloys. The formation of an amorphous phase does not seem to significantly affect the hardness values since it was shown earlier that the $Al_{40}Mg_{25}Zr_{35}$ alloy contained low fractions of the amorphous phase.

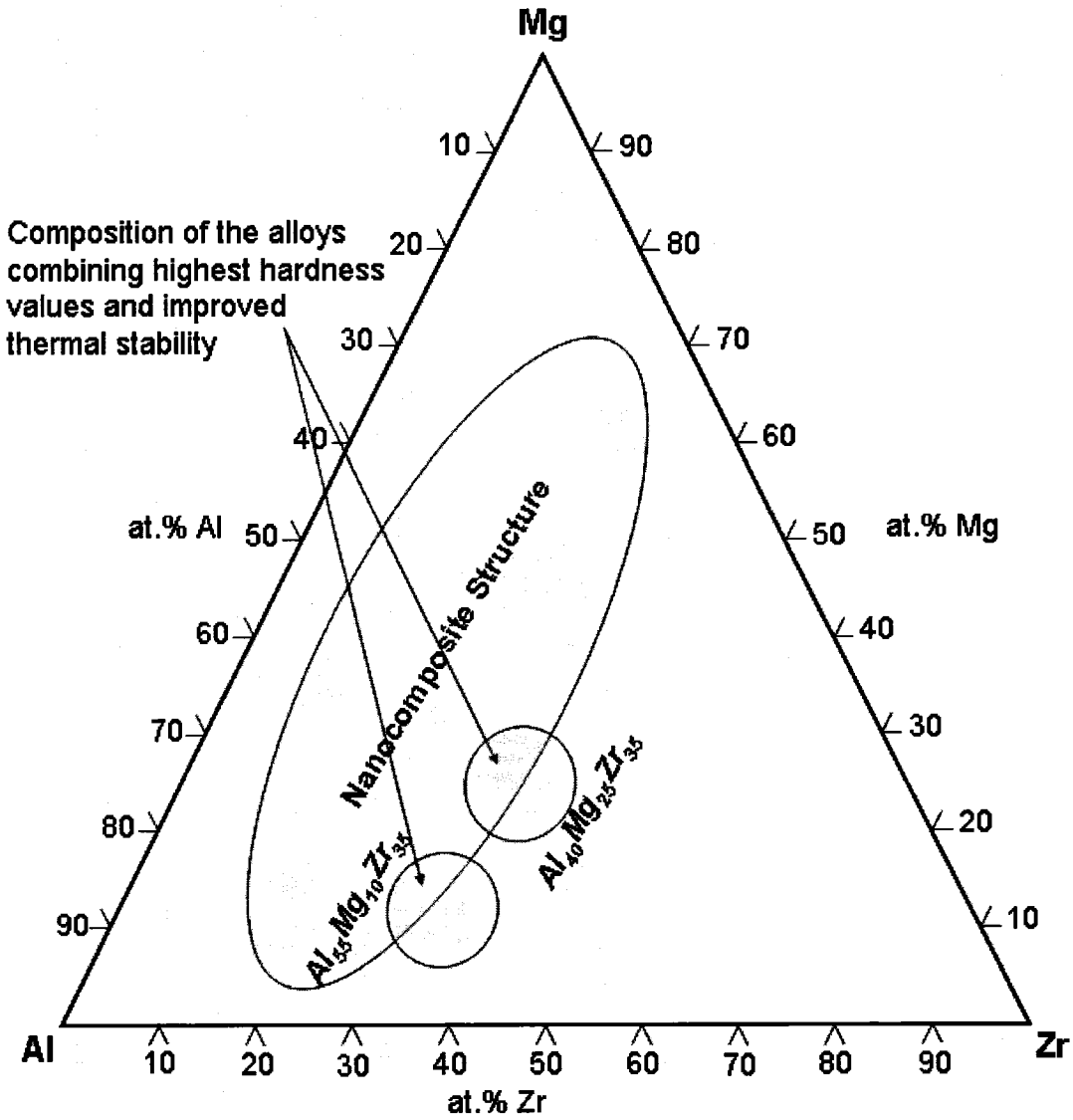

Figure 5.5: Compositions of the best alloys combining improved hardness values and good thermal stability.

Chapter 6

Conclusions, Contributions to Original Knowledge and Future Directions

6.1 CONCLUSIONS

This work was carried out mainly to develop an Al-Mg-based nanocomposite alloys via solid-state synthesis. The following specific conclusions can be drawn from the results obtained:

- The phase constitution of mechanically alloyed binary and ternary mixtures in the Al-Mg-Zr system was strongly dependent on the alloy composition.
- The extension of the solid solubility limit of Mg in Al was beyond the equilibrium value.
- The addition of Zr proved to be beneficial in promoting amorphization in the Al-Mg alloys fabricated via non-equilibrium processing.

- Nanocomposite structure comprising of nanocrystals embedded in an amorphous matrix was developed using a solid-state route. It was the first time that such nanocomposite structures were developed in the Al-Mg-Zr system.
- It was found that mechanical alloying was capable of extending the homogeneity range of many intermetallic phases. Particular interest was given to γ-$Al_{12}Mg_{17}$ in which the homogeneity range was extended beyond values reported in previous studies.
- Employing mechanical alloying proved to be beneficial in successfully producing and retaining Al_3Zr in the cubic $L1_2$ structure which is known to be a high temperature phase. It is known that the retention of Al_3Zr in this structure improves ductility of the alloy substantially.
- In most cases, the developed nanocomposite structure showed extraordinary grain stability evident by the negligible grain growth following annealing experiments at a temperature of 400°C which is related to the presence of Al_3Zr dispersoids. However, an exception was found in the case of Low Al containing alloys where the Al_3Zr was not present in both as-milled and annealed conditions.
- The recommend alloys from this research, that combined the highest hardness values and best thermal stability, were those containing higher Al and Zr concentrations, which highlight the role of both elements in this respect, in addition to their impact on the formation of the nanocomposite structure.

- It was also noted that the homogeneity range of Al_3Zr was extended due to non-equilibrium processing. However, the obtained values were compared to the equilibrium values obtained from the Al-Zr phase diagram.
- The nanocomposite structure was observed in all cases where the Zr concentration exceeded 20 at.% Zr. Nevertheless, the fraction of amorphous phase was not similar in all cases and for some compositions the presence of amorphous phase was detected in residual amounts. As observed, the alloys containing lower Al concentrations (close to 10at.%) were comprised of a low fraction of amorphous phase.
- In general, increasing the Zr proved to be beneficial in refining the structure of the nanocomposite and improving hardness.
- It was found in this research that no significant effect of Mg was observed on crystallite size refinement as the crystallite size measurements were comparable in almost all cases, regardless of the Mg content into the alloy.

6.2 CONTRIBUTIONS TO ORIGINAL KNOWLEDGE

The contributions to original knowledge from this work can be summarized below. This research, for the first time, consisted of a thorough study of a wider range of Zr concentrations (up to 35at.%) to Al-Mg alloys. The maximum Zr concentration considered in literature, ~ 6 at% addition to Al-Mg alloys. Specific contributions are:

- Development of Al-Mg-Zr nanocomposite materials comprising of nanocrystals embedded in an amorphous matrix, and starting from elemental powders.
- A study of the effect of Zr addition on the formation and thermal stability of the nanocomposite structure.
- An investigation of the effect of varying Al/Mg ratio on the final microstructure and properties of the composites.
- Proof on the nanometric scale that the presence of Al_3Zr contributes to the stability of the nanostructure.
- A study of the possible amorphization of Al-Mg-Zr alloys and the role of Zr in promoting nanocomposites formation.
- Determination of the effect of various alloy compositions on nanostructure and mechanical properties of the developed alloys.
- Alloys having a nanocomposite structure that combines higher hardness values and improved grain stability were developed.

6.3 FUTURE DIRECTIONS

In light of this research, some future research directions can be recommended and are listed as follows:

- The extension of Zr concentrations (above 35at.%Zr) could be carried out to study the effect of higher Zr concentrations on the formation of the nanocomposite structure and the anticipated improvement in mechanical properties.
- The effect of alloying conditions, like milling time and temperature, on the formation of nanocomposite structure could be investigated as well. The dependence of amorphous phase formation on milling conditions seems like an interesting future direction of research.
- Differential scanning calorimetry (DSC) studies could be carried out to study the crystallization behaviour of the amorphous structure further and to facilitate more accurate quantification of the amorphous phase.
- The effect of different annealing temperatures on the stability of the nanocomposite structure might be investigated. Additionally, the possible transformation of the cubic structured Al_3Zr to the equilibrium tetragonal DO_{23} upon annealing could be studied as a function of temperature.
- Experiments could be carried out to determine the minimum concentration of Al needed to promote the formation of Al_3Zr in these ternary Al-Mg-Zr alloys.

- Improvement in other mechanical properties could be investigated, like tensile and ductility, which might be improved significantly due to the presence of cubic structured Al_3Zr.
- It was shown earlier in this thesis that the formation of an amorphous phase does not seem to significantly affect the hardness values since it was shown previously that the $Al_{40}Mg_{25}Zr_{35}$ alloy contained low fractions of the amorphous phase. However, the independent role of precipitates and amorphous phase on the thermal stability and hardness need to be studied further.
- Mechanical alloying has a tremendous potential to fabricate a variety of promising systems especially for the development of nanomaterials with improved properties. Glass formers, other than Zr, could be used to explore the possible development of similar nanocomposite structures that combine structural stability and improved mechanical properties.

References

1. C. Suryanarayana, "Mechanical alloying and milling", *Progress in Materials Science* **46**, no. 1-2, 1. (2001)

2. F. H. Froes, C. Suryanarayana, P. R. Taylor, C. M. Ward-Close and P. Goodwin, "Synthesis of advanced lightweight metals by powder metallurgy techniques", *Powder Metallurgy* **39**, no. 1, 63. (1996)

3. C. Suryanarayana, E. Ivanov and V. V. Boldyrev, "The science and technology of mechanical alloying", *Materials Science and Engineering A* **304-306**, no. 1-2, 151. (2001)

4. P. Gilman and J. Benjamin, "Mechanical alloying", *Ann. Rev. Mater. Sci.* **13**, 279-300. (1983)

5. J. Benjamin, "Novel powder processing", *Advances in Powder Metallurgy* **7**, 155. (1992)

6. C. C. Koch and J. D. Whittenberger, "Mechanical milling/alloying of intermetallics", *Intermetallics* **4**, no. 5, 339. (1996)

7. R. M. Davis, B. McDermott and C. C. Koch, "Mechanical alloying of brittle materials ", *Metallurgical Transactions A* **19A**, no. 12, 2867-2874. (1988)

8. C. C. Koch, B. B. Cavin, C. G. McKamey and J. O. Scarbrough, "Preparation of "amorphous" $Ni_{60}Nb_{40}$ by mechanical alloying", *Applied Physics Letters* **43**, no. 11, 1017. (1983)

9. D. L. Zhang, "Processing of advanced materials using high-energy mechanical milling", *Progress in Materials Science* **49**, no. 3-4, 537. (2004)

10. L. Lu and M. O. Lai, "Mechanical alloying", **1st Edition**. (1998)

11. C. Suryanarayana, *Mechanical alloying and milling*, MARCEL DEKKER, New York, (2004)

12. D. B. Witkin and E. J. Lavernia, "Synthesis and mechanical behavior of nanostructured materials via cryomilling", *Progress in Materials Science* **51**, no. 1, 1. (2006)

13. M. A. Shtremel, "Participation of diffusion in the processes of mechanical alloying", *Metal Science and Heat Treatment* **44**, no. 7-8, 324-327. (2002)

14. A. Calka, W. Kaczmarek and J. S. Williams, "Extended solid solubility in ball-milled Al-Mg alloys", *Journal of Materials Science* **28**, 15. (1993)

15. C. Suryanarayana and F. H. Froes, "Nanocrystalline titanium-magnesium alloys through mechanical alloying", *Journal of Materials Research* **5**, no. 9, 1880-1886. (1990)

16. P. B. Desch, R. B. Schwarz and P. Nash, "Formation of metastable Ll_2 phases in Al_3Zr and Al-12.5%X-25Zr (X = Li, Cr, Fe, Ni, Cu)", *Journal of the Less-Common Metals* **168**, 69. (1991)

17. C. C. Koch, "Synthesis of nanostructured materials by mechanical milling: Problems and opportunities", *Nanostructured Materials* **9**, no. 1-8, 13. (1997)

18. C. Suryanarayana and F. H. Froes, "Nanocrystalline structures from amorphous precursors", *Nanostructured Materials* **3**, no. 1-6, 147. (1993)

19. C. Suryanarayana, "Nanocrystalline materials", *International Materials Reviews* **40**, no. 2, 41-64. (1995)

20. G. K. Williamson and W. H. Hall, "X-ray line broadening from filed aluminium and wolfram", *Acta Materialia* **1**, 22. (1953)

21. L. Schultz, "Formation of amorphous metals by mechanical alloying", *Materials Science and Engineering* **97**, 15. (1988)

22. E. Ma and M. Atzmon, "Phase transformations induced by mechanical alloying in binary systems", *Materials Chemistry and Physics* **39**, no. 4, 249. (1995)

23. H. J. Fecht, "Nanostructure formation and properties of metals and composites processed mechanically in the solid state", *Scripta Materialia* **44**, no. 8-9, 1719. (2001)

24. E. Hellestern and L. Schultz, "Progress of the amorphization reaction during mechanical alloying in Fe-Zr", *Journal of Applied Physics* **63**, no. 5, 1408-1413. (1988)

25. L. Lu and Y. F. Zhang, "Influence of process control agent on interdiffusion between Al and Mg during mechanical alloying", *Journal of Alloys and Compounds* **290**, no. 1-2, 279. (1999)

26. G. B. Schaffer and P. G. McCormick, "Reduction of metal oxides by mechanical alloying", *Applied Physics Letters* **55**, no. 1, 45-46. (1989)

27. T. D. Shen, K. Y. Wang, M. X. Quan and J. T. Wang, "Displacement reaction between Fe and CuO induced by mechanical alloying", *Scripta Metallurgica et Materialia* **25**, no. 9, 2143-2146. (1991)

28. G. B. Schaffer and P. G. McCormick, "On the kinetics of mechanical alloying", *Metallurgical Transactions A* **23**, no. 4, 1285-1290. (1992)

29. J. H. Weber and D. J. Chellman, "Mechanically alloyed aluminum alloys for aircraft applications", *Proceedings of ASM International Conference about Structural Applications of Mechanical Alloying*, 147-154. (1990)

30. P. G. McCormick, "Application of mechanical alloying to chemical refining", *Materials Transactions, JIM* **36**, no. 22, 161-169. (1995)

31. D. R. Maurice and T. H. Courtney, "Physics of mechanical alloying. A first report", *Metallurgical Transactions A* **21**, no. 2, 289-303. (1990)

32. J. Joardar, S. K. Pabi and B. S. Murty, "Estimation of entrapped powder temperature during mechanical alloying", *Scripta Materialia* **50**, no. 9, 1199. (2004)

33. D. Singh, C. Suryanarayana, L. Mertus and R. H. Chen, "Extended homogeneity range of intermetallic phases in mechanically alloyed Mg-Al alloys", *Intermetallics* **11**, no. 4, 373. (2003)

34. D. L. Zhang, T. B. Massalski and M. R. Paruchuri, "Formation of metastable and equilibrium phases during mechanical alloying of Al and Mg powders", *Metallurgical and Materials Transactions A* **25A**, 73. (1994)

35. M. Schoenitz and E. L. Dreizin, "Structure and properties of Al-Mg mechanical alloys", *Journal of Materials Research* **18**, no. 8, 1827. (2003)

36. H. L. Luo, C. C. Chao and P. Duwez, "Metastable solid solutions in aluminium-magnesium alloys", *Transactions of The Metallurgical Socity of AIME* **230**, 1488. (1964)

37. S. S. Cho, B. S. Chun, C. W. Won, S. D. Kim, B. S. Lee, H. Baek and C. Suryanarayana, "Structure and properties of rapidly solidified Mg-Al alloys", *Journal of Materials Science* **34**, no. 17, 4311. (1999)

38. K. M. Youssef, R. O. Scattergood, K. L. Murty and C. C. Koch, "Nanocrystalline Al-Mg alloy with ultrahigh strength and good ductility", *Scripta Materialia* **54**, no. 2, 251. (2006)

39. X. Gao, J. F. Nie, M. O. Lai and L. Lu, "Microstructure and mechanical properties of a Mg-5Al alloy synthesized by mechanical alloying", *Materials Science Forum* **437-438**, 101. (2003)

40. C. W. Su, B. W. Chua, L. Lu and M. O. Lai, "Properties of severe plastically deformed Mg alloys", *Materials Science and Engineering: A* **402**, no. 1-2, 163. (2005)

41. F. Zhou, X. Z. Liao, Y. T. Zhu, S. Dallek and E. J. Lavernia, "Microstructural evolution during recovery and recrystallization of a nanocrystalline Al-Mg alloy prepared by cryogenic ball milling", *Acta Materialia* **51**, no. 10, 2777. (2003)

42. L. E. Hazelton, "The effect of composition and milling conditions on the structure of mechanically alloyed Mg-Al based alloys", *Metallurgical and Materials Transactions A* **32A**, 3099. (2001)

43. N. Al-Aqeeli, G. Mendoza-Suarez and R. A. L. Drew, "Characterization and mechanical properties evaluation of Al-Mg-based nanocomposite alloys", *Journal of Alloys and Compounds*. (Accepted)

44. S. M. Umbrajkar, M. Schoenitz, S. R. Jones and E. L. Dreizin, "Effect of temperature on synthesis and properties of aluminum-magnesium mechanical alloys", *Journal of Alloys and Compounds* **402**, no. 1-2, 70. (2005)

45. M. A. Thein, L. Lu and M. O. Lai, "Kinetics of grain growth in nanocrystalline magnesium-based metal-metal composite synthesized by mechanical alloying", *Composites Science and Technology* **66**, no. 3-4, 531. (2006)

46. Y. F. Zhang, L. Lu and S. M. Yap, "Prediction of the amount of PCA for mechanical milling ", *Journal of Materials Processing Technology* **89-90**, 260-265. (1999)

47. D. Hamana, S. Nebti and S. Hamamda, "Effect of the zirconium addition on the microstructure of Al+8wt%Mg alloy", *Scripta Metallurgica et Materialia* **24**, no. 11, 2059-2064. (1990)

48. S. J. Buso, A. A. Filho and W. A. Monteiro, "Characterization by TEM of a supersaturated P/M Al-Mg-Zr alloy after thermal treatments", *Materials Science Forum* **426-432**, 4179. (2003)

49. Z. Y. Ma, R. S. Mishra, M. W. Mahoney and R. Grimes, "High strain rate superplasticity in friction stir processed Al–Mg–Zr alloy", *Materials Science and Engineering* **A351**, no. 1-2, 148-153. (2003)

50. R. Kaibyshev, F. Musin, D. R. Lesuer and T. G. Nieh, "Superplastic behavior of an Al-Mg alloy at elevated temperatures", *Materials Science and Engineering A* **342**, no. 1-2, 169. (2003)

51. H. W. Sheng, K. Lu and E. Ma, "Amorphization of Zr-Al solid solutions under mechanical alloying at different temperatures", *Journal of Applied Physics* **85**, 6400. (1999)

52. H. J. Fecht, Z. F. Han and W. L. Johnson, "Metastable phase formation in the Zr-Al binary system induced by mechanical alloying", *Journal of Applied Physics* **67**, no. 4, 1744. (1990)

53. M. Qian, D. H. StJohn and M. T. Frost, "Characteristic zirconium-rich coring structures in Mg-Zr alloys", *Scripta Materialia* **46**, no. 9, 649. (2002)

54. M. Hamalainen and K. Zeng, "Thermodynamic evaluation of the Mg-Zr system", *Calphad* **22**, no. 3, 375. (1998)

55. Y. L. Shoshin, R. S. Mudry and E. L. Dreizin, "Preparation and characterization of energetic Al-Mg mechanical alloying powders", *Combustion and Flame* **128**, 259. (2002)

56. A. J. Freeman, "Structural stability of intermetallic compounds: A computational metallurgical approach," *Alloy phase stability*, G. M. Stocks and A. Gonis (Editors), Kluwer, Dordrecht, p. 365. (1989)

57. S. Srinivasan, P. B. Desch and R. B. Schwarz, "Metastable phases in the Al_3X (X = Ti, Zr, and Hf) intermetallic system", *Scripta Metallurgica et Materialia* **25**, 2513. (1991)

58. M. Sherif El-Eskandarany, K. Aoki and K. Suzuki, "Calorimetric and morphological studies of mechanically alloyed Al-50at.% transition metal prepared by the rod-milling technique", *Journal of Applied Physics* **72**, no. 7, 2665. (1992)

59. M. N. Rittner, J. R. Weertman, J. A. Eastman, K. B. Yoder and D. S. Stoned, "Mechanical behavior of nanocrystalline aluminum-zirconium", *Materials Science and Engineering A* **237**, no. 2, 185. (1997)

60. J. S. Vetrano, S. Bruemmer, L. M. Pawlowski and I. M. Robertson, "Influence of the particle size on recrystallization and grain growth in Al-Mg-X alloys", *Materials Science and Engineering A* **238**, no. 1, 101-107. (1997)

61. V. Ocenasek and M. Slamova, "Resistance to recrystallization due to Sc and Zr addition to Al-Mg alloys", *Materials Characterization* **47**, 157-162. (2001)

62. Z. Yin, Q. Pan, Y. Zhang and F. Jiang, "Effect of minor Sc and Zr on the microstructure and mechanical properties of Al-Mg based alloys", *Materials Science and Engineering A* **280**, no. 1, 151. (2000)

63. E. J. Lavernia, E. Gomez and N. J. Grant, "The structures and properties of Mg-Al-Zr and Mg-Zn-Zr alloys produced by liquid dynamic compaction", *Materials Science and Engineering* **95**, 225-236. (1987)

64. N. Al-Aqeeli, G. Mendoza-Suarez, A. Labrie and R. A. L. Drew, "Phase evolution of Mg-Al-Zr nanophase alloys prepared by mechanical alloying", *Journal of Alloys and Compounds* **400**, no. 1-2, 96. (2005)

65. Y.-H. Kim, A. Inoue and T. Masumoto, "Ultrahigh tensile strengths of $Al_{88}Y_2Ni_9M_1$ (M = Mn or Fe) amorphous alloys containing finely dispersed fcc-Al particles", *Materials Transactions, JIM* **31**, no. 8, 747. (1990)

66. H. Chen, Y. He, G. J. Shiflet and S. J. Poon, "Mechanical properties of partially crystallized aluminum based metallic glasses", *Scripta Metallurgica et Materialia* **25**, 1421. (1991)

67. Z. C. Zhong, X. Y. Jiang and A. L. Greer, "Micro structure and hardening of Al-based nanophase composites", *Materials Science and Engineering A* **226-228**, 531. (1997)

68. B. R. Murphy and T. H. Courtney, "Synthesis of Cu-NbC nanocomposites by mechanical alloying", *Nanostructured Materials* **4**, no. 4, 365-369. (1994)

69. M. Krasnowski, V. I. Fadeeva and H. Matyja, "Nanocomposites produced by mechanical alloying of the Al50-Fe25-Ti25 powders mixture", *Nanostructured Materials* **12**, no. 1-4, 455-458. (1999)

70. M. Krasnowski and T. Kulik, "FeAl–TiN nanocomposite produced by reactive ball milling and hot-pressing consolidation", *Scripta Materialia* **48**, no. 10, 1489-1494. (2003)

71. F. L. Zhang, C. Y. Wang and M. Zhu, "Nanostructured WC/CO composite powder prepared by high energy ball milling ", *Scripta Materialia* **49**, no. 11, 1123-1128. (2003)

72. J. Li, F. Li and K. Hu, "Preparation of Ni/Al_2O_3 nanocomposite powder by high-energy ball milling and subsequent heat treatment ", *Journal of Materials Processing Technology* **147**, no. 2, 236-240. (2004)

73. M. S. El-Eskandarany, "Mechanical solid state mixing for synthesizing of SiC_p/Al nanocomposites", *Journal of Alloys and Compounds* **279**, no. 2, 263-271. (1998)

74. K. D. Woo and D. L. Zhang, "Fabrication of Al–7wt%Si–0.4wt%Mg/SiC nanocomposite powders and bulk nanocomposites by high energy ball milling and powder metallurgy", *Current Applied Physics* **4**, no. 2-4, 175-178. (2004)

75. S. Hwang, C. Nishimura and P. G. McCormick, "Compressive mechanical properties of Mg-Ti-C nanocomposite synthesised by mechanical milling", *Scripta Materialia* **44**, no. 10, 2457-2462. (2001)

76. H. W. Sheng, J. Xu, X. K. Sun, K. Lu and Z. Q. Hu, "A nanocomposite of $Al_{95}In_5$ synthesized by ball milling", *Nanostructured Materials* **6**, no. 1-4, 417-420. (1995)

77. D. Y. Ying and D. L. Zhang, "Processing of $Cu–Al_2O_3$ metal matrix nanocomposite materials by using high energy ball milling ", *Materials Science and Engineering A* **286**, no. 1, 152-156. (2000)

78. J. M. Wu and Z. Z. Li, "Nanostructured composite obtained by mechanically driven reduction reaction of CuO and al powder mixture", *Journal of Alloys and Compounds* **299**, no. 1-2, 9-16. (2000)

79. M. Yoshimura, T. Ohji, M. Sando and K. Niihara, "Superplasticity of ZrO_2 and ZrO_2/Al_2O_3 composite consisting of nano-sized grains", *Mat. Res. Innovat.* **2**, no. 2, 83-86. (1997)

80. L. Gao, H. Wang, H. Kawaoka, T. Sekino and K. Niihara, "Fabrication of YAG-SiC nanocomposites by spark plasma sintering", *Journal of European Ceramic Society* **22**, no. 5, 785-789. (2002)

81. A. Inoue, C. Fan and A. Takeuchi, "High-strength bulk nanocrystalline alloys in a zr-based system containing compound and glassy phases", *Journal of Non-Crystalline Solids* **250-252**, no. Part 2, 724. (1999)

82. A. Gupta, N. Bhagat, G. Principi, A. Maddalena, N. Malhotra, B. A. Dasannacharya, P. S. Goel, H. Amenitsch and S. Bernstorff, "Nanocrystallisation of amorphous alloys: Comparison between furnace and current annealing", *Intermetallics* **8**, no. 3, 287-291. (2000)

83. L. Reimer, *Transmission electron microscopy: Physics of image formation and microanalysis*, vol. 36, Springer, New York, (1997)

84. C. Suryanarayana and M. G. Norton, *X-ray diffraction: A practical approach*, Plenum Press, New York, (1998)

85. T. Ohashi and R. Ichikawa, "A new metastable phase in rapidly solidified Al-Zr alloys", *Metallurgical Transactions* **3**, 2300. (1972)

86. N. Al-Aqeeli, G. Mendoza-Suarez, C. Suryanarayana and R. A. L. Drew, "Development of new Al-based nanocomposites by mechanical alloying", *Materials Science and Engineering A*. (in review)

87. U. Patil, S. J. Hong and C. Suryanarayana, "An unusual phase transformation during mechanical alloying of an Fe-based bulk metallic glass composition ", *Journal of Alloys and Compounds* **389**, no. 1-2, 121-126. (2005)

88. M. Furukawa, A. Utsunomiya, K. Matsubara, Z. Horita and T. G. Langdon, "Influence of magnesium on grain refinment and ductility in a dilute al-sc alloys", *Acta Materialia* **49**, 3829-3838. (2001)

89. C. Suryanarayana, L. Wenkai and F. H. Froes, "Synthesis of metastable Ll_2 cubic phases in $(Al,M)_3Zr$ (M= Fe, Ni) powders by mechanical alloying", *Scripta Metallurgica et Materialia* **31**, no. 11, 1465-1470. (1994)

90. N. Ryum, "Precipitation and recrystallization in an Al-0.5 wt.%Zr alloy", *Acta Metallurgica* **17**, 269-278. (1969)

91. E. Nes, "Precipitation of the metastable cubic al_3zr-phase in subperitectic Al-Zr alloys", *Acta Metallurgica* **20**, 499-506. (1972)

92. J. Q. Guo, K. Ohtera, K. Kita, T. Shibata, A. Inoue and T. Masumoto, "New metastable phases in rapidly solidified Al-Zr and Al-Ti alloys with high solute content", *Materials Science and Engineering A* **181-182**, 1397-1404. (1994)

93. K. Moon, S. Kim and K. Lee, "A study on the microstructure of do_{23} al_3zr and ll_2 $(al+12.5at.\%cu)_3zr$ intermetallic compounds synthesized by PBM and SPS", *Intermetallics* **10**, 185-194. (2002)

94. J. Q. Guo and K. Ohtera, "An intermediate phase appearing in Ll_2-Al_3Zr to do23-al3zr phase transformation of rapidly solidified Al-Zr alloys", *Materials Letters* **27**, 343-347. (1996)

95. D. Srinivasan and K. Chattopadhyay, "Formation and coarsening of a nanodispersed microstructure in melt spun Al-Ni-Zr alloy", *Materials Science and Engineering A* **255**, 107-116. (1998)

96. J. D. Robson and P. B. Prangnell, "Modelling Al_3Zr dispersoid precipitation in multicomponent aluminium alloys", *Materials Science and Engineering A* **352**, 240-250. (2003)

97. R. D. Doherty, D. A. Hughes, F. J. Humphreys, J. J. Jonas, D. Juul Jensen, M. E. Kassner, W. E. King, T. R. McNelley, H. J. McQueen and A. D. Rollett, "Current issues in recrystallization: A review", *Materials Science and Engineering A* **238**, 219-274. (1997)

98. S. Lee, A. Utsunomiya, H. Akamatsu, K. Neishi, M. Furukawa, Z. Horita and T. G. Langdon, "Influence of scandium and zirconium on grain stability and superplastic ductilities in ultrafine-grained al-mg alloys", *Acta Materialia* **50**, 553-564. (2002)

Appendix - A

List of Publications

This research has yielded the following publications:

Published work:

- N. Al-Aqeeli, G. Mendoza-Suarez, A. Labrie and R.A.L. Drew, "Phase evolution of Mg-Al-Zr nanophase alloys prepared by mechanical alloying", *Journal of Alloys and Compounds*, Vol. 400, pp. 96-99 (2005)
- N. Al-Aqeeli, G. Mendoza-Suarez and R.A.L. Drew, "Characterization and mechanical properties evaluation of Al-Mg-based nanocomposite alloys", presented at the International Symposium on Metastable and Nano Materials (ISMANAM-2006), held in Warsaw, Poland, 27^{th} – 31^{st} August, paper will appear in *Journal of Alloys and Compounds* (Accepted)

Submitted:

- N. Al-Aqeeli, G. Mendoza-Suarez, C. Suryanarayana and R.A.L. Drew, "Development of new Al-based nanocomposites by mechanical alloying", *Materials Science and Engineering A* (Submitted for review)

In preparation:

- N. Al-Aqeeli, G. Mendoza-Suarez and R.A.L. Drew, "The effect of Zr on the formation of nanocomposite structure in Al-based alloys"
- N. Al-Aqeeli, G. Mendoza-Suarez and R.A.L. Drew, "Extension of Homogeneity ranges of intermetallics in Al-Mg-Zr alloys"

Appendix - B

Comparison in crystallite size measurements between XRD and TEM

The following data were obtained by using Scherrer procedure from XRD:

	$Al_{90}Mg_{10}$	$Al_{85}Mg_{10}Zr_5$
As-Milled	14.4	12.9
Annealed	23.1	15

While these crystallite size measurements were obtained by direct TEM measurement:

	$Al_{90}Mg_{10}$	$Al_{85}Mg_{10}Zr_5$
As-Milled	13.5	12
Annealed	22.7	14

It can be seen by comparing the above crystallite sizes obtained by the aforementioned methods it can be seen that the difference is close to 6%.